Ph. D. Dissertation

Photoelectrochemistry of Layered Metal Chalcogenide Electrodes

Qianqian Ba

Supervisors:

Dr. Csaba Janáky

Associate Professor

Dr. Péter S. Tóth

Senior Research Fellow

DOCTORAL SCHOOL OF CHEMISTRY
University of Szeged
Faculty of Science and Informatics
Department of Physical Chemistry and Materials Science
Szeged

2025

Table of Contents

Table of Contents ..... **i**
List of Abbreviations ..... **iii**
List of Figures ..... **v**
List of Tables ..... **ix**
1. Introduction **1**
2. Literature Background **4**
2.1. Challenges of photoelectrochemical hydrogen evolution reaction 4
2.2. Photoelectrode materials - metal chalcogenides 5
2.3. Synthesis methods of metal chalcogenides 10
2.3.1. Top-down method 11
2.3.2. Bottom-up method 15
2.4. Preparation methods of macroelectrodes 15
2.5. SnSe as a promising photocathode material 17
2.6. GaTe as a promising photocathode material 18
2.7. Other promising metal chalcogenides as photoelectrode materials 20
3. Motivation and Aims **24**
4. Experimental **26**
4.1. Materials 26
4.2. Flake preparation 27
4.3. Electrode preparation 30
4.4. Co-catalyst deposition 31
4.5. Physical characterization 32
4.6. Photoelectrochemical measurements 33
5. Results and Discussion **39**
5.1. SnSe flakes activity for photoelectrochemical hydrogen evolution 39
5.1.1. The effect of LPE solvents on PEC HER performance of exfoliated SnSe 39
5.1.2. The effect of flake edge density on PEC HER performance of SnSe 43
5.1.3. The effect of Pt co-catalyst on the PEC HER performance of exfoliated SnSe 48
5.1.4. The PEC HER performance of SnSe synthesized by hydrothermal method 53
5.1.5. The PEC HER behavior of ZnSe/SnSe heterostructure 54
5.2. GaTe flakes activity for photoelectrochemical hydrogen evolution 56

5.2.1. The PEC HER activity of GaTe microelectrodes 56
5.2.2. The PEC HER activity of GaTe macroelectrodes 59
5.2.3. The comparison of PEC activity of GaTe micro- and macro-electrodes 64
5.3. The PEC HER behavior of other semiconductors 65
6. Summary 67
References 70
Acknowledgments 83
Publication list 84

List of Abbreviations

2D – Two-dimensional

ADCD – Aggregated–compacted

AFM – Atomic force microscopy

ALD – Atomic layer deposition

APS – Ambient pressure photoemission spectroscopy

AR – As-received

CB – Conduction band

CE – Chemical exfoliation

CO_2RR – Carbon dioxide reduction reaction

CPD – Contact potential difference

CVD – Chemical vapor deposition

DCB – 1,4-Dichlorobenzene

DMF – Dimethylformamide

DOS – Density of states

EC – Electrochemical

E_F – Fermi level

EQE – External quantum efficiency

FE% – Faradaic efficiency

FTO – Fluorine doped tin oxide coated glass

GC – Glassy carbon

H_2 – Hydrogen

H_2O – Water

HER – Hydrogen evolution reaction

IMPS – Intensity modulated photocurrent spectroscopy

IPA – Isopropanol

IPEC – Incident photon-to-current efficiency

ITO – Indium tin oxide coated glass

KP – Kelvin Probe

LB – Langmuir-Blodgett

LPE – Liquid phase exfoliation

ME – Mechanical exfoliation

N_2 – Nitrogen

NMP – N-Methyl-2-pyrrolidone

O_2 – Oxygen

PEC – Photoelectrochemical

SC – Semiconductor

SCSA – Space-confined self-assembled

SEM – Scanning electron microscopy

SP – Spray coating

SPS – Surface photovoltage spectroscopy

TEM – Transmission electron microscopy

TMCs – Transition metal chalcogenides

TMDCs – Transition metal dichalcogenides

VB – Valence band

WSe_2 – Tungsten diselenide

XPS – X-ray photoelectron spectroscopy

XRD – X-ray powder diffraction

List of Figures

Fig. 1. The scheme of p-type SC applied for photoelectrochemical hydrogen evolution reaction. CB and VB present the conduction band and valence band, respectively. 2

Fig. 2. Statistical analysis of maximum photocurrent density distribution for PEC HER (under 1 sun illumination) with metal chalcogenide electrodes. Adapted from ref.[40]. 6

Fig. 3. (a) Schematic illustration of a microdroplet-based PEC setup [49]. (b) Bar chart of the photocurrent values, recorded with illuminated 1 M HCl/6 M LiCl droplets deposited on various WSe_2-Pt-cycle-1 nanoflake samples with different thickness. The power was 217 mW cm^{-2} [56]. (c) Optical micrograph of a few-layer $MoSe_2$ nanoflake, the edges are marked with white dashed lines [23]. (d) PEC behavior of layered $MoSe_2$ specimens (basal planes), linear sweep photovoltammograms recorded for the illuminated droplets deposited on monolayer, few-layer, and bulk flakes in 6 M LiCl solution; the sweep rate was 5 mV s^{-1} [23].....8

Fig. 4. (a) Representative TEM image of a single-flake-layer WSe_2 layer SCSA thin film deposited on a carbon-coated TEM grid. (b) and (c) show the cross-sectional SEM images of the SCSA and the ADCD films, respectively. The scale bars are 400 nm. (d) Liner sweep photovoltammograms of Pt decorated WSe_2 films prepared by the SCSA and ADCD techniques under chopped illumination (1 sun, 100 mW cm^{-2}). Figures were adapted from ref.[29]. 9

Fig. 5. (a) The concentration of exfoliated GeS powder as a function of solvent surface tension. The concentration of NMP-exfoliated crystal GeS is plotted as a reference [85]. (b) Dispersed concentration as a function of initial MoS_2 crystal concentration. The dashed line shows the initial linear increase. (c) Mean flake length and width of MoS_2 flake as a function of sonication time. The MoS_2 crystals were exfoliated in NMP solvent in panels (b) and (c) [87]. 13

Fig. 6. (a) The scheme of the cascade centrifugation method. Mean values of (b) nanoflake length, ⟨L⟩, and (c) nanoflake thickness of WS_2, ⟨N⟩, as a function of the relative centrifugal forces, presented as central g-force. The WS_2 crystals were exfoliated in NMP. Figures were adapted from ref.[88]. 13

Fig. 7. Schematic illustration of the swelling and exfoliation process of the chemical exfoliation process [90]. 14

Fig. 8. (a) The scheme of Langmuir-Blodgett method with a typical Langmuir trough [96]. (b-d) The space-confined self-assembly approach for WSe_2 thin-film deposition [29]. (b) The schematic diagram of the film deposition method. (c) The photograph of a single-flake-layer WSe_2 thin film deposited on flexible ITO-coated PET plastic, and (d) A representative TEM image of a single-flake-layer WSe_2 film. The scale bar is 2 mm. (e) GeSe film produced by spray-coating the GeSe nanoflakes onto a graphite paper substrate, photograph of a GeSe photoelectrode, which was manually bent to its mechanical flexibility, and its corresponding top-view SEM image. Figures were adapted from: b-d [29], e [98], respectively. 16

Fig. 9. The energy band diagrams related to the NHE at pH=0 of SCs we used. The red and black lines represent the CB and VB positions of SCs, respectively. The values shown in the figure were averaged from several data points from the literature for each SC. 20

Fig. 10. Schematic illustration of liquid phase exfoliation of SnSe layered material, size selection of nanoflakes using centrifugation, and preparation of SnSe nanoflakes-based electrodes with modified Langmuir-Blodgett method [60]. 29

Fig. 11. Schematic illustration of size selection of SnSe crystals, liquid phase exfoliation of SnSe crystals, size selection of nanoflakes using centrifugation, and preparation of SnSe nanoflakes-based electrodes with spray coating method [60]. 29

Fig. 12. The optical image of GaTe nanoflakes prepared by the ME method. Adapted from ref.[200]. 30

Fig. 13. The examples of linear sweep photovoltammograms, recorded for a (a) p-type SC and (b) n-type SC. 34

Fig. 14. Scheme of our photoelectrochemical-microscopy setup. Adapted from ref.[200]. 35

Fig. 15. IMPS result of a n-SC [203]. 38

Fig. 16. Cole–Cole plots of bare SnSe electrode as the function of the applied potential derived from our measured IMPS results [60]. 38

Fig. 17. Morphological and structural characterizations of the IPA-SnSe samples. (a) SEM and (b) AFM images of selected nanoflakes exfoliated from pure IPA. (c) Raman spectra of SnSe samples exfoliated in different solvents. The dashed, and solid lines denoted the SnSe, and $SnSe_2$ vibration bands, respectively [60].....40

Fig. 18. Statistical analysis on (a, d) area, (b, e) perimeter, and (c, f) thickness of different SnSe dispersions, exfoliated using IPA/H_2O (1:3 ratio) (a-c) and IPA/H_2O (1:0 ratio) (d-f). The number insert is the peaked value of the distributions [60]. 41

Fig. 19. (a) Linear sweep photovoltammograms of SnSe electrodes fabricated from SnSe flakes [the flakes were obtained by exfoliating commercial SnSe crystals in different IPA/H_2O mixtures (IPA: H_2O = 1:0 and 1:3)] at 2.5 mV s^{-1} sweep rate, in Ar saturated 0.5 M H_2SO_4 solution under chopped 1 sun illumination. (b) The bar diagrams of photocurrent density of SnSe electrodes plotted at four potentials. SnSe electrodes were fabricated from SnSe flakes exfoliated in different IPA/H_2O mixtures (IPA: H_2O = 1:0, 3:1, 1:1, 1:3). The averaged values and error bars were obtained from three replicate electrodes for each case [60]. 42

Fig. 20. Morphological characterization of the L-, M-, S-SnSe flakes exfoliated in IPA. (a, b, c) TEM, and (d, e, f) AFM images of selected flakes. (L-IPA-SnSe: a, d), (M-IPA-SnSe: b, e), and (S-IPA-SnSe: c, f) [60]. .44

Fig. 21. Statistical analysis on (a, b, c) area, (d, e, f) perimeter, and (g, h, i) thickness of different IPA-SnSe dispersions, exfoliated using L-SnSe crystals (L-IPA-SnSe: a, d, g), M-SnSe crystals (M-IPA-SnSe: b, e, h), and S-SnSe crystals (S-IPA-SnSe: c, f, i) [60]. 45

Fig. 22. (a) XRD pattern of large-size selected SnSe (L-SnSe) crystals, with SnSe and $SnSe_2$ formulations. (b) XRD patterns of the L-, M-, and S-IPA-SnSe flakes at around $2\theta = 15°$ are displayed for clarity. 46

Fig. 23. (a) Linear sweep photovoltammograms for L-IPA-SnSe electrodes as the function of loading. Sweep rate was 2.5 mV s^{-1}. the photovoltammograms were measured in Ar saturated 0.5 M H_2SO_4 solution. (b) Bar diagram of photocurrent density plotted at 5 different potentials for three different loadings. The average values and error bars were obtained from parallel measurements on three different electrodes [60]. 46

Fig. 24. (a) Linear sweep photovoltammograms of SnSe electrodes made from SnSe flakes (obtained by exfoliating (L, M, S)-SnSe crystals in IPA) with 2.5 mV s^{-1} sweep rate, in Ar saturated 0.5 M H_2SO_4 solution. (b) Bar diagrams of photocurrent extracted from linear sweep photovoltammetry curves of the electrodes shown in (a) at five different potentials. The averaged value and error bars were obtained from three replicate electrodes in each case. (c) IPCE of L-, M-, S-IPA-SnSe electrodes. The data were acquired at a fixed potential of −0.54 V vs. RHE [60]. 47

Fig. 25. (a) Transient photocurrent density profile of L-IPA-SnSe electrode. The data were collected at a potential of −0.54 V vs. RHE. (b) Linear sweep photovoltammograms of L-IPA-SnSe electrodes as the function of time (in weeks). The photovoltammetry curves with a sweep rate of 2.5 mV s^{-1}, were measured in Ar saturated 0.5 M H_2SO_4 solution under chopped 1 sun illumination. (c) Bar diagram of photocurrent density plotted versus the potential for five different aged samples. The average values and error bars were obtained from parallel measurements on three different electrodes [60]. 48

Fig. 26. (a-c) Bar diagrams of photocurrents plotted versus potential for bare and Pt deposited SnSe electrodes. Recipes were applied by using (a) different illumination time, (b) different illumination intensity, and (c) different concentration of H_2PtCl_6. (d) High-resolution Pt 4f XPS data of bare and Pt deposited SnSe electrodes [60]. 49

Fig. 27. (a) Linear sweep photovoltammograms of bare and Pt decorated SnSe electrodes. The photovoltammograms with a sweep rate was 2.5 mV s^{-1}, were measured in Ar saturated 0.5 M H_2SO_4 solution under chopped 1 sun illumination. (b) Bar diagram of photocurrent density plotted versus potential, and (c) The determined charge transfer efficiency as a function of applied potential for bare and Pt decorated SnSe photoelectrodes [60]. 50

Fig. 28. IMPS data for (a) bare and (b) Pt decorated SnSe electrodes. Measured 25 mV potential step (only some potential is shown here). (c) Charge transfer and (d) recombination rate constants as the function of the applied potential determined from the IMPS data [60]. 51

Fig. 29. Cole–Cole plots for (a) bare and (b) Pt decorated SnSe electrodes as the function of the applied potential determined from the IMPS data [60]. 52

Fig. 30. Simplified models of the elementary processes in (a) bare SnSe, and (b) Pt decorated SnSe electrodes. Upon illumination, photogenerated carriers move towards the semiconductor-electrolyte interface, (1) surface state-mediated recombination of electron-hole pairs, (2) electron transfer directly from the conduction band to the electrolyte, (3) electron transfer to the electrolyte via Pt [60]. 52

Fig. 31. (a) and (b) SEM images with different resolutions of SnSe film on GC substrate. (c) Linear sweep photovoltammograms of SnSe photocathodes with different loadings, measured in Ar saturated 0.5 M H_2SO_4 solution. Sweep rate is 2.5 mV s^{-1}. (d) Bars of photocurrents as a function of potentials at four different loadings. 53

Fig. 32. Linear sweep photovoltammograms of ZnSe electrodes made from ZnSe flakes (exfoliated from EtOH and IPA solvents, respectively). The photovoltammograms with a sweep rate of 2.5 mV s^{-1}, were measured in Ar saturated 0.1 M Na_2SO_4 solution under chopped 1 sun illumination. 54

Fig. 33. The PEC HER performance of ZnSe/SnSe electrodes. Linear sweep photovoltammograms of (a) bare and ZnSe decorated SnSe electrodes, and (b) ZnSe/SnSe electrodes with and without annealing. The photovoltammograms with a scan rate of 2.5 mV s^{-1} were measured in Ar saturated 0.5 M H_2SO_4 solution. 55

Fig. 34. Morphological and structural characterization of GaTe nanoflakes. (a) Optical image of GaTe nanoflakes on SiO_2/Si substrate. (b) AFM image of GaTe nanoflake indicated by red rectangle in (a), and (c) The height profile from the region highlighted by the dashed blue line in (b). Adapted from ref.[200]. 56

Fig. 35. (a) SPS, (b) APS, and (c) band diagram of mechanically exfoliated GaTe sample [200]. 57

Fig. 36. The PEC activity, thickness-dependent PEC activity, and IPCE data of GaTe microelectrodes. (a) Linear sweep photovoltammograms of GaTe nanoflakes using 6 M LiCl and 1 M HCl/6 M LiCl droplets (sweep rate was 2.5 mV s^{-1}), under chopped illumination. The thickness of GaTe nanoflake herein was 808 ± 50 nm. (b) The photocurrent of GaTe nanoflakes with different thicknesses (100-900 nm) at −1.2 V vs. RHE. (c) IPCE of GaTe nanoflakes with 318 ± 6 nm thickness at −0.59 V vs. RHE. The average values and error bars were obtained from three individual droplets deposited on each nanoflake in three different spots. The electrolyte was 1 M HCl/6 M LiCl in (b-c) [200]. 57

Fig. 37. (a) TEM and (b) AFM images of GaTe nanoflakes exfoliated in pure IPA by the LPE method. Adapted from ref.[200]. 59

Fig. 38. Statistical analysis on (a) perimeter, (b) area, and (c) thickness of the LPE prepared GaTe nanoflakes [200]. 60

Fig. 39. (a) Raman spectrum and (b) XRD pattern of GaTe macroelectrode. Adapted from ref.[200]. 61

Fig. 40. Coverage of GaTe nanoflakes deposited by spray coating on GC substrates. SEM images of (a) 0.1 mg cm^{-2}, (b) 0.3 mg cm^{-2}, and (c) 0.5 mg cm^{-2} loading of GaTe nanoflakes [200].....61

Fig. 41. (a) Linear sweep photovoltammograms of GaTe/GC electrodes as the function of loading. Photovoltammograms were measured in Ar saturated 0.5 M H_2SO_4 solution, scan rate was 2.5 mV s^{-1}. (b) Bar diagram of photocurrents plotted versus the potentials at three different loadings. (c) IPCE of GaTe/GC electrode at −0.59 V vs. RHE in 0.5 M H_2SO_4 solution. Adapted from ref.[200]. 62

Fig. 42. (a) Linear sweep photovoltammograms of GaTe/GC macroelectrodes as the function of illumination intensity. Photovoltammograms were measured in Ar saturated 0.5 M H_2SO_4 solution, the scan rate was 2.5 mV s^{-1}. Five photocathodes from the same batch were studied here. (b) The photocurrent densities of GaTe/GC electrode at −0.79 V vs. RHE under different illumination intensities. (c) The long-term stability of GaTe/GC electrode at −0.54 V vs. RHE under 1 and 10 sun illumination. The mass loading was 0.3 mg cm^{-2} in (a-c) [200]. 63

Fig. 43. SEM images of (a) before and (b) after the long-term chronoamperometry experiments of GaTe nanoflakes [200]. 63

Fig. 44. Linear sweep photovoltammograms of GaTe (a) microelectrodes and (b) macroelectrodes under 200 mW cm^{-2} illumination intensity. The scan rate was 2.5 mV s^{-1} in (a) and (b). 64

Fig. 45. Linear sweep photovoltammograms of GeS nanoflakes exfoliated in various solvents. (a) In EtOH, IPA, EtOH/H_2O and IPA/H_2O. (b) In DCB, NMP, and DMF, here, before the spray coating process, these organic solvents were replaced by EtOH. Linear sweep photovoltammograms were measured in Ar saturated 0.5 M H_2SO_4 solution, the scan rate was 2.5 mV s^{-1} in (a) and (b). 65

List of Tables

Table 1. Summary of the photoelectrochemical activity, measurement conditions, and the preparation methods of transition metal chalcogenides macroelectrodes. This table was adapted from ref [60]..... 10

Table 2. The preparation methods of 2D/layered materials [40]. 11

Table 3. The preparation methods of SC materials (bulk and nanoflakes) that we used for PEC HER application. 28

Table 4. The peaked area, perimeter, thickness, and edge density (perimeter/area) morphological properties for IPA/H_2O and IPA solvents produced SnSe nanoflakes [60]..... 41

Table 5. The overall yield of SnSe fractions exfoliated in IPA [60]. 43

Table 6. The peaked area, perimeter, thickness, and edge density (perimeter/area) morphological properties of SnSe flakes obtained by exfoliating size separated L-, M-, S-SnSe [60]..... 44

Table 7. The summary of band edge positions, Fermi level, and bandgap values for GaTe sample from the Kelvin probe measurements [200]..... 57

Table 8. Summary of the properties of the mechanically exfoliated GaTe flakes used in PEC tests [200]. 58

Table 9. The most probability of perimeter, area, thickness, and the calculated edge density values (perimeter/area) of GaTe nanoflakes collected from dispersions [200]. 60

1. Introduction

The increasing need for global energy is driven by the rapid expansion of the global population and modern industry. The energy sources we rely on in current society are mainly from conventional fossil fuels, which bring the issues of environmental pollution and energy crisis because of the pollutant emissions and the limited reserves. This motivates the development of sustainable energy to generate fuels/feedstocks from earth-abundant resources such as water (H_2O), carbon dioxide (CO_2), and nitrogen (N_2) using renewable energy. Solar energy is a clean and cheap energy source, and it is by far the most abundant renewable energy, which comprises more than 99% of the total amount of all renewable energies available on earth [1–3]. While its intermittent nature and unbalanced availability demand the storage of captured solar energy. There are several ways to use this plentiful energy. The photovoltaic (PV)-electrolysis system can directly convert solar energy into electricity which must be consumed immediately or stored in batteries/capacitors with limited storage capacity [3,4].

Solar energy can also be directly converted into chemical energy through photosynthesis, which is the oldest method and has been developed by nature over the past billion years. Inspired by nature, researchers developed this method, named artificial photosynthesis, which aims to utilize sunlight to produce renewable energy, typically in the form of electricity, but using totally different approaches and materials. Artificial photosynthesis consists of two major methods including photoelectrochemistry and photocatalysis.

Compared with photocatalysis, the photoelectrochemical (PEC) system integrates the photocatalysis and electrocatalysis systems, which makes full use of external bias and solar energy in a unified reaction system. There are several reasons why this method is appealing. One of the biggest advantages is that hydrogen (H_2) and oxygen (O_2) are generated from separate electrodes, which allows the easy separation of these gas products without postseparation process, avoiding the safety issue due to the inflammability of H_2. Another advantage is that this process can be performed at room temperature, which is energy saving. The third advantage is that the PEC water splitting devices can be totally fabricated from inorganic materials [9,10]. Moreover, the PEC technique has two potential advantages compared to PV-electrolysis. The first advantage is since the fact that the commercial electrocatalysts require cell voltages of around 1.9 V to achieve their optimal operating current density of around 1 A cm^{-2}. As the

thermodynamically needed potential for water splitting is 1.23 V, this results in an upper limit of 65% (1.23/1.9) for overall energy conversion efficiency [5]. While the current density at a photoelectrode immersed in water is much smaller (maximum 10–20 mA cm^{-2}) and the necessary overpotential is significantly lower. The second one is that a PEC system can be constructed as a single device, which demands fewer packaging components (like glass, quartz, and frame) and may lead to lower costs. Therefore, photoelectrochemistry constitutes the topic of this dissertation.

The photoelectrode material, namely semiconductor (SC), plays a critical role in the PEC system [6]. When the illumination power is equal to or higher than the bandgap of SCs, the electrons can be excited from the valence band (VB) position to the conduction band (CB), leaving the holes in the VB. As the photocathode (p-type SC) shown in **Fig. 1**, under applied external bias, the electrons are driven to the working electrode surface, to drive the reduction process (for example, water reduction reaction). The holes migrate to the counter electrode (anode) to participate in the oxidation reaction. For the photoanode (n-type SC), the photogenerated charge carriers transfer occurs in the opposite direction: the holes go to the working electrode surface to drive the water oxidation reaction while the electrons transfer to the counter electrode to forward the reduction process [7]. Thus, the energy from the incoming light can be stored in the products in the form of chemical bonds.

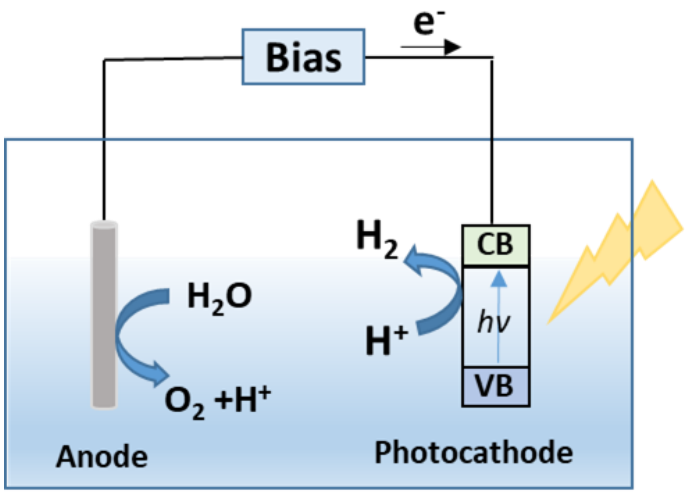

Fig. 1. The scheme of p-type SC applied for photoelectrochemical hydrogen evolution reaction. CB and VB present the conduction band and valence band, respectively.

PEC hydrogen evolution and CO_2 reduction reactions (HER and CO_2RR) are the most widely investigated processes to generate valuable fuels, such as H_2, carbon monoxide, methane, and methanol, to replace the traditional fossil fuels [8]. PEC HER has been studied for decades since it was first reported by Fujishima and Honda in 1972 [9]. It is a promising technique which can efficiently utilize 120,000 terawatts of solar radiation striking to the earth's surface. Efforts in this field are directed to develop new materials which can efficiently facilitate H^+ reduction reaction, ultimately paving the way for industrial applications. Our study focuses on the synthesis of such materials, and the investigation of their PEC HER behavior along with exploring their applicability as photoelectrodes for solar fuel and chemical generation processes.

2. Literature Background

2.1. Challenges of photoelectrochemical hydrogen evolution reaction

The water splitting reaction to produce H_2 (or O_2, **Equation 1**) is a thermodynamically uphill reaction, and the free energy change under standard-state conditions of this process is ΔG^o = 237 kJ mol^{-1} or $\Delta E^o = -1.23$ V.

$$2H_2O \rightarrow O_2 + 2H_2 \qquad (1)$$

The energy needed to drive PEC water splitting is supplied by solar simulator or ideally sunlight [10]. Therefore, the SCs possessing a narrow bandgap (~1.5 eV) with a high absorption coefficient (10^4–10^5 cm^{-1}) over a wide wavelength range to harvest most of the solar irradiation are desired in this PEC system. Many SCs have been studied as photocathode materials in this field over the past decades, for example, Si [11] and copper oxides [12], which achieved decent PEC performance. Despite significant advancements in PEC HER, the efficiency and long-term stability of photoelectrodes remain critical limitations that hinder its large-scale commercialization. These challenges arise from issues such as insufficient light absorption, fast recombination of charge carriers, and degradation of materials under operating conditions. In this regard, the employed photoelectrode materials must fulfill several key criteria simultaneously to achieve efficient and sustainable hydrogen production [13]:

i). The *bandgap* must be small enough to harvest a large portion of the solar spectrum, but big enough to suppress the rapid recombination of photogenerated charge carriers.

ii). The *band edge positions* at the electrode surface should straddle the H_2 and O_2 redox potentials, which means that the CB and VB positions should be more negative and positive than the water reduction and oxidation potential, respectively.

iii). The photoelectrode materials must exhibit good *long-term stability* over the desired pH and potential window.

iv). *Efficient charge transport*, which is necessary to facilitate the extraction of the photogenerated charge carriers towards the electrode/electrolyte junction and back contact, minimizing the significant recombination. This means, for a p-type SC, that the

higher the mobility of the photogenerated electrons and holes within the material, the higher the produced photocurrent.

v). *Fast charge transfer* from the electrode surface to the electrolyte, which can minimize the energy losses due to the kinetic overpotential.

vi). *Low toxicity*.

vii). Low cost and facile preparation methods.

The ongoing research and development aim to discover new materials possessing the desired bulk and interfacial characteristics which can meet these criteria. Therefore, there is a clear need to develop highly efficient and stable SC-based photoelectrodes to reach this goal.

2.2. Photoelectrode materials - metal chalcogenides

So far, a variety of SCs have been employed as photoelectrode materials in the past decades, such as metal oxides [12,14], metal chalcogenides [15–17], group III-V and group IV materials [18,19]. Among those SCs, metal chalcogenides, for example, MoS_2, WSe_2, and CuS_2, have gained considerable attention due to their excellent optical and electrical properties [16,17,20–23]. Studies on water splitting using metal chalcogenides bulk crystals date back to the early 1980s, which have achieved high photocurrent (around 10 mA cm^{-2}) [24–27]. **Fig**. **2** shows the histogram of the maximum photocurrent density values (recorded under 1 sun illumination) collected from the literature for PEC HER application of metal chalcogenides [17,28–39], which was adapted from our review paper [40]. Only studies reporting photocurrent densities over 1 mA cm^{-2} were included in the detailed analysis here. The highest photocurrent density of around 60 mA cm^{-2} was achieved on MoS_2 under ca. 6 sun illumination [41]. **Fig**. **2** indicated that over 50% of photocurrent density values is below 10 mA cm^{-2}, thus it is desirable to investigate the factors that limit such materials for achieving high PEC HER activity (over 10 mA cm^{-2}).

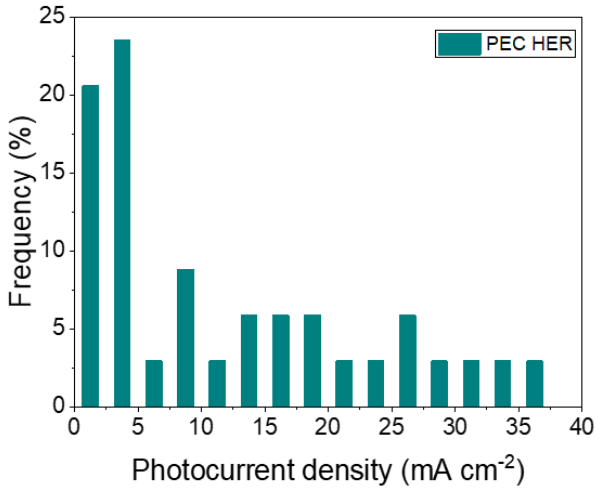

Fig. 2. Statistical analysis of maximum photocurrent density distribution for PEC HER (under 1 sun illumination) with metal chalcogenide electrodes. Adapted from ref.[40].

Microelectrodes-based PEC studies

Studies on the two-dimensional (2D) materials have gained intensive interest since the successful isolation of graphene [42]. When using 2D materials for (photo)electrocatalysis, it is crucial to consider the impact of defects like steps, edges, and atomic vacancies in their crystal structure. These defects, particularly at the edges, significantly affect their electrochemical (EC) behavior. It is widely accepted that the EC activity is higher at the defective edges compared to the basal plane of 2D flakes, while the exact reasons for these variations are still under investigation [23,43–45]. For bulk transition metal dichalcogenides (TMDCs), the activities of basal plane and edge were extensively investigated a few decades ago [24–27,46]. Tungsten diselenides (WSe_2) for example, higher EC and lower PEC activity were observed for edge planes, compared to its basal plane. This phenomenon is attributed to the defects and edges creating surface states within the bandgap, acting as the recombination centers for photogenerated charge carriers.

The influence of structural domains (e.g., in plane defects, edges, and thickness of sheets) on PEC activity of 2D and layered materials has been investigated by using microscale EC/PEC techniques, such as scanning electrochemical cell microscopy, scanning electrochemical microscopy, and microdroplet-based methods [47–55]. **Fig. 3a** shows the schematic illustration of a microdroplet-based PEC setup. A single-nanoflake scanning photocurrent microscopy approach has been employed on WSe_2 nanoflakes for example, revealing that charge carrier

recombination occurs more near perimeter edges than basal planes [23]. Lewis and co-workers employed a scanning photocurrent microscopy to investigate the PEC behavior of bare and Pt-deposited WSe_2 photoelectrodes, and the results presented significant variation in the photoconversion efficiency of terraces of the layered structures. The observed variation is ascribed to the uneven distribution of surface and bulk defect states among terraces, particularly chalcogenide vacancies [49].

Recently in our group, we have observed the spatial variation of the PEC activities of $MoSe_2$ and WSe_2 photoanodes in the oxidation reaction of a model redox couple (**Fig. 3c–d**) [23]. We have also found that Pt nanoparticles deposited on p-type WSe_2 flakes by atomic layer deposition (ALD) cause significant improvement in the PEC HER activity (**Fig. 3b**). This enhancement was affected by the bulk defects and their migration to the surface. The heat-induced W(VI) defects during ALD process result in a reduction in the density of states (DOS) near the valence band of WSe_2. The Pt nanoparticles produced by ALD suppressed the DOS decrease caused by W(VI), leading to a better PEC performance [56].

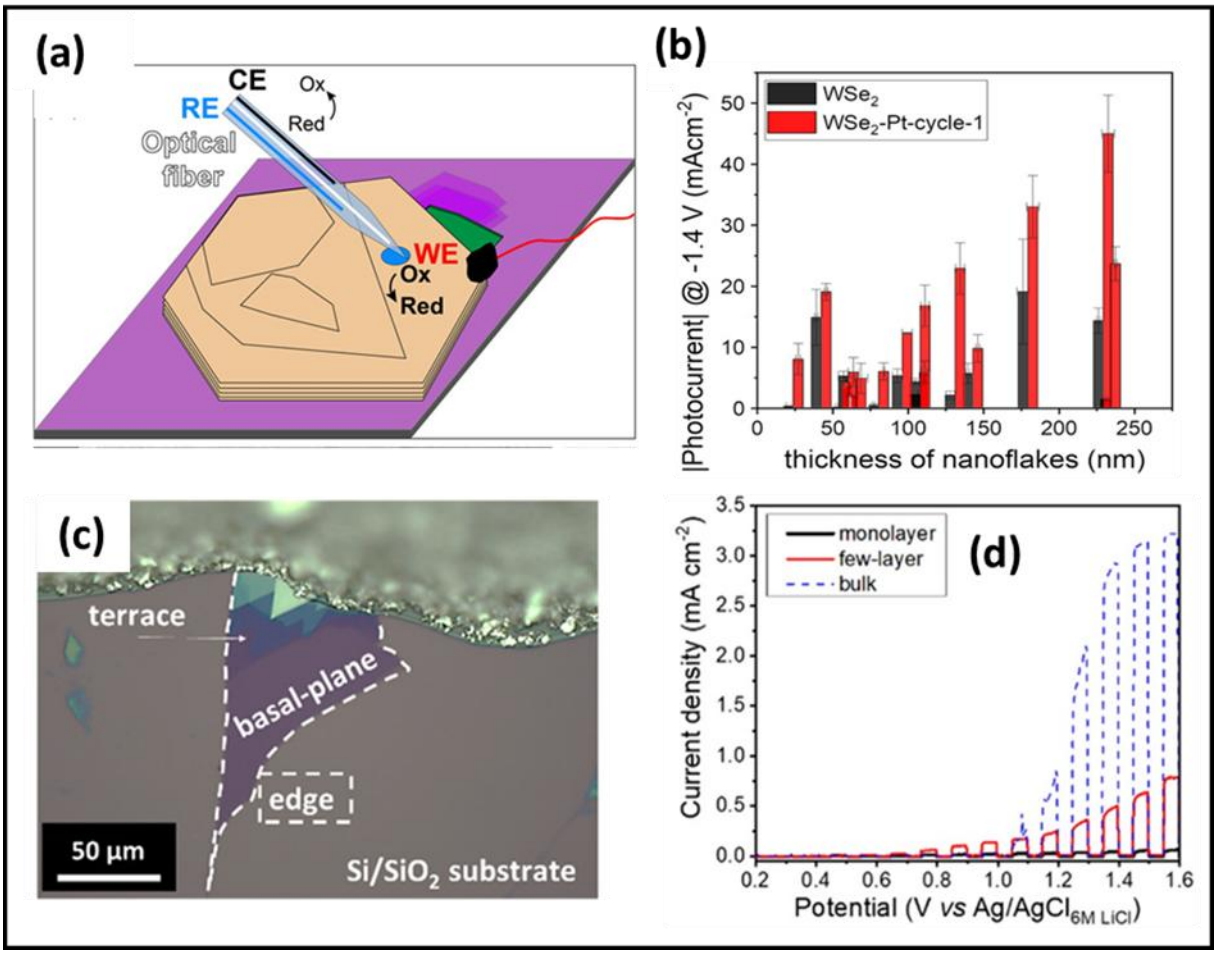

Fig. 3. (a) Schematic illustration of a microdroplet-based PEC setup [49]. (b) Bar chart of the photocurrent values, recorded with illuminated 1 M HCl/6 M LiCl droplets deposited on various WSe_2-Pt-cycle-1 nanoflake samples with different thickness. The power was 217 mW cm^{-2} [56]. (c) Optical micrograph of a few-layer $MoSe_2$ nanoflake, the edges are marked with white dashed lines [23]. (d) PEC behavior of layered $MoSe_2$ specimens (basal planes), linear sweep photovoltammograms recorded for the illuminated droplets deposited on monolayer, few-layer, and bulk flakes in 6 M LiCl solution; the sweep rate was 5 mV s^{-1} [23].

Macroelectrode-based photoelectrochemical studies

Typically, enlarging the photoelectrode area from the micrometer scale to mm^2 or cm^2 results in a significant reduction in photocurrent (to the µA cm^{-2} range) due to the presence of numerous defects [22,29,57]. Meanwhile, given the ultimate application of solar energy conversion devices, it is essential to prepare microelectrodes. In this regard, many works have been reported to fabricate microelectrodes [29,37,58,59]. For example, Yu and co-workers prepared WSe_2 nanoflakes with liquid phase exfoliation (LPE) method, then they fabricated the WSe_2 film using space-confined self-assembled (SCSA) and aggregated–compacted (ADCD) film formation approaches, respectively [29]. The morphology of SCSA film is characterized by TEM, as

shown in **Fig. 4a**, and no significant aggregation or restacking of the nanoflakes is observed. **Fig. 4b** and **c** displayed the cross-section images of these films, confirming that for the SCSA film, the film consists of a single sheet with the sheet orientation parallel to the substrate, whereas in the ADCD film, the film is thicker and the sheet orientation is more random. The PEC performance of electrodes after Pt co-catalyst decoration is presented in **Fig. 4d.** SCSA film shows much higher PEC HER activity than that of ADCD film. Furthermore, **Table 1** shows the PEC HER performance of reported macroelectrodes composed of flakes, including the results of my doctoral work.

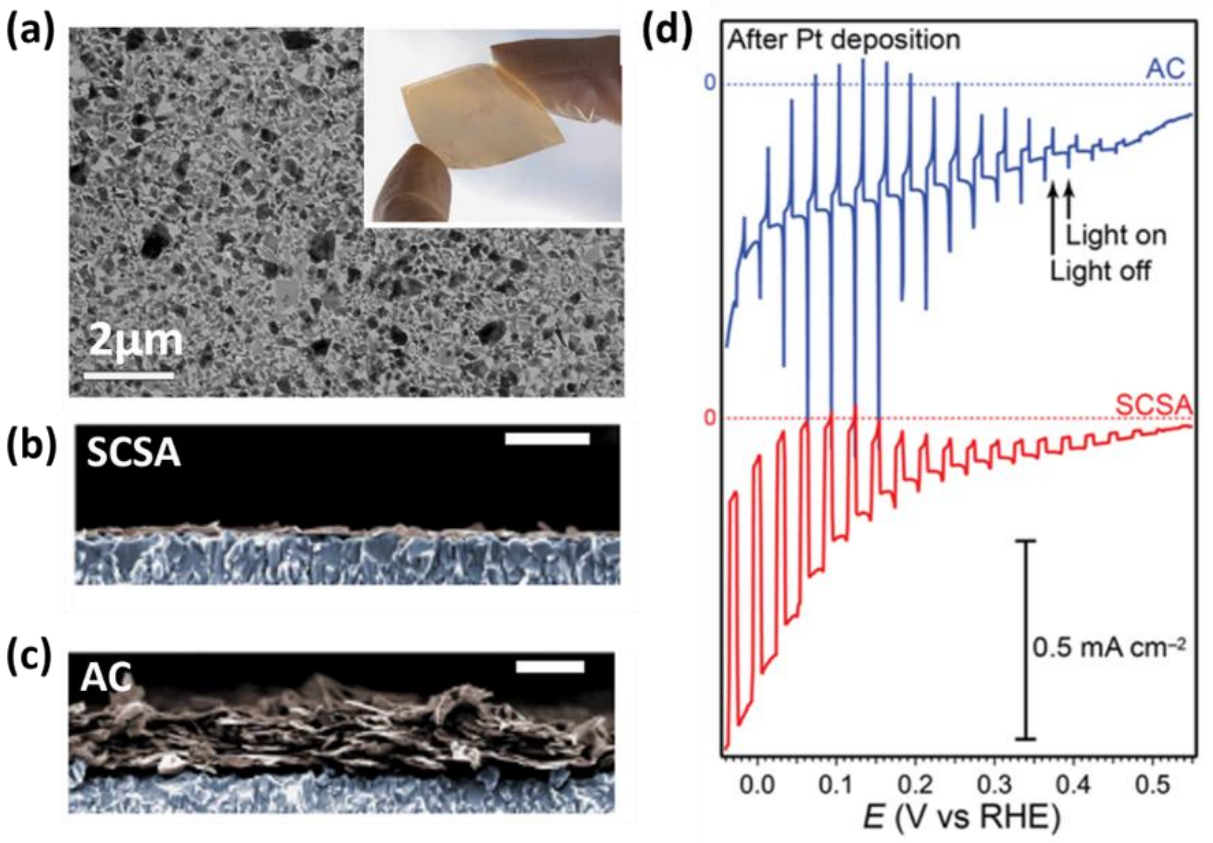

Fig. 4. (a) Representative TEM image of a single-flake-layer WSe_2 layer SCSA thin film deposited on a carbon-coated TEM grid. (b) and (c) show the cross-sectional SEM images of the SCSA and the ADCD films, respectively. The scale bars are 400 nm. (d) Liner sweep photovoltammograms of Pt decorated WSe_2 films prepared by the SCSA and ADCD techniques under chopped illumination (1 sun, 100 mW cm^{-2}). Figures were adapted from ref.[29].

Table 1. Summary of the photoelectrochemical activity, measurement conditions, and the preparation methods of transition metal chalcogenides macroelectrodes. This table was adapted from ref [60].

Material	j_{max} (mA cm^{-2})	Potential (V vs. RHE)	Conditions	Flake preparation method	Film preparation method	Ref.
WSe_2	0.03	0	1 M H_2SO_4; 100 mW cm^{-2} (Cree MCE4 LED)	LPE	SCSA	[22]
WSe_2	0.04	0	1 M H_2SO_4; 100 mW cm^{-2} (Xenon lamp)	LPE	SCSA	[29]
WSe_2	~ 0.01	0.05	0.5 M H_2SO_4; 100 mW cm^{-2} (Xenon lamp)	aSLcS	aSLcS	[57]
MoS_2	~ 0.5	–0.5	0.5 M H_2SO_4; 150 mW cm^{-2} (Xenon lamp)	hydrothermal method	hydrothermal method	[61]
WS_2	~ 1	–0.5	0.5 M H_2SO_4; 150 mW cm^{-2} (Xenon lamp)	hydrothermal method	hydrothermal method	[61]
SnSe	1.4	–0.2	0.05 M H_2SO_4; 100 mW cm^{-2} (Optical fiber source, FX300)	thermal vacuum evaporation	thermal vacuum evaporation	[62]
SnSe	0.06	–1.0	1.5 M Na_2SO_3; 90 mW cm^{-2} (polychromatic lamp)	electro-deposition	electro-deposition	[63]
SnSe	0.02	–0.6	0.2 M $Eu(NO_3)_3$; 100 mWcm^{-2} (Xenon lamp)	electro-deposition	electro-deposition	[64]
SnSe	2.44	–0.74	0.5 M H_2SO_4; 100 mW cm^{-2} (Xenon lamp)	LPE	spray coating	Our work
GaTe	4	–0.74	0.5 M H_2SO_4; 1000 mW cm^{-2} (Xenon lamp)	LPE	spray coating	Our work

2.3. Synthesis methods of metal chalcogenides

Various approaches have been employed to synthesize transition metal chalcogenides (TMCs) with controlled size and crystallinity, which can be classified as either bottom-up or top-down methods [65]. **Table 2** summarizes the mostly used synthesis techniques of 2D/layered materials and its characteristics (yield, cost, and aimed materials), and the application of the as-prepared materials with some representative references [66–69].

Table 2. The preparation methods of 2D/layered materials [40].

Strategy	Methods	Flakes Yield	Cost	Resulted Materials	Application	References
Top–down	Liquid Phase Exfoliation	High	Moderate-high	TMCs/Oxides	Research/ commercial	[70,71]
	Chemical Exfoliation	High	Moderate-high	Oxides/TMCs/MXenes	Research/ commercial	[66,72]
	Mechanical Exfoliation	Low	Low	TMCs	Research	[23,47]
Bottom–up	Chemical Vapor Deposition	High	High	TMCs/Oxides	Research/ commercial	[73,74]
	Spray Pyrolysis	High	High	MXenes/Oxides	Research/ commercial	[69,75]
	Hydrothermal Synthesis	High	Moderate-high	TMCs/Oxides	Research/ commercial	[76,77]
	Atomic Layer Deposition	High	High	TMCs	Research/ commercial	[78,79]

2.3.1. Top-down method

In the top-down method, the 2D/layered materials are prepared from their parent bulk counterparts. The mostly used top-down method includes mechanical, liquid-phase, and chemical exfoliation processes [80], and these approaches are discussed below:

Liquid phase exfoliation (LPE)

LPE is a method in which the layered crystals are dispersed in a solvent and exfoliated to nanoflakes with external forces, like controlled ball milling, solvothermal, or ultrasonication processes. It was first reported in 1989 for the production of MoS_2 and WSe_2 nanosheets [81], and was later adapted for graphene in 2008 [82], demonstrating a cost-effective and scalable approach for the mass production of 2D materials. Furthermore, Coleman et al. applied this method on other layered compounds, such as $MoTe_2$, $TaSe_2$, and BN, to obtain their flakes efficiently [83]. The size and yield of resultant flakes can be affected by several factors:

i). The *solvents*. According to the reported studies, the layered materials are most effectively dispersed in solvents with matching surface energy [84], namely the surface tensions of the solvent and the material are close. Layered crystals may have different exfoliation efficiency in different solvents because of different interactions between solvents and crystals. **Fig. 5a** shows the plot of concentration of GeS flakes as a function of LPE solvent surface tension [85]. Toxic solvents with high boiling points, such as N-Methyl-2-pyrrolidone (NMP) and 1,4-dichlorobenzene (DCB), have been commonly used to prepare flakes, while such solvents are not easy to remove from the surface, leading to a big loss of the material and the generation of toxic waste. Recently, more green solvents with low boiling points and toxicity, for example, ethanol, isopropanol (IPA), and the mixture of water/alcohol, have been used in the LPE process [60,85,86].

ii). Higher *initial concentration of crystals* in a certain degree leads to higher concentration of as-resultant flakes. Coleman and co-workers studied the effect of it on the concentration of MoS_2 nanoflakes, which were exfoliated from NMP, and a positive linear relation was observed when the initial concentration of MoS_2 crystals was below 100 mg cm^{-2} (**Fig. 5b**) [87].

iii). Different *sonication times* can result in as-resultant flakes with different sizes (length, width, and thickness). One example is shown in **Fig. 5c**, the flake size of MoS_2 increases with shorter sonication time, while it decreases at longer sonication time because of the sonication-induced scission [87].

iv). The flakes based on different flake size parameters (e.g., length, thickness) can be separated by using centrifugation with *different speeds/relative centrifugal forces (g-force*). One of the well-known methods is the cascade centrifugation approach, and its scheme is shown in **Fig. 6a** [88]. The flakes with larger length and thicker thickness are screened out first. Moreover, a negative linear correlation between the mean flake length/thickness of WS_2 and g-force was found (**Fig. 6b-c**).

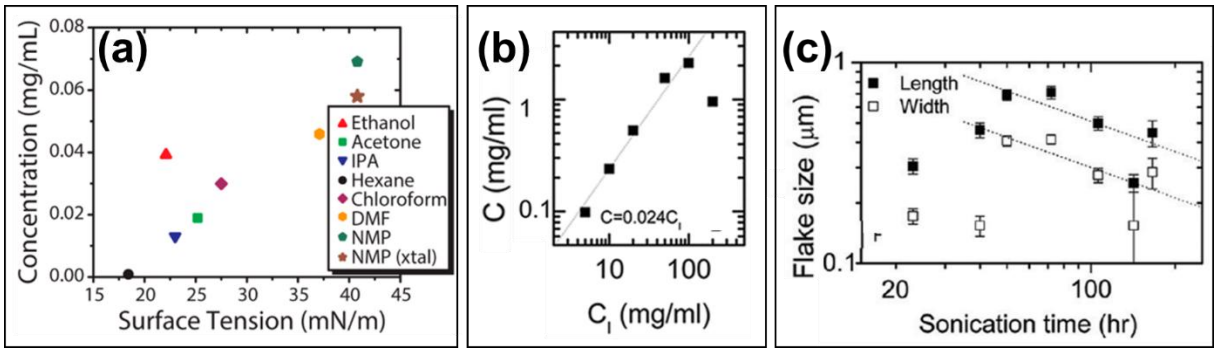

Fig. 5. (a) The concentration of exfoliated GeS powder as a function of solvent surface tension. The concentration of NMP-exfoliated crystal GeS is plotted as a reference [85]. (b) Dispersed concentration as a function of initial MoS_2 crystal concentration. The dashed line shows the initial linear increase. (c) Mean flake length and width of MoS_2 flake as a function of sonication time. The MoS_2 crystals were exfoliated in NMP solvent in panels (b) and (c) [87].

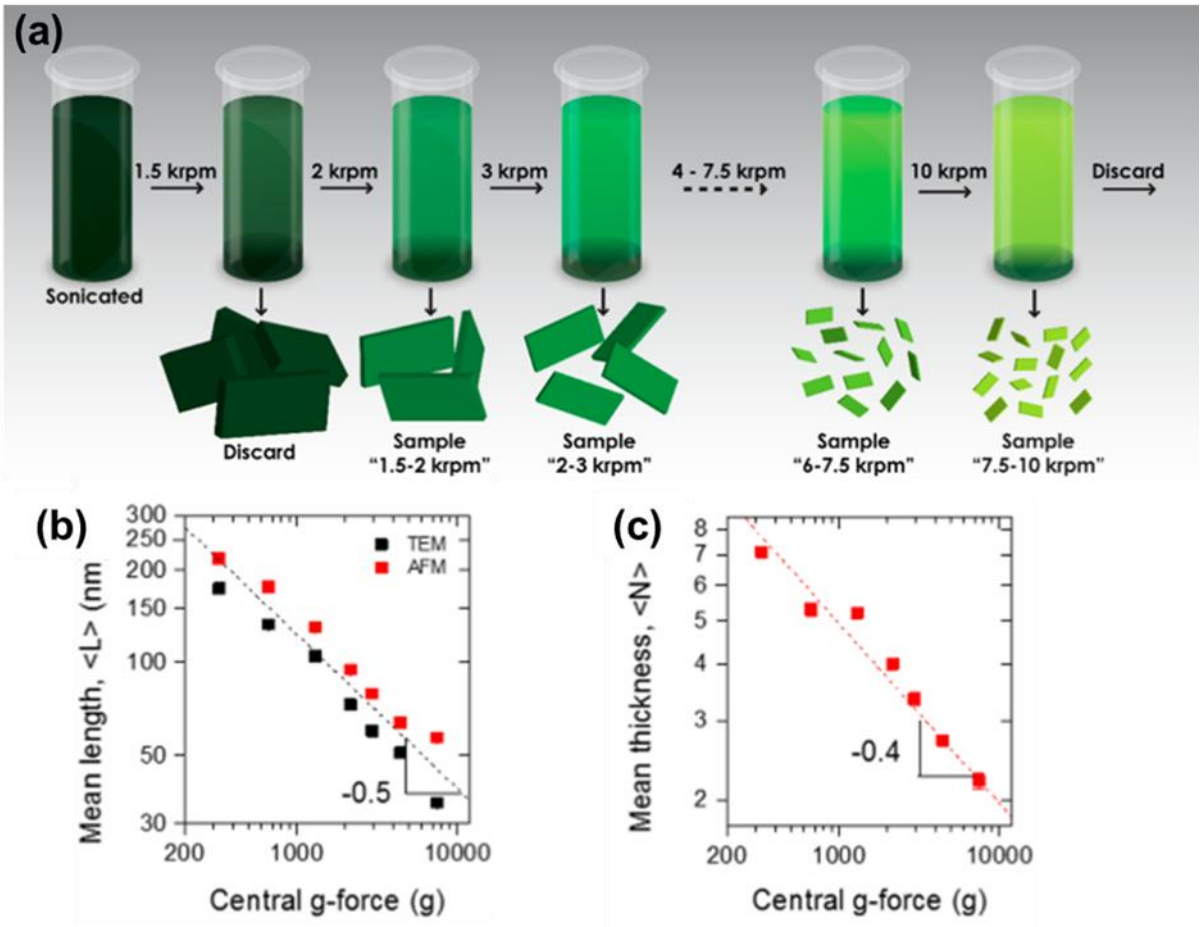

Fig. 6. (a) The scheme of the cascade centrifugation method. Mean values of (b) nanoflake length, ⟨L⟩, and (c) nanoflake thickness of WS_2, ⟨N⟩, as a function of the relative centrifugal forces, presented as central g-force. The WS_2 crystals were exfoliated in NMP. Figures were adapted from ref.[88].

Mechanical exfoliation (ME)

ME is one of the most widely used methods to prepare high-quality nanoflakes from their bulk crystals [23,42,47]. In general, layered materials can be cleaved because of the weak van der Waals force within intralayer. This method requires very simple setups (normally an adhesive tape is needed), and can be employed to prepare thin layers and 2D materials by using repeated cleavage process [58]. Since the first isolation of graphene in 2004 [42], many other inorganic layered materials have been exfoliated by ME method to give thin nanoflakes with some interesting properties. For example, a thickness-dependent optical property of GaTe was observed by using ME-prepared GaTe flakes [89]. Therefore, this approach is important in the exploration of the undiscovered physical phenomena of layered materials. While the low yield and relatively small size of the flakes obtained with this method limit its practical applicability for some device applications.

Chemical exfoliation (CE)

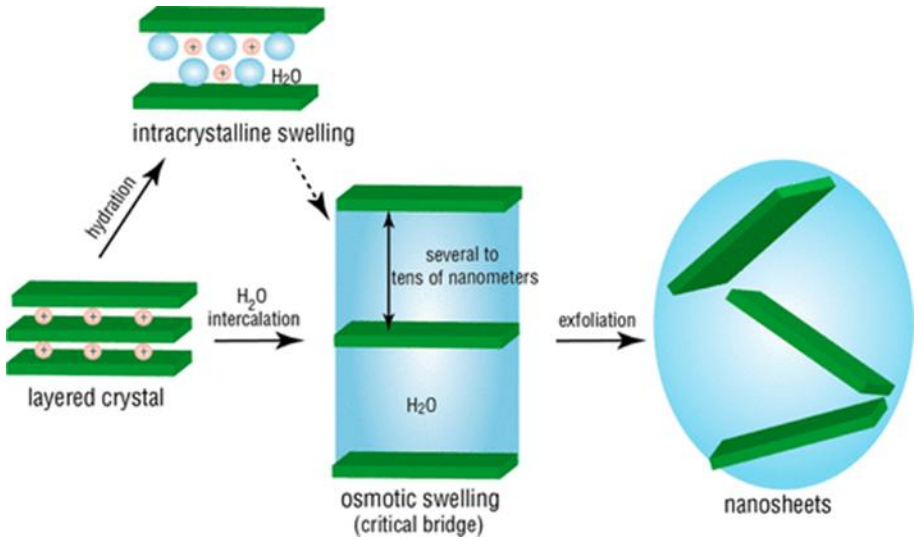

Fig. 7. Schematic illustration of the swelling and exfoliation process of the chemical exfoliation process [90].

The chemical exfoliation of layered materials has been widely investigated over the past few decades. **Fig. 7** shows the schematic illustration of this method. It demonstrates that ions/molecules play dual roles. Firstly, the insertions of ions/molecules expand the host interlayer spacing, which weakens the van der Waals interactions of the interlayers. Secondly, under the applied external force, for example, ultrasonication, the layers can be separated into multi- and mono-layer [90]. Various ions have been applied in the CE process, such as Li^+,

which is commonly employed to prepare thin-layer of TMDCs [91]. While several drawbacks of this CE process should be mentioned here, such as i) the long processing time, and sometimes the high reaction temperature. ii) the relatively small size of resultant nanoflakes. iii) more defects might be produced [68].

2.3.2. Bottom-up method

In the bottom-up method, the nanomaterials are constructed by assembling either atoms or clusters into nanoscale structures. It includes, for example, chemical vapor deposition (CVD) [74,92], hydrothermal [77], and atomic layer deposition [78,93]. Among these approaches, the hydrothermal method is the one that generally requires lower temperature and vacuum, which can be used to synthesize nanomaterials at a low cost. It utilizes an aqueous solution as a reaction system in a special closed reaction vessel, heating such reaction system to create a high-temperature and high-pressure reaction environment [94]. Many metal chalcogenides with nanoplate/nanosheet morphology have been successfully prepared by this method. Moreover, the materials can be either directly grown on the substrates by inserting the clean substrates into the reaction solvents before the reaction, or first synthesized and then processed to film on the substrates [35,77,95].

2.4. Preparation methods of macroelectrodes

From a practical standpoint, it's highly desirable to prepare macroelectrodes with large-area and continuous film to further develop solar energy conversion devices. In this regard, a variety of preparation methods have been established and developed, such as the most traditionally used approaches: Langmuir-Blodgett and spray coating methods.

Langmuir-Blodgett (LB) method

LB technique provides a flexible way to prepare layers/films on solid substrates. Its scheme was shown in **Fig. 8a,** which consists of two main steps: i) dropping the material suspension into the water, and the materials self-assemble to thin film (Langmuir-film) at air-water interface. ii) inserting solid substrate into the water, then the film is transferred onto it (LB film formed) [96]. Many films of layered SCs, such as $MoSe_2$ and WSe_2, have been fabricated by this method [23,60,97]. Moreover, this approach has been developed, for example, adding a stirring

procedure throughout the film forming [96], or preparing the film without using the LB trough and omitting the film compression process [60,97], which can further expand its application.

Space-confined self-assembled (SCSA) method

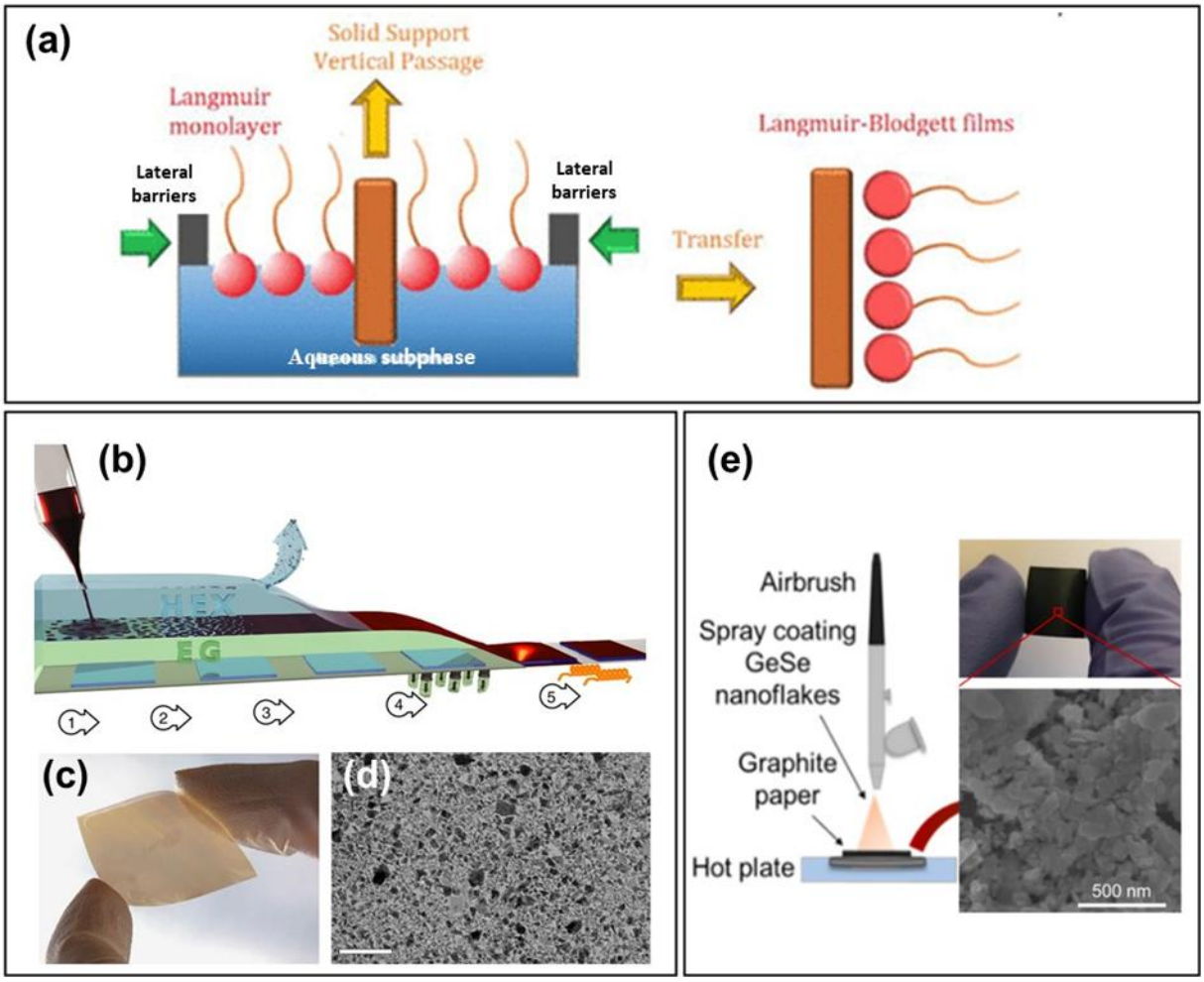

Fig. 8. (a) The scheme of Langmuir-Blodgett method with a typical Langmuir trough [96]. (b-d) The space-confined self-assembly approach for WSe_2 thin-film deposition [29]. (b) The schematic diagram of the film deposition method. (c) The photograph of a single-flake-layer WSe_2 thin film deposited on flexible ITO-coated PET plastic, and (d) A representative TEM image of a single-flake-layer WSe_2 film. The scale bar is 2 mm. (e) GeSe film produced by spray-coating the GeSe nanoflakes onto a graphite paper substrate, photograph of a GeSe photoelectrode, which was manually bent to its mechanical flexibility, and its corresponding top-view SEM image. Figures were adapted from: b-d [29], e [98], respectively.

Self-assembling nanoparticles at liquid-liquid interface is also a useful technique suitable for film preparation. In a typical process, the nanoparticles, dispersed into a hydrophilic medium, are driven towards a hydrophilic/hydrophobic interface through stirring or with an inducing agent [99,100]. However, the solvent-exfoliated TMDCs nanoflake suspensions have poor stability in most solvents. Sivula's group for example, applied this technique for film preparation

of TMDCs, but formed inhomogeneous films. Later, they developed this method by confining the TMDCs nanoflakes at the interface of two immiscible non-solvents, achieving uniform and continuous films [22,29,58,101]. The scheme of the developed method is shown in **Fig. 8b**, employing WSe_2 as an example here [29], which includes 5 steps: i): injection of WSe_2 nanoflakes dispersion; ii) nanoflake confinement and self-assembly; iii) hexane removal; iv) ethylene glycol removal and film deposition; v) drying at 150 °C. A photograph of SCSA film of WSe_2 flakes on flexible ITO-coated PET substrate is shown in **Fig. 8c**, and a homogeneous film over a large area (7.5 cm^2) is presented. Moreover, they scaled up the area to 22.5 cm^2 using this method. **Fig.8d** is a representative TEM image of SCSA-WSe_2 film, and no significant aggregation or restacking of the flakes is observed.

Spray coating method

Spray coating is a deposition technique where the coating materials are typically dispersed in a solvent medium and deposited on rigid or flexible substrates by using a spray gun to fabricate layers/films structures [98,102]. One representative example is shown in **Fig. 8e**, where the GeSe nanoflakes were spray-coated on a graphite paper substrate, and its corresponding top-view SEM image was also presented in the top-right figure [98]. A heating step is commonly used during the spray coating process to evaporate the solvents and eliminate the interlayer strain [71]. The film quality, such as the thickness and loading, can be tuned by changing the number of spray-coating cycles [103].

2.5. SnSe as a promising photocathode material

SnSe is a binary group IV-VI monochalcogenide with an orthorhombic phase structure [91,104]. It has been considerably studied in the thermoelectric community because of its ultralow lattice thermal conductivity [105,106]. As a layered SC, due to the weak van der Waals force within its interlayers, the bulk SnSe crystals can be cleaved to nanoflakes with different thicknesses, resulting in a tunable bandgap (0.9–1.8 eV, corresponding to the thickness from bulk to monolayer). Furthermore, it has a p-type semiconducting nature with high absorption coefficient of 10^5 cm^{-1} [107]. All these properties enable SnSe an appropriate material for photovoltaic and optoelectronic devices [108,109]. In addition, the other merits, such as the earth-abundance of both Se and Sn elements, and the comparatively low toxicity of SnSe, make this material even more attractive. After reviewing the reports, we have found that SnSe-based materials have been

used for solar cell [110], photocatalysis [111], and PEC OER applications [112–116], while only limited number of papers investigated the PEC HER performance of SnSe [62], there is a strong need to further study this application of SnSe.

So far, SnSe has been synthesized by using different methods, such as CVD [117], electrodeposition [64,118], hydrothermal method [119], chemical (Li-intercalation) exfoliation [120,121], and LPE [70]. As discussed in the **2.3 section**, some synthesis methods have their own drawbacks, which can affect the yield and crystallinity of the obtained materials. Therefore, from the view of cost and product yield, among these approaches, LPE is considered as the suitable method to prepare SnSe nanoflakes. Hence, this method was employed in our study. The LPE method has been used to prepare the high-quality crystalline SnSe nanoflakes in pure IPA, showing tunable bandgap and optical absorption performance by adjusting the nanoflake thickness [107]. Besides, another work reported that they prepared few-layer SnSe nanoflakes from different solvents (e.g., NMP, ethanol, and IPA), and a thickness-dependent bandgap was proved [70].

Compared to CVD, the hydrothermal method is also suitable for synthesizing SnSe flakes because of the lower energy cost. The nanomaterials synthesized by different approaches have different morphologies, surface conditions, and crystallinities, which might result in different PEC performance [13,122]. Therefore, we aimed to study the PEC HER activity of SnSe flakes prepared by different methods, namely LPE and hydrothermal methods. These results will highlight the potential of SnSe electrodes in the PEC HER application, offering new avenues for exploring PEC processes on such metal chalcogenide electrodes.

2.6. GaTe as a promising photocathode material

Lately, III–VI group monochalcogenides, such as indium selenide (InSe) and gallium telluride (GaTe), have attracted extensive attention because of their excellent optical and electronic properties [123–125].

GaTe is a van der Waals SC, and possesses a direct bandgap which can be tuned between 1.7 to 2.1 eV by adjusting the flake thickness [89,126–128]. Also, it has a high absorption coefficient (10^4 cm^{-1}) [129]. All these merits make GaTe a good material for photovoltaic and optoelectronic devices. So far, numerous devices based on GaTe nanoflakes, nanowires, and

multilayers have been fabricated and applied for various applications, e.g., photodetector [130–132], transistor [133], supercapacitor [134], and solar cell [125,135]. Additionally, GaTe utilized as a catalyst in photocatalysis has also been investigated [136–139]. For example, Tien et al studied the photocatalytic dye degradation activity of bulk GaTe nanosheets and nanowires [136]. Moreover, the band diagram of GaTe was fabricated by theoretical calculation, revealing a more negative CB than H^+/H_2 (–1.1 eV vs. 0 eV) [137,138]. Later, the photocatalytic HER performance of GaTe was tested experimentally [138]. The heterostructure of GaTe/ZnO was fabricated and used for PEC HER application, achieving seven times higher photocurrent than bare ZnO [140]. These results demonstrate that GaTe is a promising material in the field of HER. While we notice that all published reports about GaTe are based on either bare or the heterostructure of the bulk GaTe, the PEC applications of exfoliated bulk GaTe have not been reported, it's highly recommended to study the PEC HER behavior of GaTe nanoflakes.

GaTe has been synthesized by different approaches, such as bottom-up methods (e.g., CVD and self-flux (using Ga and Te powder) [141,142]), and top-down methods generally referred to as exfoliation [89,127,133,143,144]. The latter method includes ME [89,133,143] and LPE [127,134,144], which require more simple setups and less energy consumption compared to bottom-up methods. Therefore, the exfoliation was employed to prepare GaTe flakes in my PhD studies.

As discussed in the section of *Microelectrodes-based PEC studies*, the flake-based microelectrodes were fabricated to reveal the fundamental questions about layered materials, for example the thickness-dependent EC/PEC properties [23,56]. Reviewing the reports, the PEC performance of GaTe microelectrode has not been studied yet, therefore, the ME-prepared GaTe flakes were constructed as microelectrodes, meanwhile its thickness-dependent PEC HER performance was explored in our study. To scale up the electrode size, the GaTe macroelectrodes were assembled by using LPE prepared GaTe flakes. Several "green" solvents, such as ethanol [145], IPA [134,144], and water/ethanol mixtures [127], were employed for the exfoliation of GaTe. In our study, IPA was used as the solvent for the LPE process of GaTe crystals.

2.7. Other promising metal chalcogenides as photoelectrode materials

Except SnSe and GaTe materials, we have studied other layered SCs such as GeS, As_2S_3, and Cu_2S for PEC HER application in my doctoral projects as well, as their CB positions are more negative than H^+ reduction potential [95,137,146–164], indicating they are thermodynamically suitable for HER. Their band positions are shown in **Fig. 9.**

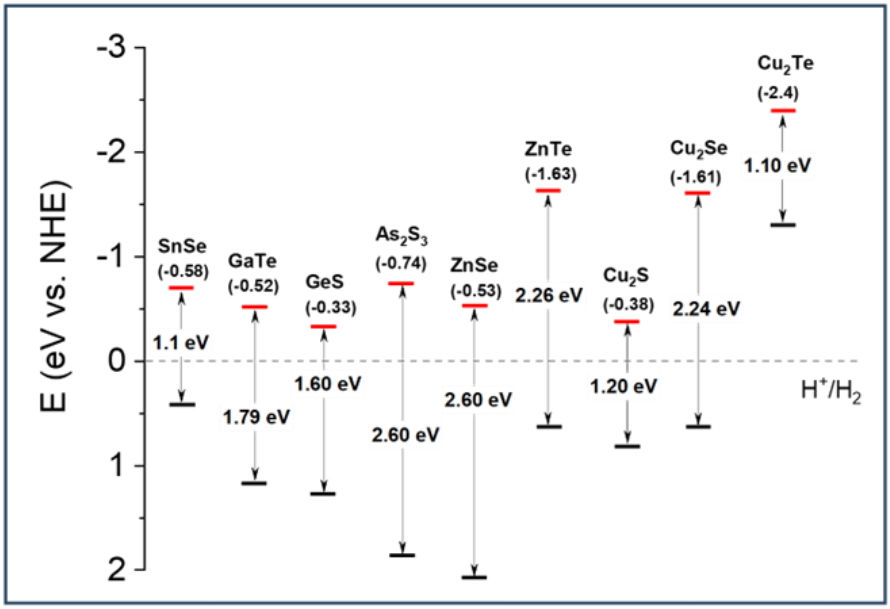

Fig. 9. The energy band diagrams related to the NHE at pH=0 of SCs we used. The red and black lines represent the CB and VB positions of SCs, respectively. The values shown in the figure were averaged from several data points from the literature for each SC.

Germanium sulfide (GeS)

Recently, GeS, as a p-type layered SC with an orthorhombic structure, has attracted great attention due to its direct bandgap of 1.65 eV in bulk, and a high electron mobility (10^3 cm^2 V^{-1} s^{-1}) and tunable electronic/optical properties [165]. These properties enable GeS used for various applications, such as photodetectors [162,166], photocatalytic/electrochemical HER [163,167,168], and transistors [164]. Additionally, the earth-abundant and environmentally friendly nature of GeS makes it suitable for practical use [169]. The PEC HER performance of GeS is rarely reported, therefore, it is critical to study its PEC HER activity, which can help to broaden the family of layered SC for solar energy conversion techniques.

GeS layers are bonded by weak van der Waals force, which can be peeled by exfoliation [85,164,170]. For example, Matsuda et al. prepared GeS flakes by using ME method, and

reported its anisotropic and thickness-dependent optical properties [170]. Besides, GeS crystals can be exfoliated in solvents with different surface tensions, such as ethanol (22.1 mN m^{-1}), acetone (25.2 mN m^{-1}), and IPA (23 mN m^{-1}) [85,162], providing a pathway for scalable production of GeS flakes.

Arsenic(III) sulphide (As_2S_3)

As_2S_3 is a p-type layered material with a monoclinic structure, and has an optical indirect band gap of 2.6 eV. It has low interlayer binding energy (van der Waals force), which can be peeled into thin flakes by exfoliation. As_2S_3 as a catalyst for photocatalytic HER has been expected [146,171]. Also, it shows photoconductivity [172,173], making it a candidate for PEC applications. While its PEC HER application is rarely studied, in this regard, it is desired to study the PEC activity of As_2S_3. It is worth mentioning that additional safety precautions are required when using As_2S_3 because of its toxicity [174].

Zinc telluride/Zinc selenide (ZnTe/ZnSe)

Among the zinc chalcogenide-based catalysts, ZnX is an n-type SC when X is O, S, and Se, while ZnTe is a p-type SC [175].

ZnSe is a n-type layered SC with a bandgap of 2.6 eV, and its CB and VB positions straddle the reduction and oxidation potentials of water, enabling ZnSe suitable for the water splitting process [149]. So far, there have been a lot of reports about the photocatalytical/photoelectrochemical applications of ZnSe-based materials [147,149,176–178]. For example, Reisner's group synthesized ZnSe nanorods and applied them for photocatalytical HER, showing an activity approaching that of Cd-based materials, even without a co-catalyst. Rosei and co-workers fabricated InP/ZnSe heterostructure for PEC HER, achieving higher activity than that of bare InP [176]. Other heterostructure, like $Ni_{0.85}Se$/ZnSe [147] and $ZnIn_2S_4$/ZnSe [179], were also constructed. Besides, ZnSe is a stable and inexpensive SC, making this material more attractive to form heterostructures with other materials. We found the relative band edge potentials between SnSe and ZnSe (**Fig. 9**) are suitable for HER, hence, the heterostructure of ZnSe/SnSe was fabricated, and its PEC HER activity was investigated during my doctoral studies.

The p-type ZnTe material has a bandgap of 2.26 eV, which is a suitable candidate for photoelectric devices. Due to its relatively negative CB energy potential (−1.63 V vs. RHE) among many known p-type SCs so far [151], ZnTe has been widely used for PEC CO_2RR and HER [180,181]. However, there are still some shortcomings, such as the poor selectivity, low stability, and fast recombination of charge carriers, which need to be overcome. The strategies developed to solve these issues mainly include constructing heterostructures with other SCs, metal, or conductive polymers [181–186]. For example, the heterostructure of polypyrrole-coated p-ZnTe was fabricated and applied for PEC CO_2RR, showing the improvement in the catalytic activity in terms of the Faradaic efficiency, reaction selectivity, and production rate [183].

So far, ZnTe has been synthesized by a variety of approaches, for example, the hydrothermal method [184,187], hot injection [188], thermal evaporation method [150], and close spaced sublimation [186]. Reviewing the literature, we found that ZnTe prepared by the exfoliation method requires low energy cost, meanwhile, the PEC HER application of exfoliated ZnTe has not been reported yet. It is desired to study the PEC performance of exfoliated bulk ZnTe to broaden the opportunities of ZnTe material in the field of energy conversion applications.

Copper sulfide (Copper telluride, Copper selenide) (Cu_2S (Cu_2Se, Cu_2Te))

Cu_2S is a narrow bandgap SC (1.2 eV for bulk), which can absorb the sunlight in a wide wavelength range. It has a high absorption coefficient over 10^4 cm^{-1} and a high conductivity, allowing for efficient photogenerated charge transfer. Moreover, the Cu and S elements are earth-abundant and non-toxic. All these attributes favor Cu_2S to be a promising material for solar energy conversion. So far, Cu_2S has been employed for solar cells, photocatalysis [189,190], and counter electrode in quantum dot solar cells [191], while only a few studies reported its PEC applications. The heterostructure of Cu_2S/Cu_2O for example, was constructed by coating Cu_2S onto the Cu_2O photocathodes and used for PEC HER [192], showing better performance than bare Cu_2O. These results indicate the potential of Cu_2S as a promising material for PEC HER, thus, there is a strong need to further explore its PEC HER performance.

Cu_2Se and Cu_2Te have an indirect bandgap of 1.1−1.5 eV, and it has been widely used as a good absorber in photovoltaic devices [193,194]. Meanwhile, their CB positions are more

negative than H^+/H_2, making them great candidates for HER. While their practical application in PEC HER has rarely been reported [157,195], and in these reports, only the heterostructure of it was studied, the bare and exfoliated Cu_2Se and Cu_2Te have not been investigated. Regarding this, it is interesting to study the PEC HER performance of bare and exfoliated Cu_2Se and Cu_2Te.

3. Motivation and Aims

When I started my PhD studies in 2019, our initial goal was to **improve the performance of 2D semiconductor materials in PEC reaction**. To do this, we wanted to i) activate the inactive parts (e.g., basal plane) by depositing co-catalysts; ii) passivate the defects (like the edges) by decorating them with surfactants or other materials (e.g., Al_2O_3). While as the research progressed and new issues occurred, my doctoral goals became clearer. These aims can be summarized as follows:

i). To **find a suitable solvent for the LPE process of SnSe**. As far as we know, different solvents have different surface tensions, which can result in different interactions between crystals and solvents, consequently leading to nanoflakes with different sizes after LPE process. Therefore, we used different solvents in the LPE process, aiming to find out a suitable solvent for the LPE process of SnSe, and for achieving improved PEC HER activity.

ii). Another goal was to **study the effect of edge density on PEC activity of SnSe**. From the literature review, we found that the flake size (edge density) can affect its PEC performance. Therefore, a sieving process was used to separate the as-received commercial SnSe crystals into three size fractions before LPE, and the obtained flakes edge density can be tuned. The photocathodes made from them by spray coating method were tested for PEC HER application. The influence of flake edge density on the PEC HER performance of SnSe was investigated.

iii). To **study the effect of Pt co-catalyst on SnSe PEC HER performance.** Pt nanoparticles were deposited on SnSe photoelectrodes by photodeposition method, and the effect of different deposition factors, such as illumination time, the concentration of Pt precursor, and illumination intensity, on the PEC activity was investigated. Under optimal recipe, the role of Pt co-catalyst on the charge carriers transfer and recombination of SnSe photocathode was studied.

iv). To **investigate the PEC HER performance of micro- and macro-GaTe photoelectrodes**. To our best knowledge, exfoliated GaTe has not been studied in the PEC HER, therefore, it is desired to prepare GaTe nanoflakes and study its PEC performance in HER.

v). To **explore other new layered materials for PEC HER application**. There are many layered metal chalcogenides that have not been studied in the field of PEC HER. We aimed to process such materials into films and investigate their PEC HER behavior to expand the SC family for solar energy conversion applications.

4. Experimental

4.1. Materials

Commercial semiconductors

- Tin(II) selenide (SnSe, 99.999%, diameter ≤ 12 mm, Alfa Aesar)
- Gallium telluride (GaTe, ≥99.999%, Thermo Scientific)
- Zinc telluride (ZnTe, ≥99.99%, Thermo Scientific)
- Zinc selenide (ZnSe, ≥99.999%, Thermo Scientific)
- Germanium(II) sulfide (GeS, 99.99%, Sigma-Aldrich)
- Copper(I) sulfide (Cu_2S, ≥99.5%, Thermo Scientific)
- Arsenic(III) sulfide (As_2S_3, ≥99.999%, Thermo Scientific)

Synthesis of SnSe

- Tin(II) chloride dihydrate ($SnCl_2·2H_2O$, 99.99%, Sigma-Aldrich)
- Selenium (Se, 99.5%, Sigma-Aldrich)
- Sodium borohydride ($NaBH_4$, 99%, Sigma-Aldrich)

Synthesis of Cu_2S, Cu_2Se and Cu_2Te

- Copper(II) chloride ($CuCl_2$, 99%, Sigma-Aldrich)
- Thiourea (CH_4N_2S, ≥99%, Sigma-Aldrich)
- Ethylenediamine ($C_2H_8N_2$, EDA, ≥99%, Sigma-Aldrich)
- Copper powder (Cu, Analytical, Reanal)
- Copper foil (Cu, thickness=0.25 mm, 99.98%, Sigma-Aldrich)
- Copper(II) sulfate pentahydrate ($CuSO_4·5H_2O$, ≥98.0%, Sigma-Aldrich)
- Selenium dioxide (SeO_2, ≥99.9%, Sigma-Aldrich)
- Hydrazine monohydrate ($N_2H_4·H_2O$, N_2H_4 64-65%, reagent grade, 98%, Sigma-Aldrich)
- Tellurium powder (Te, powder, −200 mesh, 99.8%, Sigma-Aldrich)

Liquid solvents for liquid phase exfoliation

- Isopropanol (C_3H_8O, IPA, 99.5%, Sigma-Aldrich)
- Ethanol (C_2H_6O, EtOH, 96%, VWR)

- N-Methyl-2-pyrrolidone (C_5H_9NO, NMP, 95%, Sigma-Aldrich)
- 1,4-Dichlorobenzene ($C_6H_4Cl_2$, DCB, 99%, Merck)
- Dimethylformamide (C_3H_7NO, DMF, 99.9% VWR)

Photoelectrochemical characterization

- Lithium chloride (LiCl, 99.99%, Acros Organics)
- Hydrochloric acid (HCl, 37%, Szkarabeusz)
- Sulphuric acid (H_2SO_4, 95%, VWR)
- Methanol (CH_4O, ≥99.8%, VWR)
- Chloroplatinic acid hydrate ($H_2PtCl_6 \cdot xH_2O$, ≥99.9%, Sigma-Aldrich)
- Argon (Ar, 99.999%, Messer)

Substrates and its cleaning

- Glassy carbon (GC; 2 mm thick; Alfa Aesar)
- Indium tin oxide coated glass (ITO; 20 Ω/sq.; Präzisions Glas & Optik GmbH)
- Fluorine doped tin oxide coated glass (FTO; TEC15; 7 Ω/sq.; Sigma-Aldrich)
- SiO_2/Si wafer (Graphene Supermarket)
- Acetone (C_3H_6O, 99.5%, VWR)
- Alumina powder (Al_2O_3, 0.05 μm, Buehler)

All the chemicals were utilized without further purification, and all solutions were prepared using ultrapure deionized water (Millipore Direct Q3-UV, 18.2 MΩ cm).

4.2. Flake preparation

The preparation methods of SC materials in the form of bulk and/or nanoflakes used in my doctoral research were listed in **Table 3**, and the conductivity type of each SC, and the substrates used in the photoelectrode fabrication process were included here as well. Followingly, SnSe and GaTe were used as representative examples to explain how their bulk, nanoflakes, and photoelectrodes were prepared/fabricated.

Table 3. The preparation methods of SC materials (bulk and nanoflakes) that we used for PEC HER application.

Specimen	Conductivity type	Nanoflakes preparation method	Solvent for LPE	Electrode preparation method	Substrate
SnSe	p	LPE, hydrothermal	IPA/H_2O, IPA	m-LB, SP	GC
GaTe	p	ME, LPE	IPA	ME, SP	SiO_2/Si, GC
ZnSe (ZnTe)	n (p)	LPE	IPA, EtOH, EtOH/H_2O, NMP	m-LB	GC
Cu_2S (Cu_2Se, Cu_2Te)	p	LPE hydrothermal	IPA, EtOH	m-LB, SP	GC
GeS	p	LPE	EtOH, EtOH/H_2O, IPA, IPA/H_2O, DCB, NMP, DMF	m-LB	GC
As_2S_3	p	LPE	IPA, EtOH/H_2O	m-LB	FTO, ITO, GC

Liquid phase exfoliation (LPE)

The as-received SnSe (AR-SnSe) crystals were dispersed into IPA/H_2O mixture solvent with different IPA contents with an initial concentration of 5 mg mL^{-1}, using a 250 mL of round-bottom flask. Then the dispersion was purged with Argon for 10 minutes to remove the dissolved oxygen and sealed with parafilm, subsequently performed sonication for 12 h with a bath sonicator (Elmasonic P70H) operating at 37 kHz and 100% power, while keeping the bath temperature below 30 ^oC with a recirculating cooler system (J. P. Selecta, Dig-iterm TFT). Then the suspension was centrifuged at 100 g (Z366K, Hermle centrifuge) for 15 min at 15 ^oC. 90% of the supernatant was gently taken out with a pipette, leaving the sediment as obtained nanoflakes. The concentration of the obtained sediment from centrifuge was measured via the gravimetric analysis method [60]. The process scheme was shown in **Fig. 10**.

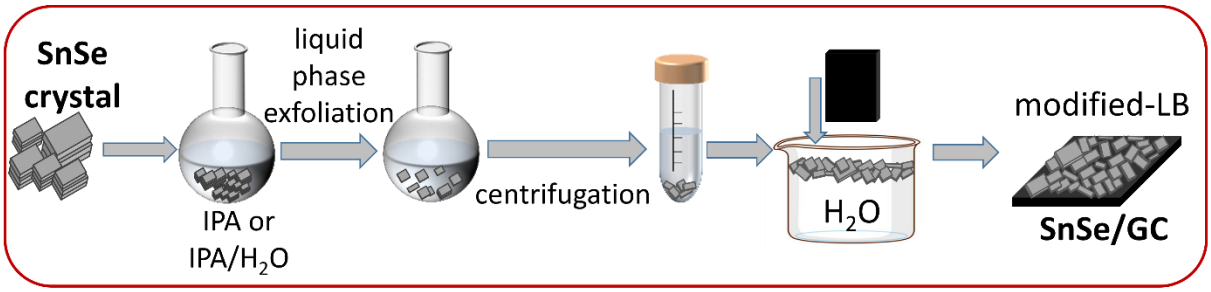

Fig. 10. Schematic illustration of liquid phase exfoliation of SnSe layered material, size selection of nanoflakes using centrifugation, and preparation of SnSe nanoflakes-based electrodes with modified Langmuir-Blodgett method [60].

A crystal size selection process was only performed on SnSe crystals with a sieving system (Blau-Metall, Inc., with 200 mm in diameter sieves of woven wire mesh) to separate the AR-SnSe crystals into different sized crystals before LPE process (shown in **Fig. 11**.). This step led to 3 different fractions of SnSe crystals with 0.16–0.4 mm, 0.69–1.6 mm and 1.6–12 mm, named as S-, M- and L-SnSe, respectively. SnSe nanoflakes were obtained by exfoliating above different sized crystals in pure IPA solvent, and the resulting fractions were denoted as S-, M-, and L-SnSe-IPA, respectively.

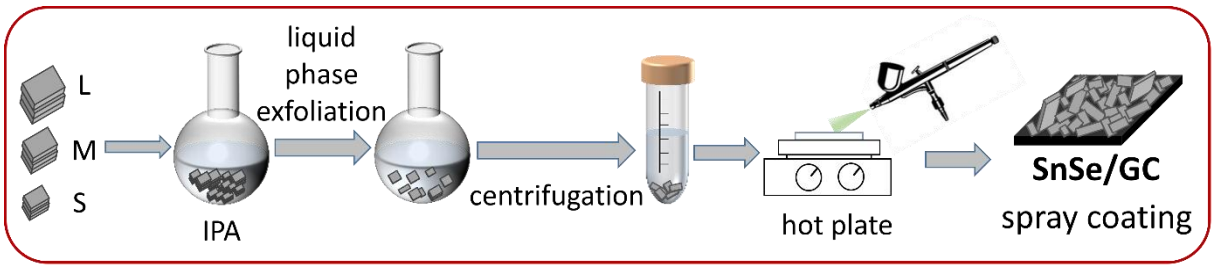

Fig. 11. Schematic illustration of size selection of SnSe crystals, liquid phase exfoliation of SnSe crystals, size selection of nanoflakes using centrifugation, and preparation of SnSe nanoflakes-based electrodes with spray coating method [60].

Mechanical exfoliation (ME)

SiO_2/Si wafer (Graphene Supermarket) was used as substrate for GaTe microelectrode. Prior to use, the substrate was ultrasonically cleaned in acetone and IPA for 5-5 min, respectively. Layered GaTe crystals were mechanically exfoliated into thinner nanoflakes using scotch tape. Then these nanoflakes were transferred onto SiO_2/Si substrate using a thermal release tape (Graphene Supermarket) at 105 ^oC on a hotplate (MCS78, CAT Scientific).

Hydrothermal method

SnSe nanosheets were synthesized via a hydrothermal method [95]. In brief, 451 mg $SnCl_2 \cdot 2H_2O$ was dispersed in 30 mL deionized water and was marked as solution A. Then, 250 mg $NaBH_4$ and 138 mg Se powder were dispersed into 30 mL deionized water and was heated to 80 ^oC until all powder was dissolved, marked as solution B. Then solution A and B were mixed and transferred into a Teflon-lined autoclave, kept at 200 ^oC for 16 h, followed by cooling down to room temperature. The as-obtained product was separated from the suspension by centrifugation, subsequently washed with deionized water and ethanol successively for three times, dried by Ar flow, and stored in a glass vial. The synthesis methods of Cu_2S (Cu_2Se, Cu_2Te) can be found in the literature [189,196–199].

4.3. Electrode preparation

Microelectrode preparation

The GaTe nanoflakes prepared by ME method were electrically contacted with carbon paste (Electron Microscopy Sciences) and copper wire (Cu, 99.99%, 0.15 mm diameter, Advent Research Materials Ltd), and were used as GaTe microelectrodes. **Fig. 12** shows the optical image collected by an optical microscopy (Nikon Eclipse LV100ND) of GaTe nanoflakes. The nanoflakes immobilized on the SiO_2/Si substrate were distinguishable due to the contrast in refractive indexes between GaTe and the substrate [131]. Moreover, the variations in color in the optical image indicate different thicknesses of GaTe nanoflakes.

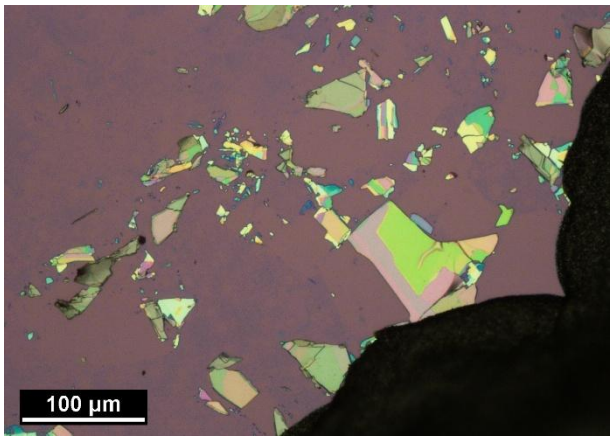

Fig. 12. The optical image of GaTe nanoflakes prepared by the ME method. Adapted from ref.[200].

Macroelectrode preparation

GC plate, ITO, and ITO were used as substrates for macroelectrode preparation. The substrates were sequentially ultrasonic cleaned in H_2O, IPA, and acetone for 5 minutes, respectively. GC plates need to be polished on alumina powder for 10 min before cleaning in the above solvents.

1）Modified Langmuir-Blodgett method (m-LB)

As shown in **Fig. 10**, a beaker filled with ultrapure deionized water was used as a trough, and the obtained SnSe suspension after centrifuge process was slowly dropped onto the surface of the water until a continuous film formed. Then, the GC substrate was inserted into the water and slowly fished up by a tweezer. Subsequently, the electrodes were dried on a pre-heated hotplate for a few minutes to remove the solvent traces and to enhance the adhesion between deposited nanoflakes and substrates.

2）Spray coating method (SP)

To better control the loading of SC on the substrates, SP method was employed to prepare macroelectrodes in some cases (**Table. 3**). The concentrations of specimen suspensions (obtained from the centrifugation) were adjusted to 2 mg mL^{-1} using the same solvents as LPE process in all cases. Then the SnSe suspensions were spray-coated on a pre-heated substrate using an Alder AD320 type airbrush. The precise loading of the SnSe nanoflake was monitored using an analytical microbalance (Mettler Toledo XPE-26 type). Before the spray coating process, the electrodes were masked with PTFE sealing tape (Thickness: 0,1 mm, Temperature resistant from −200 to +250 °C, VWR) to have an exposed surface area of 1 cm^2.

4.4. Co-catalyst deposition

Pt co-catalyst was photodeposited on the surface of SnSe from an aqueous solution containing 5 mM H_2PtCl_6, 5 vol% methanol, and 0.25 mM H_2SO_4. The solution was purged with Ar for 1 h to remove the dissolved O_2 before deposition. The Pt deposition recipe was optimized by using different H_2PtCl_6 concentrations (1, 5, 10 mM), illumination times (30, 60, 90 s), and illumination intensities (30, 44, 100 mW cm^{-2}). After Pt deposition, the SnSe electrodes were washed three times using ultrapure deionized water and then dried by Ar gas flow.

4.5. Physical characterization

Scanning electron microscopy (SEM)

The morphology and size of obtained nanoflakes were analyzed by SEM (Hitachi S-4700 Type II) equipped with energy dispersive X-ray spectroscopy (EDS) probe, and another SEM (Thermo Fisher Scientific Apreo C) equipped with Everhart–Thornley detector and a Bruker EDS probe. SEM images coupled with ImageJ software were used to estimate the average size of nanoflakes. The histogram distributions of nanoflake area and perimeter were conducted from over 100 nanoflakes in all cases.

Transmission electron microscopy (TEM)

TEM images were recorded by using a FEI Tecnai G2 X-Twin type instrument, operating at 200 kV. TEM images coupled with ImageJ software were used to determine the average size of nanoflakes. The histogram distributions of nanoflake area and perimeter were conducted from over 100 nanoflakes in all cases.

Atomic force microscopy (AFM)

The thickness of the nanoflakes was measured by using AFM (NT-MDT Solver), operating in the "tapping" mode with a silicon tip on a silicon nitride. The histogram distribution of nanoflake thickness was obtained from the analysis of over 100 nanoflakes.

X-ray powder diffraction (XRD)

XRD was employed to analyze the crystal structure and phase composition of the samples. XRD measurements were performed on a Rigaku Miniflex II instrument, operating with a Cu Kα, radiation source ($\lambda = 1.5406$ Å).

Raman spectroscopy

Raman spectroscopy was conducted to analyze the vibrational modes of samples on a Senterra II Compact Raman microscope (Bruker) with a $\lambda = 532$ nm green laser, operating at a power of 2.5 mW.

X-ray photoelectron spectroscopy (XPS)

The chemical state of elements of sample surface was analyzed by a SPECS XPS instrument equipped with a PHOIBOS 150 MCD 9 hemispherical analyzer. The analyzer was employed in

the transmission mode with 40 eV pass energy for the survey scans and 20 eV pass energy for the high-resolution scans. Charge referencing was done to adventitious carbon (peaked at 284.8 eV) on the sample surface as the reference in all cases. For spectrum evaluation, CasaXPS commercial software package was utilized.

Kelvin Probe measurement (KP)

Measurements were performed on a KP Technology APS04 instrument, coupled with a glove box (Mbraun, Labmaster Pro) in Ar atmosphere to construct the band diagram of bulk GaTe. The KP is placed in a Faraday cage where the illumination can be controlled. The sample was immobilized on a motorized (x, y, z) sample stage with transitional position control <300 nm. The contact potential difference (CPD) measurements were conducted to calculate the Fermi level (E_F), and the surface photovoltage spectroscopy (SPS), the ambient pressure photoemission spectroscopy (APS) were measured to determine the bandgap and conduction band (CB), respectively [201].

4.6. Photoelectrochemical measurements

Linear sweep photovoltammetry

Linear sweep photovoltammetry is a method that applies bias potential to the working electrode with a constant scan rate to one direction in a certain potential window, meanwhile irradiating the working electrode surface periodically. It is one of the key PEC characterization techniques to evaluate the PEC properties of a photoelectrode. The examples are shown in **Fig. 13,** the (a) p-type SC and (b) n-type SC are our prepared SnSe and ZnSe materials, respectively. From this technique, the following important information can be gained:

1) The conductivity type (p or n) of the SC can be indicated from the plot. p-type and n-type SCs give cathodic and anodic photocurrents, respectively.
2) The dark current, and photocurrent (which is the difference between dark current and total current) of the photoelectrode can be seen from one plot.
3) The flatband potential (which is the potential that needs to be applied to the SC to reduce the band bending to zero) of a SC can be estimated from photocurrent onset, which correlates to E_{VB} for a p-type SC and to E_{CB} for an n-type SC.

4) A maximum theoretical photocurrent can be possibly extracted from three-electrode measurements.
5) The shape of transient on the photovoltammogram profile can indicate if significant recombination happens at the SC/electrolyte interface, evident through spikes.

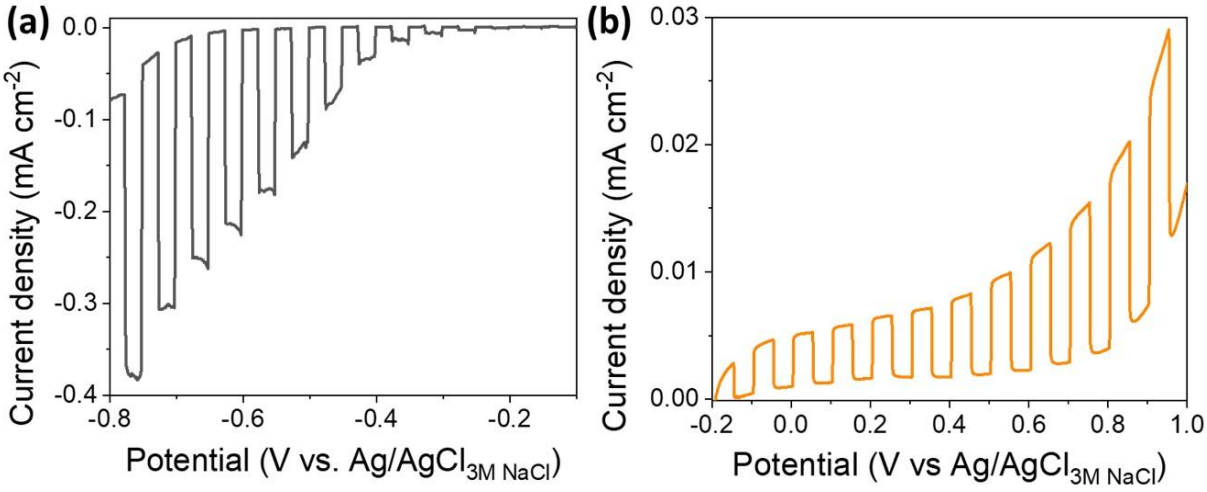

Fig. 13. The examples of linear sweep photovoltammograms, recorded for a (a) p-type SC and (b) n-type SC.

All the PEC measurements of microelectrodes were recorded by a PGSTAT302N potentiostat (Metrohm-Autolab) in a three-electrode configuration. GaTe nanoflake contacted with carbon paste on SiO_2/Si substrate was the working electrode, while Pt wire and Ag/AgCl as counter and reference electrodes, respectively. The electrolytes were injected into the micropipette via syringe, followed by the insertion of the counter and reference electrodes, and the optical fiber, the schematic illustration was shown in **Fig. 14**. Using a microinjector (PV820 Pneumatic PicoPump, WPI) with Ar gas, the electrolyte droplets were deposited onto the GaTe nanoflake surface. All potentials were measured against the Ag/AgCl reference electrode in 6 M LiCl. The PEC performance of GaTe microelectrodes was tested with 6 M LiCl/1 M HCl and 6 M LiCl droplets, respectively. All solutions were purged with Ar for 30 min to remove the dissolved O_2 from the solution before the PEC measurements. The linear sweep photovoltammograms were collected at 2.5 mV s^{-1} potential scan rate under chopped white illumination (Fiber-Lite DC950 Illuminator, 200 mW cm^{-2}, 10 s on/off).

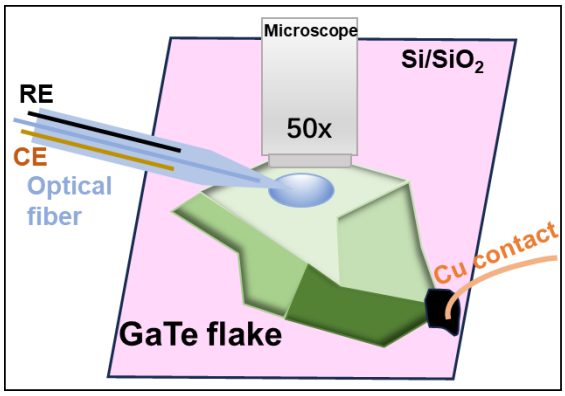

Fig. 14. Scheme of our photoelectrochemical-microscopy setup. Adapted from ref.[200].

All the PEC measurements of macroelectrodes were performed on a Bio-logic SAS VMP-300 type electrochemical station. A custom-designed, three-electrode one-compartment glass cell was used to measure the PEC performance. SC-coated GC was the working electrode, while GC plate, and Ag/AgCl were counter and reference electrodes, respectively. Ar-saturated 0.5 M H_2SO_4 solution was employed as electrolyte. Linear sweep photovoltammograms were recorded with a scan rate of 2.5 mV s^{-1} with chopped illumination (Newport LCS-100 solar simulator, 100 mW cm^{-2}, 10 s on/off). Long term chronoamperometry was performed for 1 h in Ar-saturated 0.5 M H_2SO_4, under chopped illumination (30 s on/off) at −0.54 V vs. RHE.

To determine the Faradaic efficiency (FE), another chronoamperometry (1 h duration) was conducted on GaTe macroelectrodes at −0.79 V vs. RHE under chopped 10 sun illumination (on/off at every 30 s), during which the evolved gas products were collected for analysis. The hydrogen generated during the PEC reaction was quantified using gas chromatography (Shimadzu GC-2010 Plus) equipped with a barrier discharge ionization detector. Gas separation was achieved using a Restek ShinCarbon ST column with ultra-high-purity helium (6.0 grade) as the carrier gas. Samples were taken at regular intervals using an automated 6-port valve. The sealed cathode compartment of the H-cell was directly connected to the gas chromatography injection unit, enabling on-line hydrogen detection. To prevent products mixing, a Nafion membrane was used to separate the anode and cathode compartments. This sealed cathode compartment allowed the accumulation of hydrogen in the 50 mL gas-phase volume. Prior to each injection, a peristaltic pump (Ismatec, ISM831C) was employed to ensure homogeneous mixing of hydrogen in the gas phase. The FE values of the product were calculated as the ratio of charge consumed for the product formation to the total charge passed.

All measured potentials were adjusted to the RHE reference scale by applying the equation of $E_{RHE} = E_{Ag/AgCl} + 0.210\ V + 0.059 \times pH$. All currents were normalized to the geometric electrode area.

Incident photon-to-current efficiency (IPCE)/External quantum efficiency (EQE)

IPCE/EQE is one of the most significant diagnostic figures of merit for PEC devices. It is a measurement of the ratio of the photocurrent to the rate of incident photons as a function of wavelength.

In a PEC system, IPCE data are generally derived from chronoamperometry measurements. A constant potential is applied on the working electrode while measuring the currents that arise by illuminating the electrode surface with a monochromatic light at various wavelengths. The photocurrent is the difference between the steady state current under monochromatic illumination and the steady state background current. All photocurrents were normalized to the geometric surface area of the electrodes. The illumination density is measured before and after the chronoamperometry test using Si detector. Then IPCE value can be calculated via the following equation:

$$\mathrm{IPCE} = \mathrm{EQE} = \frac{number\ of\ electrons}{number\ of\ photons} = \frac{j * 1239.8}{P * \lambda} \qquad (2)$$

where j, P, and λ represent the measured photocurrent density (mA cm^{-2}), monochromated illumination power intensity (mW cm^{-2}), and wavelength (nm), respectively.

Several useful parameters can be derived from IPCE measurement:

1) The wavelength-range, in which the sample is photoactive – ideal if this wavelength window and the peaked value of the curve overlap with the absorption spectrum of sample.
2) The bandgap of SC of interest can be estimated by fitting a linear to the cutoff-region of the IPCE curve.
3) The photocurrent under actual solar irradiation can be predicted by integrating the IPCE data over the solar spectrum.

IPCE measurement was carried out on a Newport Quantum Efficiency Measurement System (QEPVSI-B) in the same cell configurations as in the case of linear sweep

photovoltammetry. The resolution was kept at $\Delta\lambda$ = 20 nm for macroelectrodes and $\Delta\lambda$ = 50 nm for microelectrodes. Measurements were carried out in 0.5 M H_2SO_4 solution for macroelectrodes, using 6 M LiCl/1 M HCl droplets for microelectrodes. All IPCE data were recorded after Ar-purging the electrolyte solution for 1 h to remove O_2 from the solution.

Intensity modulated photocurrent spectroscopy (IMPS)

IMPS is a useful technique to study the charge carrier dynamics of photoactive materials under irradiation. A base light intensity is used to create a steady-state situation, and a small, sinusoidally modulated intensity is superimposed and the corresponding modulated photocurrent is recorded. The results are typically illustrated by a plot of the imaginary versus the real part of the complex transfer function, dividing the resulting modulated photocurrent by the modulated light intensity [202,203]. A representative IMPS plot of n-SC is shown in **Fig. 15**, ω, k_{tr}, and k_{sr} represent frequency, rate constant for charge transfer, and surface recombination, respectively, which can be derived from IMPS profiles. The relative transfer efficiency can be calculated by the equation:

$$\eta_{tr} = \frac{k_{tr}}{k_{tr} + k_{sr}} \qquad (3)$$

IMPS was conducted on the SnSe-based macroelectrodes with the same configuration as in the case of linear sweep photovoltammetry, employing an AUTOLAB PGSTAT302N potentiostat equipped with a FRA32 module and a light-emitting diode (LED) driver kit (Metrohm-Autolab). A 10% light modulation of the original intensity was used for all experiments, and the frequency of the modulation was swept from 20 kHz down to 0.1 Hz, in Ar-saturated 0.5 M H_2SO_4 solution. The resolution was kept at ΔV = 50 mV under the potential window between −0.24 V and −0.67 V vs. RHE.

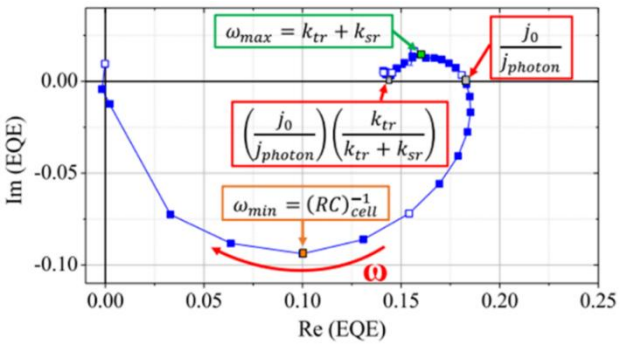

Fig. 15. IMPS result of a n-SC [203].

The Cole–Cole plot is the plot of the imaginary part of impedance against the frequencies, which can be derived from IMPS results, and a representative plot of SnSe is shown in **Fig. 16**. The peak at high frequencies between 10^3 and 10^4 Hz can be explained by the charge transport in the semiconductor layer [204].

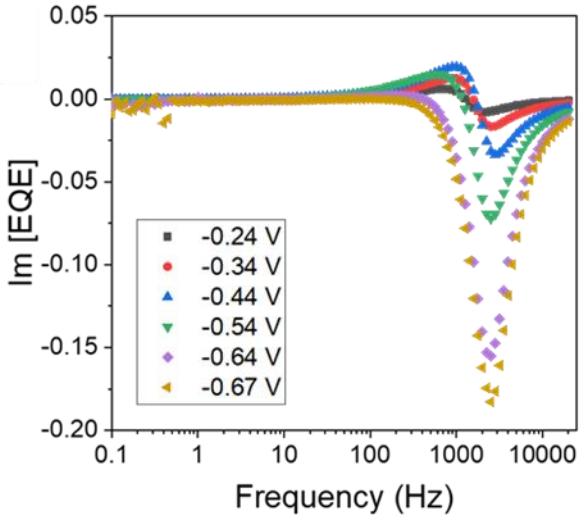

Fig. 16. Cole–Cole plots of bare SnSe electrode as the function of the applied potential derived from our measured IMPS results [60].

5. Results and Discussion

This chapter describes the characterizations of our prepared SCs and the investigation of their PEC activity in HER. The influence of several factors, such as the solvents used for LPE process and co-catalyst on SnSe catalytic performance, was studied and discussed. The effect of preparation methods (ME and LPE) of GaTe nanoflakes on PEC HER activity was investigated. Some other promising SCs were also tested for PEC HER application.

5.1. SnSe flakes activity for photoelectrochemical hydrogen evolution

5.1.1. The effect of LPE solvents on PEC HER performance of exfoliated SnSe

SnSe nanoflakes were prepared by the LPE of AR-SnSe crystals in IPA/H_2O mixtures with different IPA contents. The schematic illustration in **Fig. 10** (in the **Experimental** part) demonstrated how the photoelectrocatalysts, e.g., flakes and electrodes, were prepared and fabricated.

SEM and AFM were employed to characterize the morphology of the SnSe flakes produced by exfoliation. **Fig. 17a** and **b** present the SEM and AFM images of IPA-SnSe sample, showing angular shape. To quantify the as-resultant SnSe flake size (i.e., perimeter, area, and thickness), the area and perimeter were obtained from SEM images, and the thickness was determined from AFM. More than 100 flakes were evaluated here. The average area and thickness of IPA-SnSe and IPA/H_2O-SnSe were 4.0 ± 1.3 μm^2, 2.8 ± 0.9 μm^2, and 297 ± 189 nm, 266 ± 119 nm, respectively. **Fig. 18** shows the statistical analysis of the flake size characteristics. The log-normal distributions were found for these flake parameters, as the exfoliation follows a linear fragmentation model (i.e., a process which is driven by an external force, like ultrasonication) [205,206]. **Table 4** lists the mode values for the morphology features. The flakes exfoliated from IPA/H_2O have a larger average perimeter, area, and thickness than those prepared from pure IPA. Furthermore, the edge density of SnSe flakes was determined by dividing the perimeter by the area, and the IPA-SnSe specimen showed a higher edge density than that of IPA/H_2O-SnSe, which was consistent with reported studies that smaller-sized flakes generally have higher edge density. The flake edge density can significantly affect the PEC activity [22,48].

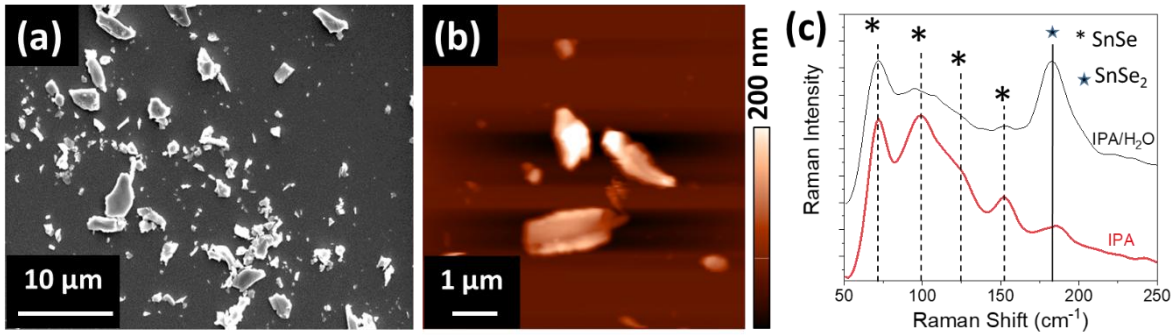

Fig. 17. Morphological and structural characterizations of the IPA-SnSe samples. (a) SEM and (b) AFM images of selected nanoflakes exfoliated from pure IPA. (c) Raman spectra of SnSe samples exfoliated in different solvents. The dashed, and solid lines denoted the SnSe, and $SnSe_2$ vibration bands, respectively [60].

Raman spectra were recorded to analyze the atomic vibrational modes in the SnSe flakes exfoliated in different solvents (**Fig. 17c**). The bands at 72.0, 99.1, 124.5, and 152 cm^{-1} were found in both of the specimens, which corresponded to A^1_g, B^3_g, A^2_g, and A^3_g vibrational modes of SnSe, respectively [207]. The peak at ~182.5 cm^{-1} was ascribed to the Raman active A^1_g mode of $SnSe_2$, representing the in-plane vibrations [208]. The A^1_g mode is more significant for IPA/H_2O-SnSe sample compared to IPA-SnSe. The presence of $SnSe_2$ phase in SnSe nanostructure has been found earlier [104,209]. $SnSe_2$ is reported as an n-type SC with a bandgap of 1.5–2.2 eV (depending on the thickness) [210–212], which can be formed through the nonstoichiometric combination of Se and Sn, or the localized phase segregation during the formation process of SnSe [213,214].

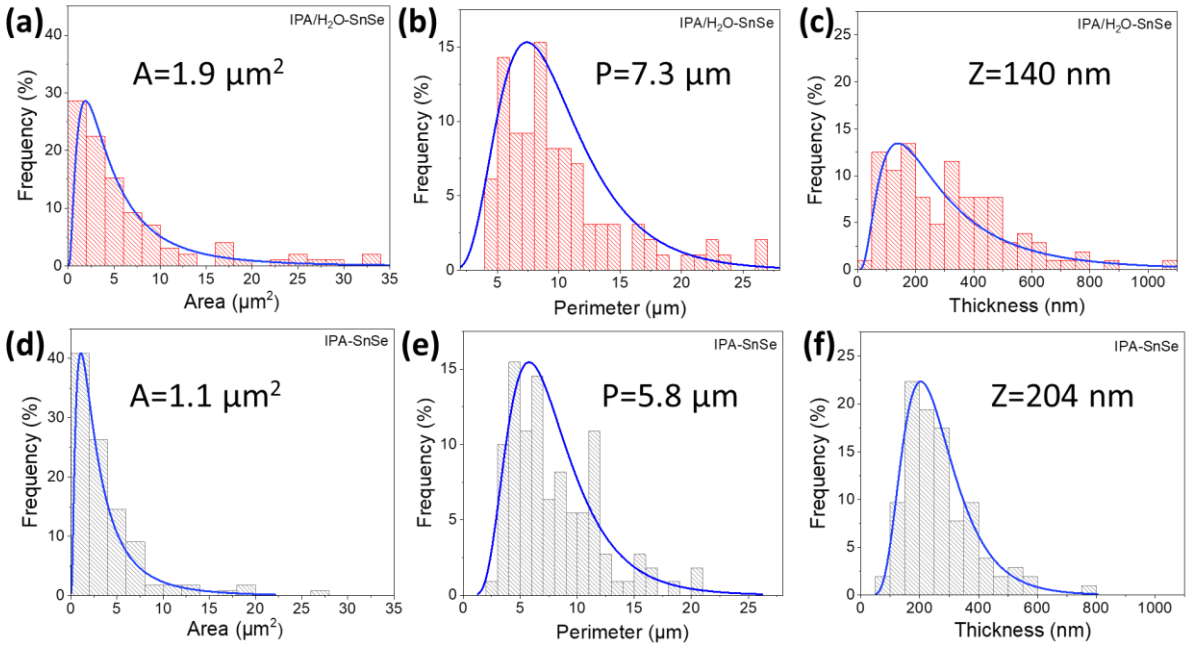

Fig. 18. Statistical analysis on (a, d) area, (b, e) perimeter, and (c, f) thickness of different SnSe dispersions, exfoliated using IPA/H_2O (1:3 ratio) (a-c) and IPA/H_2O (1:0 ratio) (d-f). The number insert is the peaked value of the distributions [60].

Table 4. The peaked area, perimeter, thickness, and edge density (perimeter/area) morphological properties for IPA/H_2O and IPA solvents produced SnSe nanoflakes [60].

Fractions	**Area (μm^2)**	**Perimeter (μm)**	**Thickness (nm)**	**Edge density**
IPA/H_2O-SnSe	1.9	7.3	140	3.8
IPA-SnSe	1.1	5.8	204	5.3

Linear sweep photovoltammetric curves were recorded to evaluate the PEC performance of SnSe film (prepared by m-LB method) in HER. **Fig. 19a** presents the linear sweep photovoltammogram of IPA-SnSe electrodes (SnSe loading: 0.28 ± 0.06 mg cm^{-2}) and IPA/H_2O-SnSe (SnSe loading: 0.29 ± 0.03 mg cm^{-2}). Both showed p-type photoactivity with increased currents at more negative potentials. The photocurrent was obtained by subtracting the dark current from the total current on the photovoltammograms. It is clear to see that the IPA-SnSe electrode gave higher photocurrent density compared to the IPA/H_2O-SnSe one, but with a higher dark current which probably resulted from the higher edge density of IPA-SnSe flakes [215]. As reported in studies, the presence of $SnSe_2$ in the SnSe flakes might contribute to the enhanced PEC performance [213,216]. While the $SnSe_2$ as the secondary phase breaks

the uniform nanostructure of SnSe, creating more defects inside of SnSe and acting as the recombination centers for the photogenerated charge carriers [217]. As the Raman spectra (**Fig. 17c**) show, more $SnSe_2$ was observed in the IPA/H_2O-SnSe sample.

To investigate the effect of the LPE solvent on the PEC performance of resultant SnSe nanoflakes, four IPA/H_2O mixtures with different IPA contents were utilized as LPE solvents. The photocurrent density values were decreasing as lowering the IPA content in the IPA/H_2O mixtures (**Fig. 19b**). The IPA/H_2O (1:0) electrodes presented ten times higher photocurrent density (1.18 vs. 0.11 mA cm^{-2}) at −0.69 V vs. RHE, compared to IPA/H_2O (1:3) case. The average values and error bars shown in **Fig. 19b** at four different potentials were calculated from three replicate electrodes for each case. The difference in PEC activity can be explained by the different surface tensions of the liquid mixture of IPA/H_2O with different mixing ratios, which in turn leads to different interactions between the SnSe crystals and the solvents during the exfoliation. This can lead to different flake morphologies and product yields [218]. The overall yield, determined by using the equation: overall yield = mass of flakes/starting crystal mass [82], was higher for IPA-exfoliated SnSe (63%) compared to IPA/H_2O-exfoliated SnSe (25%).

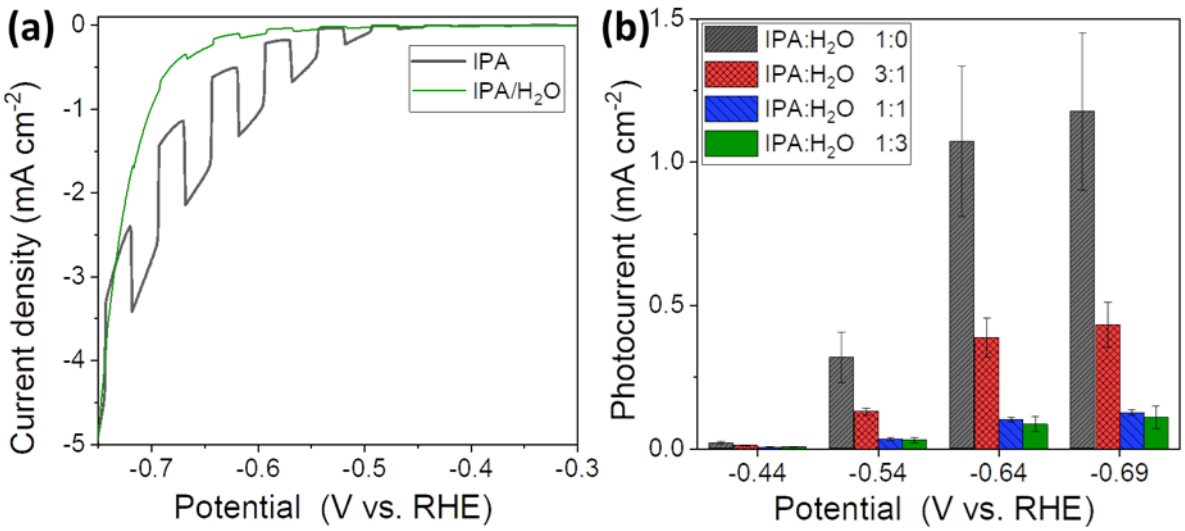

Fig. 19. (a) Linear sweep photovoltammograms of SnSe electrodes fabricated from SnSe flakes [the flakes were obtained by exfoliating commercial SnSe crystals in different IPA/H_2O mixtures (IPA: H_2O = 1:0 and 1:3)] at 2.5 mV s^{-1} sweep rate, in Ar saturated 0.5 M H_2SO_4 solution under chopped 1 sun illumination. (b) The bar diagrams of photocurrent density of SnSe electrodes plotted at four potentials. SnSe electrodes were fabricated from SnSe flakes exfoliated in different IPA/H_2O mixtures (IPA: H_2O = 1:0, 3:1, 1:1, 1:3). The averaged values and error bars were obtained from three replicate electrodes for each case [60].

5.1.2. The effect of flake edge density on PEC HER performance of SnSe

Regarding the reports, applying a sieving technique to the flake selection process can result in flakes with tunable edge density [22]. Therefore, to prepare SnSe flakes with different edge densities, a sieving-based method was applied to prepare SnSe crystals with controllable crystal size before liquid phase exfoliation. These SnSe crystals after size-selection (noted as L-, M-, S-SnSe) were exfoliated in IPA, as demonstrated in **Fig. 11 (**in the **Experimental** section). The obtained electrodes made from these crystals were named as L-IPA-, M-IPA-, S-IPA-SnSe. As shown in **Table 5**, the overall yield values of L-, M-, S-IPA-SnSe increase with decreasing the initial SnSe crystal size. TEM and AFM images indicated that all flake specimens had angular shape (**Fig. 20**) and smaller size (**Fig. 21**, **Table 6**) compared with those produced by exfoliating the AR-SnSe crystals. In addition, the S-IPA-SnSe specimen had a more monodispersed distribution than the other two specimens, which may trace back to the original narrower crystal size distribution of S-SnSe. All SnSe flakes had similar morphological characteristics, and only the edge density increased as the initial SnSe crystal size decreased.

Table 5. The overall yield of SnSe fractions exfoliated in IPA [60].

Fractions	**Overall yield (%)**
L-IPA-SnSe	5.6 ± 0.2
M-IPA-SnSe	17.1 ± 0.8
S-IPA-SnSe	85.3 ± 8.5

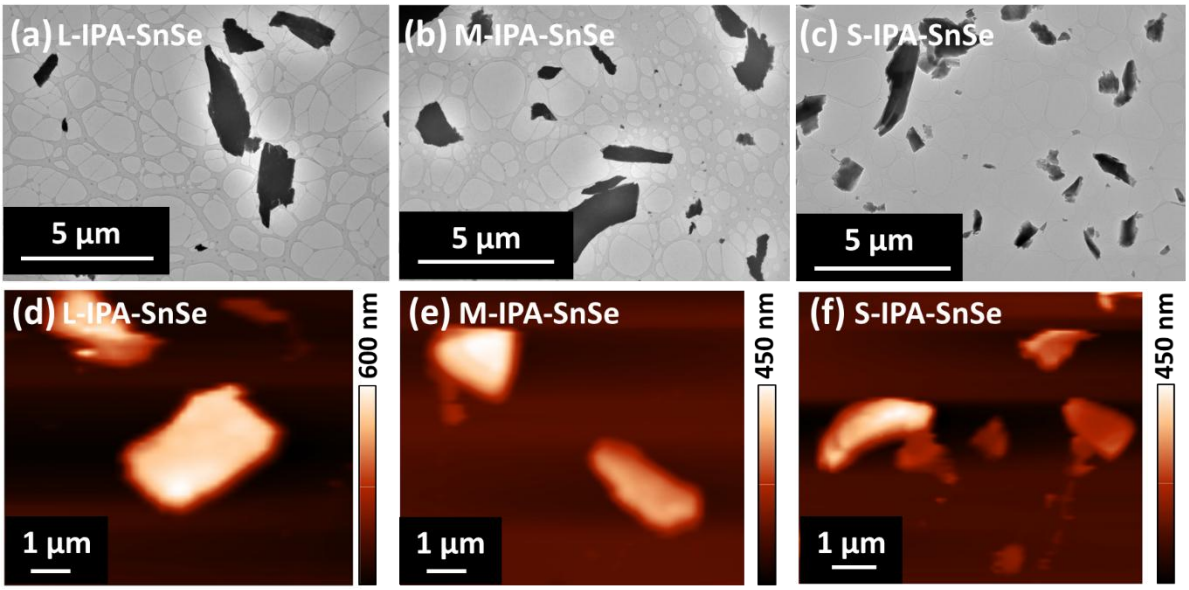

Fig. 20. Morphological characterization of the L-, M-, S-SnSe flakes exfoliated in IPA. (a, b, c) TEM, and (d, e, f) AFM images of selected flakes. (L-IPA-SnSe: a, d), (M-IPA-SnSe: b, e), and (S-IPA-SnSe: c, f) [60].

Table 6. The peaked area, perimeter, thickness, and edge density (perimeter/area) morphological properties of SnSe flakes obtained by exfoliating size separated L-, M-, S-SnSe [60].

Fractions	Area (µm^2)	Perimeter (µm)	Thickness (nm)	Edge density
L-IPA-SnSe	0.7	2.9	357	4.4
M-IPA-SnSe	0.6	2.8	286	4.7
S-IPA-SnSe	0.1	1.7	272	14.2

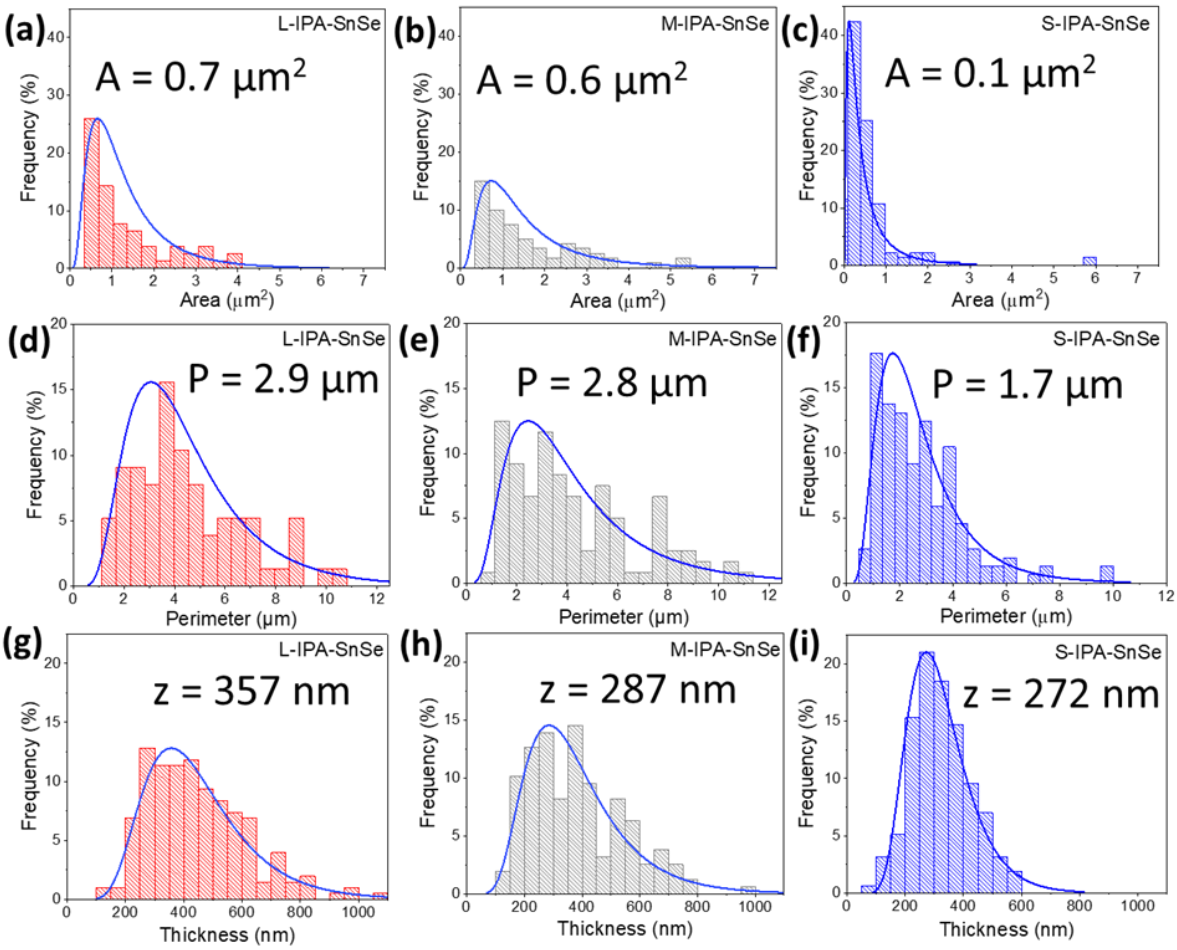

Fig. 21. Statistical analysis on (a, b, c) area, (d, e, f) perimeter, and (g, h, i) thickness of different IPA-SnSe dispersions, exfoliated using L-SnSe crystals (L-IPA-SnSe: a, d, g), M-SnSe crystals (M-IPA-SnSe: b, e, h), and S-SnSe crystals (S-IPA-SnSe: c, f, i) [60].

XRD was performed to determine the structural properties of the SnSe crystals and nanoflakes. As shown in **Fig. 22a**, the XRD pattern of L-SnSe crystals contains SnSe and $SnSe_2$ phases, indicating $SnSe_2$ as the second phase in the initial SnSe crystals. Besides, **Fig. 22b** shows the SnSe nanoflakes prepared from different sized crystals have $SnSe_2$ phase in the structure, which are in good agreement with Raman spectra results (**Fig. 17c**). These results demonstrated that $SnSe_2$ phase is from the initial crystals ($SnSe_2$ can be formed by the nonstoichiometric combination of Se and Sn, or the localized phase segregation during the formation process of SnSe) [213,214].

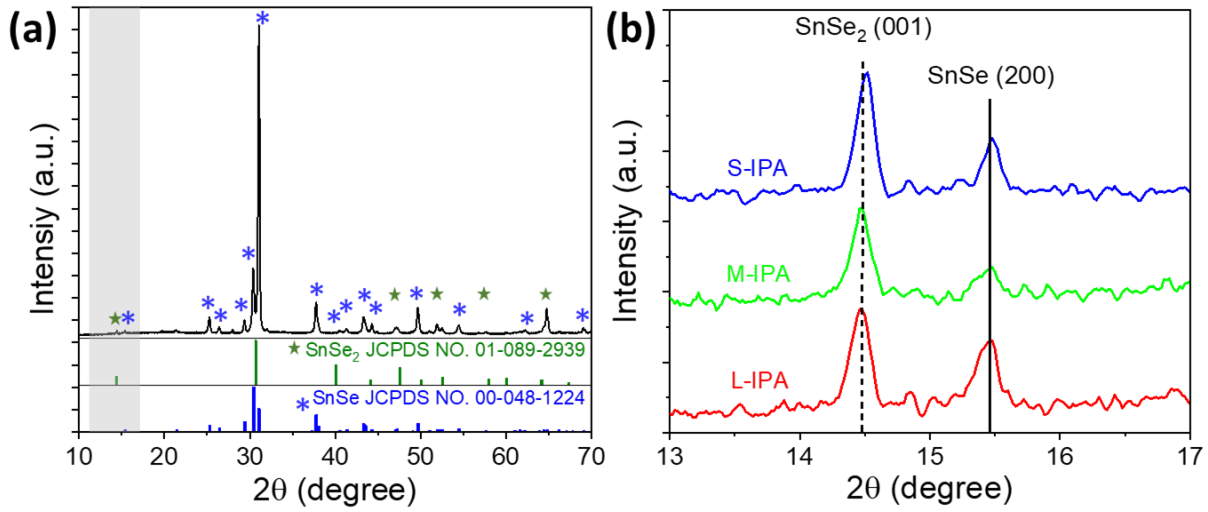

Fig. 22. (a) XRD pattern of large-size selected SnSe (L-SnSe) crystals, with SnSe and $SnSe_2$ formulations. (b) XRD patterns of the L-, M-, and S-IPA-SnSe flakes at around $2\theta = 15°$ are displayed for clarity.

To optimize the SnSe nanoflakes loading on the GC substrate for achieving the highest PEC activity, spray coating was used instead of m-LB method as the former method is much more convenient to tune the catalyst loading. **Fig. 23** shows the mass loading-dependent PEC HER performance of L-IPA-SnSe. 0.3 mg cm^{-2} was identified as the optimal loading of the SnSe flakes on GC. This loading was used for the preparation of other sized SnSe catalysts as well.

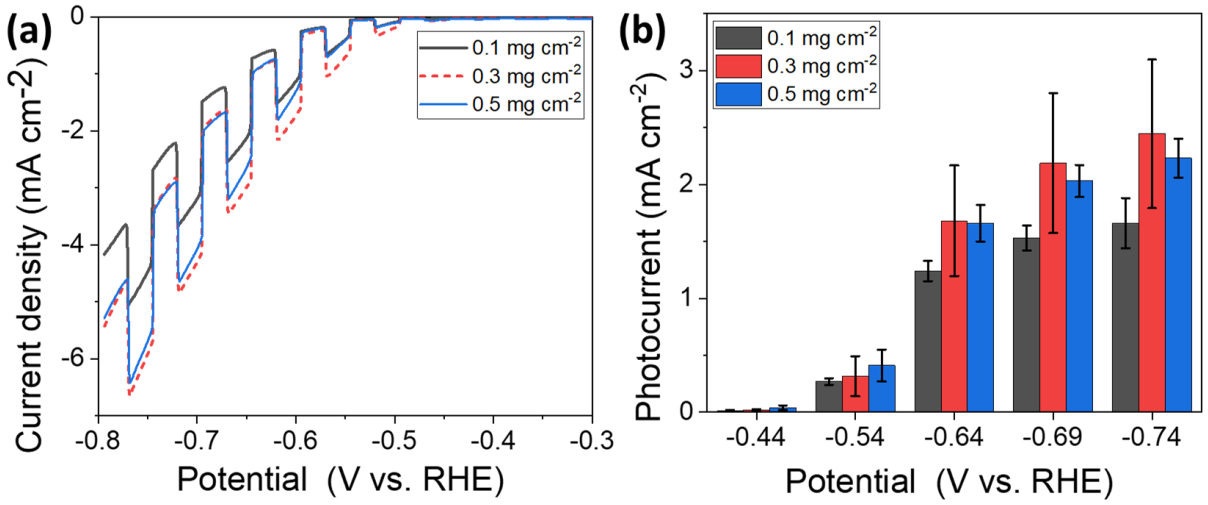

Fig. 23. (a) Linear sweep photovoltammograms for L-IPA-SnSe electrodes as the function of loading. Sweep rate was 2.5 mV s^{-1}. the photovoltammograms were measured in Ar saturated 0.5 M H_2SO_4 solution. (b) Bar diagram of photocurrent density plotted at 5 different potentials for three different loadings. The average values and error bars were obtained from parallel measurements on three different electrodes [60].

The effect of flake edge density on the PEC HER performance of SnSe was studied and the results were shown in **Fig. 24a**. No significant difference in photocurrent was found among samples with different edge densities (**Fig. 24b**). L-, M- and S-IPA-SnSe achieved the maximum photocurrent densities of ca. 2.3 mA cm^{-2} at −0.74 V vs. RHE, indicating that the flake edge density has no significant effect on PEC HER activity of SnSe flakes, which might be explained by that all the SnSe flakes are bulk materials, and they have identical properties. Besides, they showed higher photocurrent than that of IPA-SnSe (2.3 mA cm^{-2} vs. 1.18 mA cm^{-2}). These findings illustrate that the spray-coating and sieving-based methods collaborate to achieve higher PEC HER performance of SnSe nanoflakes.

IPCE spectra were conducted to measure the power conversion efficiency of SnSe samples (**Fig. 24c**). The electrodes showed the maximum IPCE value at 900 nm because of the narrow bandgap of SnSe (1.1 eV) [219]. In addition, two peaked values were found at 900 nm and 500 nm, indicating the compositions of SnSe and $SnSe_2$ in flakes, respectively. The IPCE spectra of L-, M- and S-IPA-SnSe electrodes showed same absorption edge and similar absorption region, implying analogous compositions. The presence of $SnSe_2$ phase (observed by Raman spectroscopy (**Fig. 17c**), XRD (**Fig. 22b**), and IPCE) in the flakes can form heterostructure with SnSe, and thus leads to more efficient charge carrier separation and interfacial charge transfer compared to pure SnSe, as reported [213].

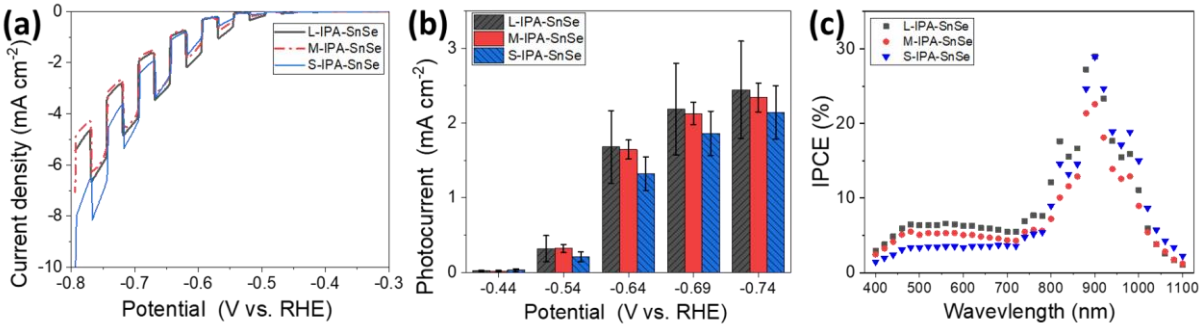

Fig. 24. (a) Linear sweep photovoltammograms of SnSe electrodes made from SnSe flakes (obtained by exfoliating (L, M, S)-SnSe crystals in IPA) with 2.5 mV s^{-1} sweep rate, in Ar saturated 0.5 M H_2SO_4 solution. (b) Bar diagrams of photocurrent extracted from linear sweep photovoltammetry curves of the electrodes shown in (a) at five different potentials. The averaged value and error bars were obtained from three replicate electrodes in each case. (c) IPCE of L-, M-, S-IPA-SnSe electrodes. The data were acquired at a fixed potential of −0.54 V vs. RHE [60].

Photostability is one of the most important criteria for an electrode to achieve good PEC performance. Thus, chronoamperometry curve (**Fig. 25a**) was recorded for L-IPA-SnSe

electrode at −0.54 V vs. RHE, under chopped 1 sun illumination (on/off, every 30 s). The electrode retained 52% of its initial activity after 60 min of reaction, demonstrating relatively good photostability. Moreover, to determine the stability of SnSe flakes in pure IPA solvent, their PEC HER activity was investigated as a function of the ageing time of their dispersions. To achieve this goal, the freshly prepared L-IPA-SnSe suspension was split into 5 portions. These suspensions were purged with Ar, sealed into the vial, and then kept under dark, room temperature conditions. Weekly, one of these portions was spray-coated on GC substrates with a mass loading of 0.3 mg cm^{-2}, and their PEC HER activity was tested (**Fig. 25b**). The electrodes prepared from fresh portions were used as a reference. The photocurrent density gradually decreased as the ageing time (**Fig. 25c**), denoting that SnSe flake was not stable in the IPA solvent under the employed condition, which might be caused by the restacking of flakes [62]. This possibility needs further study. Therefore, the results presented in SnSe work were conducted on freshly prepared SnSe flakes suspensions.

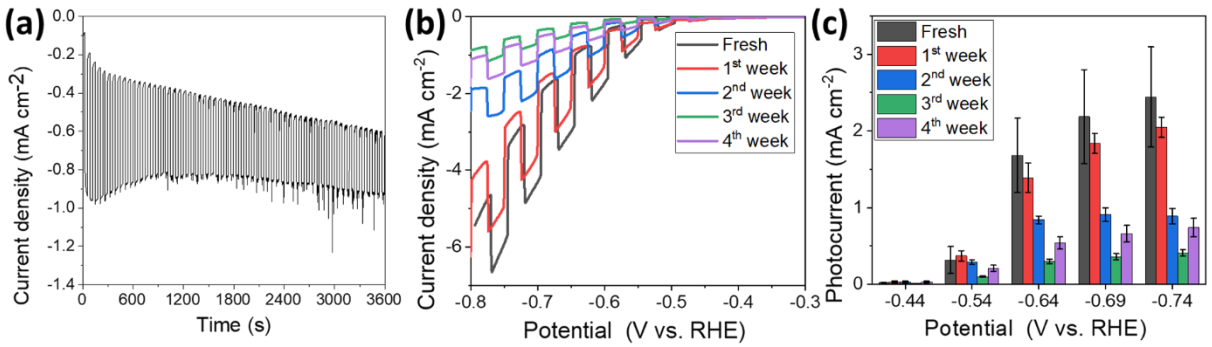

Fig. 25. (a) Transient photocurrent density profile of L-IPA-SnSe electrode. The data were collected at a potential of −0.54 V vs. RHE. (b) Linear sweep photovoltammograms of L-IPA-SnSe electrodes as the function of time (in weeks). The photovoltammetry curves with a sweep rate of 2.5 mV s^{-1}, were measured in Ar saturated 0.5 M H_2SO_4 solution under chopped 1 sun illumination. (c) Bar diagram of photocurrent density plotted versus the potential for five different aged samples. The average values and error bars were obtained from parallel measurements on three different electrodes [60].

5.1.3. The effect of Pt co-catalyst on the PEC HER performance of exfoliated SnSe

To improve the PEC HER activity of SnSe, Pt co-catalyst was decorated on the SnSe electrode by using the photodeposition method. Here, the S-IPA-SnSe specimen was used as bare SnSe reference because of its highest overall yield (**Table 3**). **Fig. 26a-c** exhibited the photocurrents of Pt/SnSe electrodes prepared with different Pt photodeposition recipe parameters (illumination time, illumination intensity, H_2PtCl_6 concentration), recorded at five potentials. The optimal

recipe parameters were 60 s illumination time, 44 mW cm^{-2} illumination intensity, and 5 mM H_2PtCl_6.

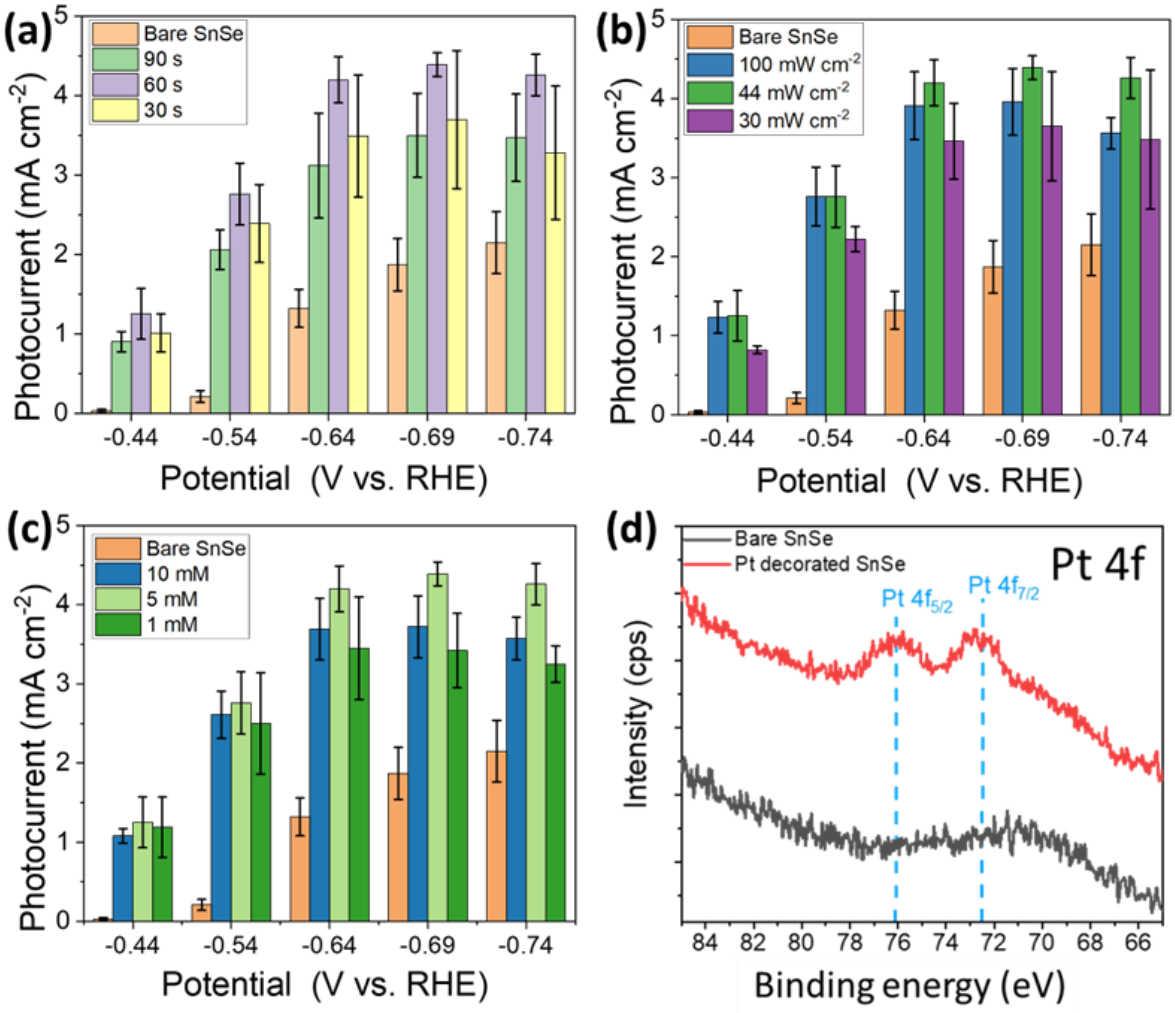

Fig. 26. (a-c) Bar diagrams of photocurrents plotted versus potential for bare and Pt deposited SnSe electrodes. Recipes were applied by using (a) different illumination time, (b) different illumination intensity, and (c) different concentration of H_2PtCl_6. (d) High-resolution Pt 4f XPS data of bare and Pt deposited SnSe electrodes [60].

XPS was used to examine the surface compositions of bare and Pt deposited SnSe electrodes. The results were shown in **Fig. 26d**, two peaks observed at binding energies of 76.1 eV and 72.6 eV were assigned to Pt $4f_{5/2}$ and $4f_{7/2}$, respectively. These results indicated the successful decoration of Pt on the surface of SnSe electrode.

Linear sweep photovoltammetry curves were recorded to compare the PEC HER activity of bare and Pt decorated SnSe electrodes (**Fig. 27a**). After Pt decoration, the electrodes showed several characteristics: i) significant higher photocurrents were obtained; ii) the dark currents

were higher and developed earlier; iii) the onset potential shifted to a less negative direction. The photocurrent of Pt/SnSe electrode at 0 V vs. RHE is lower compared to other catalysts [29,220]. This problem might be caused by the flakes structural domains (i.e., in plane defects, edges, and thickness of flakes) produced by the exfoliation process, which can strongly affect the PEC performance of TMDCs [53]. Recently, the PEC HER activity of SnSe thin films, prepared by thermal vacuum method, has been studied with varying selenization time, aiming to repair defects and to enhance its PEC activity. Such defects passivation treatment improved the photocurrent, and shifted the onset potential to a more positive value [62]. **Fig. 27b** presented that SnSe photoelectrodes decorated with Pt co-catalyst could achieve twice higher photocurrent than bare SnSe (i.e., 4.39 mA cm^{-2}).

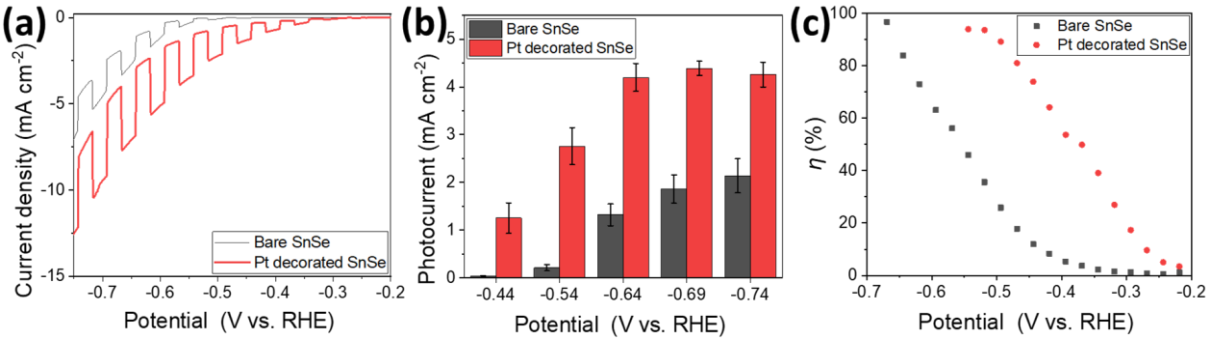

Fig. 27. (a) Linear sweep photovoltammograms of bare and Pt decorated SnSe electrodes. The photovoltammograms with a sweep rate was 2.5 mV s^{-1}, were measured in Ar saturated 0.5 M H_2SO_4 solution under chopped 1 sun illumination. (b) Bar diagram of photocurrent density plotted versus potential, and (c) The determined charge transfer efficiency as a function of applied potential for bare and Pt decorated SnSe photoelectrodes [60].

To study the effect of Pt co-catalyst on charge carrier dynamics in the prepared SnSe photocathodes, IMPS measurements were carried out at different potentials [221,222]. **Fig. 28a** and **b** exhibited the IMPS spectra of bare and Pt decorated SnSe electrodes, respectively, measured in the potential window of –0.24 V to −0.67 V vs. RHE. Two semicircles were observed in the 2nd and 3rd quadrant, which are the characteristic of p-type semiconductor behavior [223]. The almost perfect circles presented at less negative potentials, indicating that the recorded steady-state photocurrent approached zero. Hence, the surface recombination dominated the PEC behavior of the system. No upper semicircles were found below −0.67 V vs. RHE and −0.57 V vs. RHE for bare SnSe and Pt decorated SnSe electrodes, respectively. Kinetic parameters, charge carrier transfer (k_{tr}) and surface recombination (k_{sr}) could be derived from the IMPS spectra, and were plotted as a function of applied potential (**Fig. 28c** and **d**). Compared

to bare SnSe, Pt decorated SnSe presented higher k_{tr} at same potential until −0.5 V vs. RHE, and smaller k_{sr} below −0.3 V vs. RHE, as expected that co-catalyst enhances the charge transfer and suppresses the charge carrier recombination [224,225]. The relative transfer efficiency could be determined from the equation: $\eta_{tr} = k_{tr}/(k_{tr}+ k_{sr})$ [203]. Significant improvement in η_{tr} values was observed for Pt decorated SnSe (**Fig. 27c**), while the bare SnSe electrode could also achieve a similar η_{tr} (~90%) at more negative potentials.

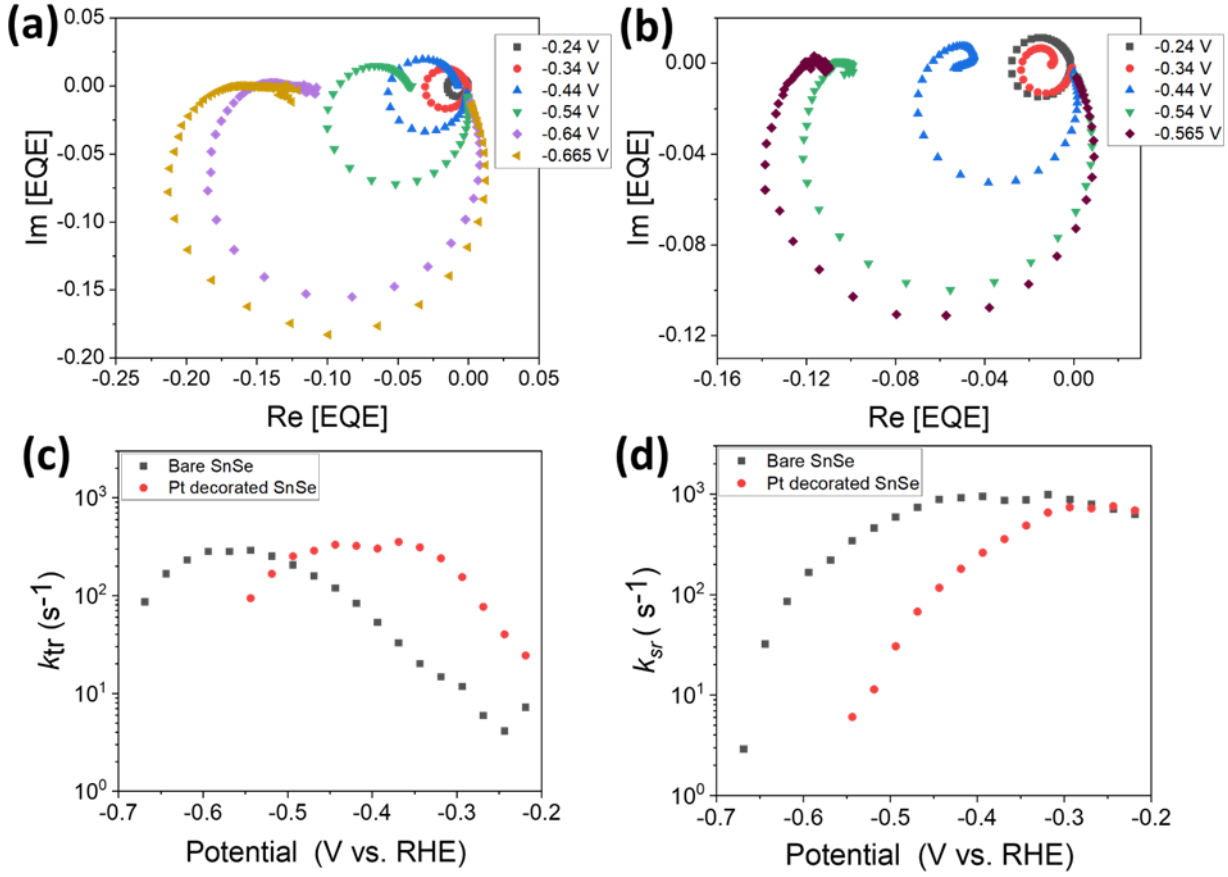

Fig. 28. IMPS data for (a) bare and (b) Pt decorated SnSe electrodes. Measured 25 mV potential step (only some potential is shown here). (c) Charge transfer and (d) recombination rate constants as the function of the applied potential determined from the IMPS data [60].

The Cole–Cole plots of bare and Pt-decorated SnSe electrodes were derived from IMPS data, as shown in **Fig. 29**. The peaks presented at around 2.5 kHz and 2.2 kHz for bare SnSe, and Pt decorated SnSe electrodes, respectively, which can be explained by the charge transport in the semiconductor layer [204]. The Cole–Cole plots showed higher imaginary frequency dependent EQE for Pt decorated SnSe.

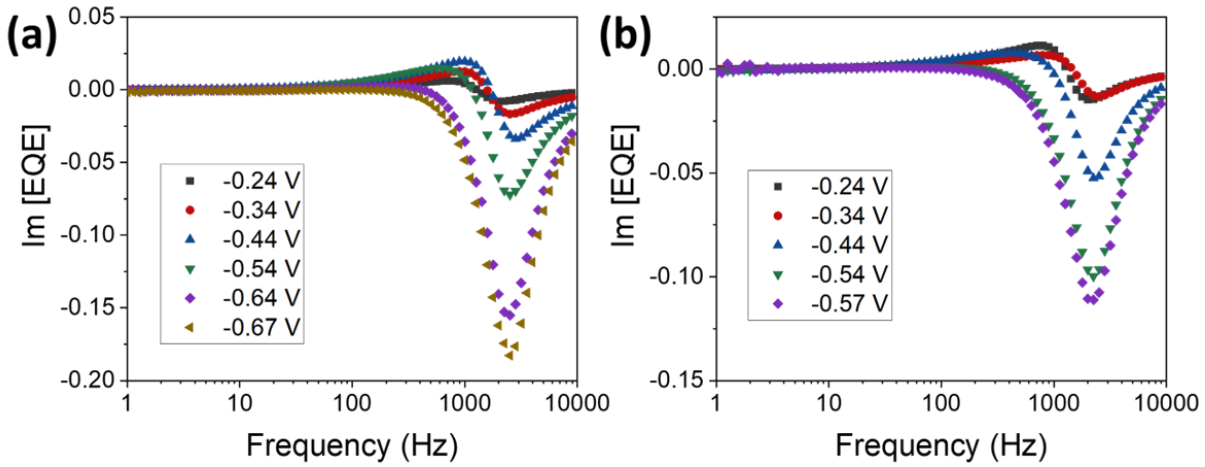

Fig. 29. Cole–Cole plots for (a) bare and (b) Pt decorated SnSe electrodes as the function of the applied potential determined from the IMPS data [60].

The processes occurring at the co-catalyst decorated and bare SnSe were summarized in **Fig. 30**. For bare SnSe (**Fig. 30a**), the CB electrons could (1) migrate to the surface states and recombine with the VB holes, or (2) directly reduce water. The former means that they do not participate in the water reduction process. By functionalizing the SnSe electrode with Pt co-catalyst (**Fig. 30b**), the surface states are passivated, thereby hindering charge carrier recombination (1). Meanwhile, the electrons could also transfer to Pt, then directly reduce water via Pt (3) [224]. This dual role of Pt led to the enhancement of the PEC activity of SnSe in HER application.

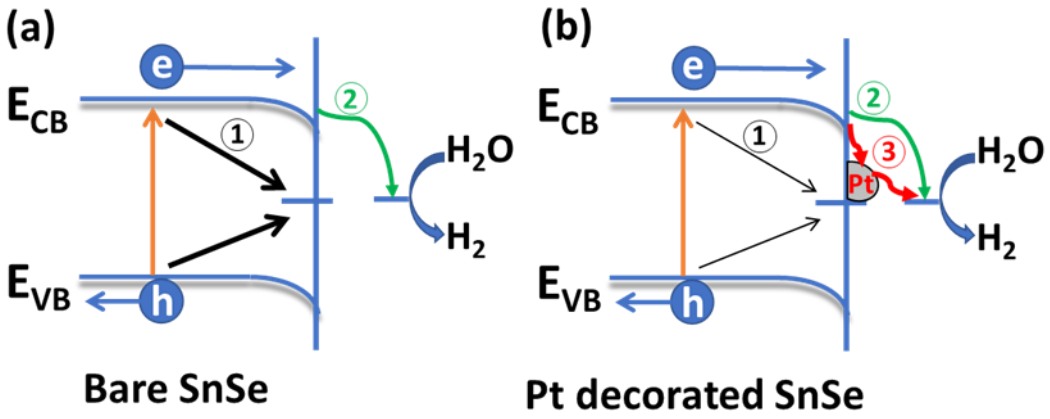

Fig. 30. Simplified models of the elementary processes in (a) bare SnSe, and (b) Pt decorated SnSe electrodes. Upon illumination, photogenerated carriers move towards the semiconductor-electrolyte interface, (1) surface state-mediated recombination of electron-hole pairs, (2) electron transfer directly from the conduction band to the electrolyte, (3) electron transfer to the electrolyte via Pt [60].

5.1.4. The PEC HER performance of SnSe synthesized by hydrothermal method

SnSe was also synthesized via the hydrothermal method [95], and spray-coated on GC substrate, and ultimately used as photocathode for HER. **Fig. 31a** and **b** presented the SEM images of SnSe film, showing the nanosheet morphology of SnSe, and the film was uniform on the GC.

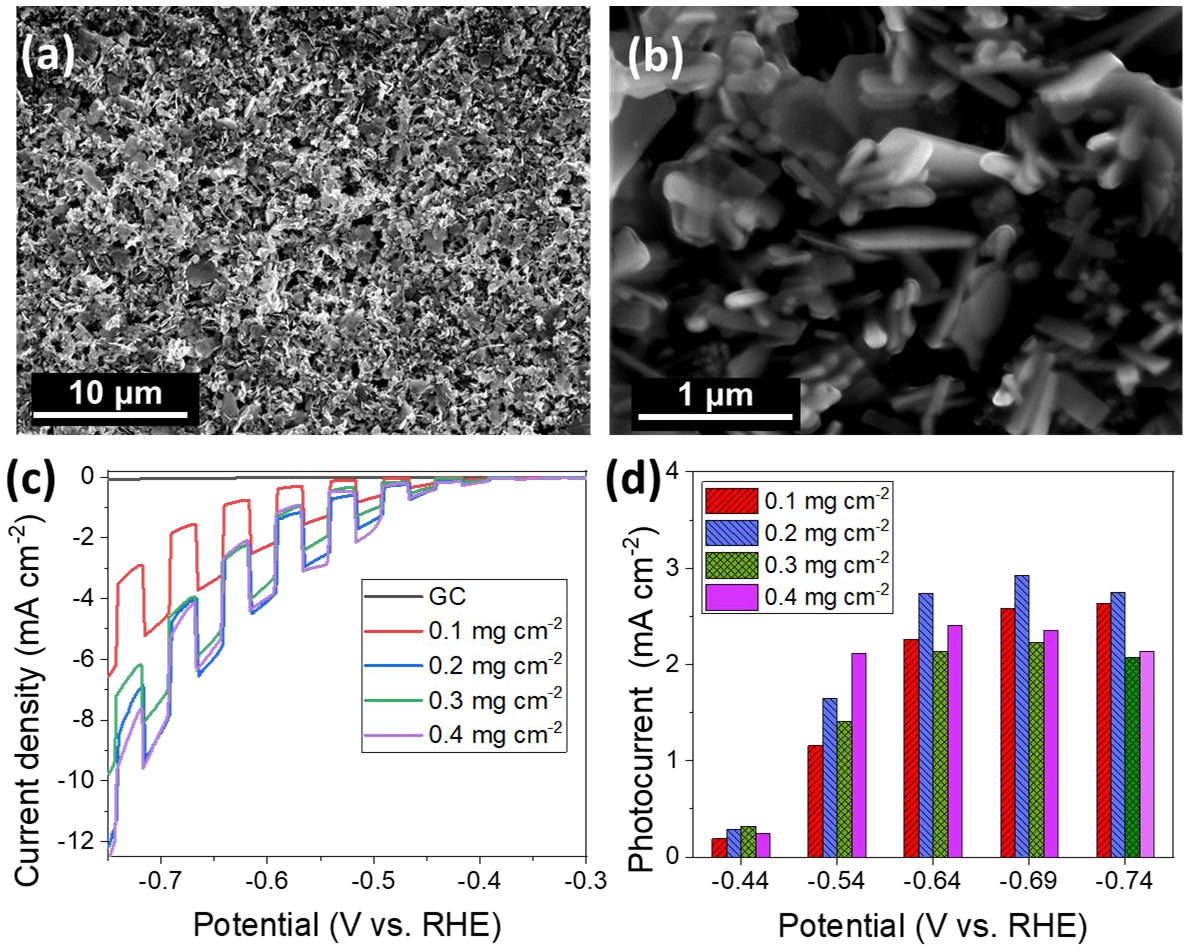

Fig. 31. (a) and (b) SEM images with different resolutions of SnSe film on GC substrate. (c) Linear sweep photovoltammograms of SnSe photocathodes with different loadings, measured in Ar saturated 0.5 M H_2SO_4 solution. Sweep rate is 2.5 mV s^{-1}. (d) Bars of photocurrents as a function of potentials at four different loadings.

To study the loading-dependent PEC activity, SnSe/GC electrodes with different loadings were prepared and tested in Ar saturated 0.5 M H_2SO_4 solution (**Fig. 31c**). All electrodes showed higher dark current than GC substrate. Compared to the higher loadings, 0.1 mg cm^{-2} loaded electrode exhibited lower dark current, which might be explained by the lower edge density. Furthermore, the photocurrents at five different potentials were calculated from **Fig. 31c**, and the results were shown in **Fig. 31d**. 0.2 mg cm^{-2} is identified as the optimal loading, achieving a maximum photocurrent of 3 mA cm^{-2} at −0.69 V vs. RHE, which is in the same

order of magnitude as liquid phase exfoliated SnSe flakes (2.3 mA cm^{-2}), suggesting no significant improvement in HER activity was achieved by the hydrothermal method under the employed condition.

5.1.5. The PEC HER behavior of ZnSe/SnSe heterostructure

The fabrication of heterostructure is one of the most used techniques to improve the PEC performance of SCs, owing to the efficient charge transfer [31,77]. To enhance the PEC HER activity of SnSe flakes, and given the suitable CB alignment of ZnSe and SnSe for HER (**Fig. 9**), ZnSe/SnSe heterostructure was constructed by depositing ZnSe flakes on SnSe surface. To prepare ZnSe flakes, ZnSe crystals were exfoliated in EtOH and IPA solvents, respectively. Centrifugation was then employed for flake-size selection, and the obtained flakes were deposited on a GC substrate via the m-LB method and ultimately used as photoelectrodes. Their PEC activity was tested in Ar saturated 0.1 M Na_2SO_4 solution (**Fig. 32**), and the flakes exfoliated from EtOH showed higher photocurrent than the IPA case.

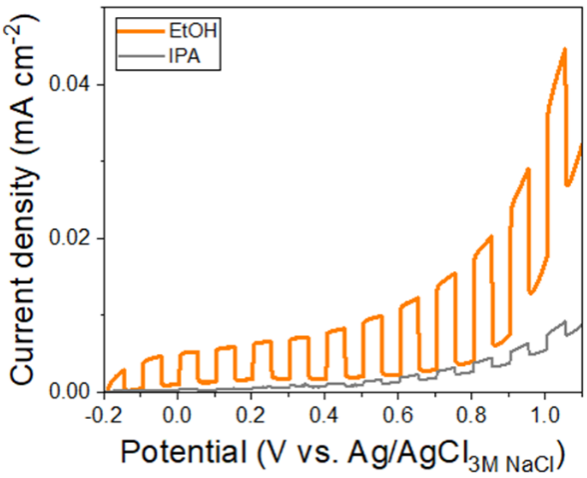

Fig. 32. Linear sweep photovoltammograms of ZnSe electrodes made from ZnSe flakes (exfoliated from EtOH and IPA solvents, respectively). The photovoltammograms with a sweep rate of 2.5 mV s^{-1}, were measured in Ar saturated 0.1 M Na_2SO_4 solution under chopped 1 sun illumination.

The heterostructure of ZnSe/SnSe was fabricated by depositing n-type ZnSe flakes exfoliated from EtOH on p-type SnSe by using m-LB method, and their PEC HER performance was evaluated using linear sweep photovoltammetry profiles measured in Ar saturated 0.5 M H_2SO_4 solution (**Fig. 33a**). It showed lower dark current compared to bare SnSe, which might result from the higher separation efficiency of charge carriers and/or the defect passivation effect

of ZnSe on SnSe flakes. No significant difference in photocurrent was observed, which was probably because the ZnSe film detached from the electrode during the measurement. To improve the adhesion of ZnSe film, the heterostructure electrodes were annealed at 120 °C in vacuum for 30 min, while there was still no significant improvement in PEC activity compared to the sample without annealing (**Fig. 33b**).

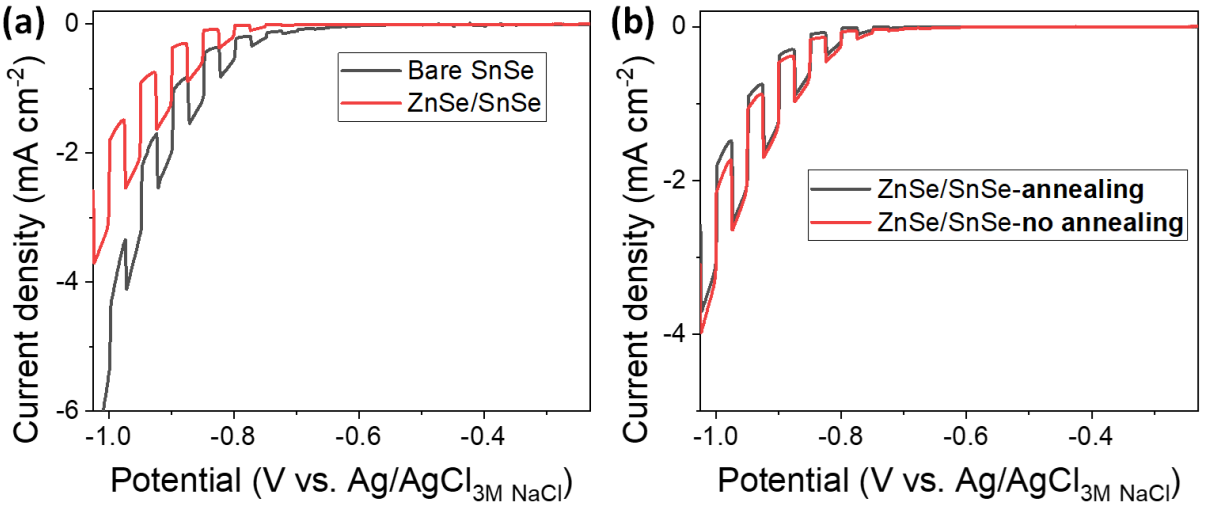

Fig. 33. The PEC HER performance of ZnSe/SnSe electrodes. Linear sweep photovoltammograms of (a) bare and ZnSe decorated SnSe electrodes, and (b) ZnSe/SnSe electrodes with and without annealing. The photovoltammograms with a scan rate of 2.5 mV s^{-1} were measured in Ar saturated 0.5 M H_2SO_4 solution.

5.2. GaTe flakes activity for photoelectrochemical hydrogen evolution

5.2.1. The PEC HER activity of GaTe microelectrodes

The PEC activity of the GaTe nanoflakes was examined by our designed PEC microscopy setup [23,56,200], as illustrated in **Fig. 14** (in the **Experimental** part). To study their thickness effect on PEC performance, twelve GaTe samples with thicknesses varying from 108 ± 7 nm to 885 ± 44 nm were fabricated. Given that the thickness of GaTe monolayer is ~0.75 nm [226], thus all these flakes are regarded as bulk. **Fig. 34a** showed a representative example of GaTe nanoflakes. Due to the different refractive indexes of GaTe and SiO_2/Si substrate [131], the area deposited by GaTe nanoflakes can be differentiated optically (**Fig. 34a**). Additionally, the different colors of GaTe nanoflakes on the optical image indicated the different flake thicknesses. **Fig. 34b** displayed the AFM image corresponding to the region outlined by the dashed red rectangle in **Fig. 34a**. The height profile, highlighted by the dashed blue line in **Fig. 34b**, is presented in **Fig. 34c**, revealing a flake thickness of 140 ± 9 nm.

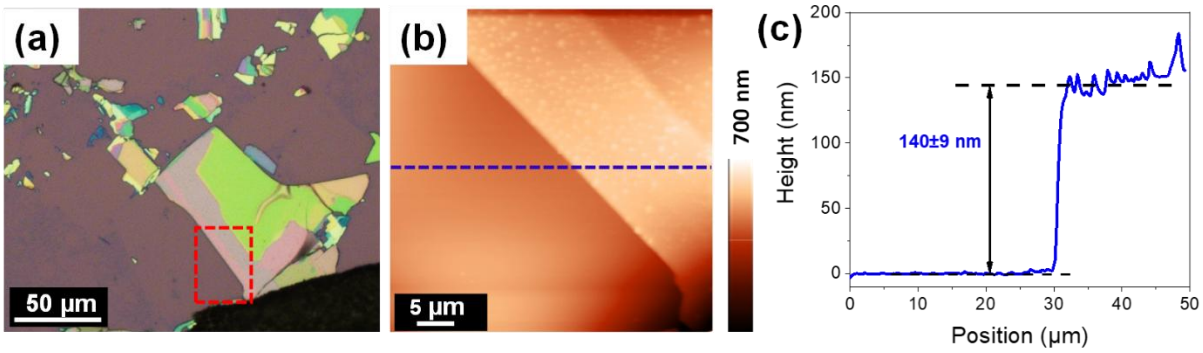

Fig. 34. Morphological and structural characterization of GaTe nanoflakes. (a) Optical image of GaTe nanoflakes on SiO_2/Si substrate. (b) AFM image of GaTe nanoflake indicated by red rectangle in (a), and (c) The height profile from the region highlighted by the dashed blue line in (b). Adapted from ref.[200].

A KP instrument was used to measure the band structure of mechanically exfoliated GaTe sample (**Fig. 35**). The bandgap (1.7 eV), the Fermi level (−4.31 eV), and VB (−4.97 eV) were determined by surface photovoltage spectroscopy (SPS), contact potential difference (CPD), and ambient pressure photoemission spectroscopy (APS), respectively, the details were shown in **Table 7**. Then the CB was obtained (−3.27 eV) from the measured VB position and bandgap. The Fermi level is much closer to VB than CB, demonstrating the p-type nature of GaTe. Furthermore, the CB of GaTe is higher than the standard potential of the H^+/H_2 (−3.27

eV vs. −4.44 eV), suggesting that GaTe is thermodynamically suitable to carry out H^+ reduction process, which is consistent with previous studies [24,137–139].

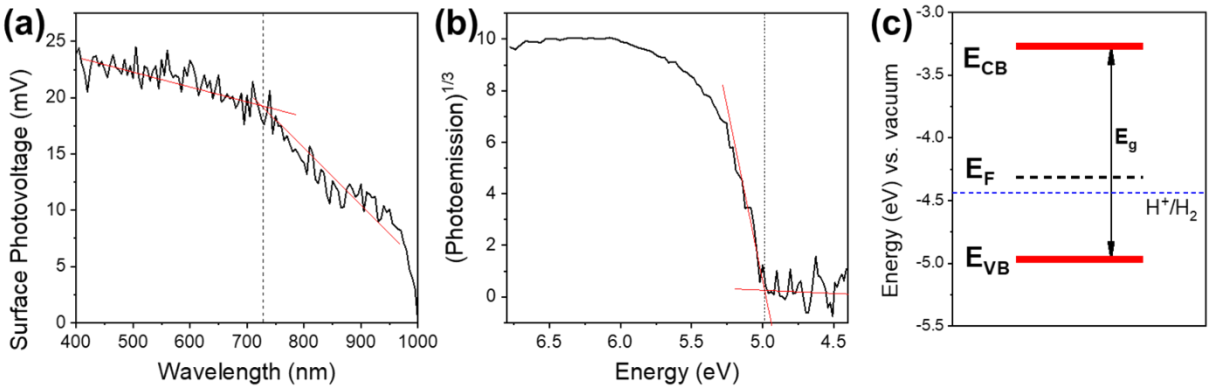

Fig. 35. (a) SPS, (b) APS, and (c) band diagram of mechanically exfoliated GaTe sample [200].

Table 7. The summary of band edge positions, Fermi level, and bandgap values for GaTe sample from the Kelvin probe measurements [200].

Specimen	E_{VB} (eV)	E_F (eV)	E_{CB} (eV)	Eg (eV)
GaTe	−4.97 ± 0.06	−4.31 ± 0.05	−3.27± 0.03	1.7± 0.02

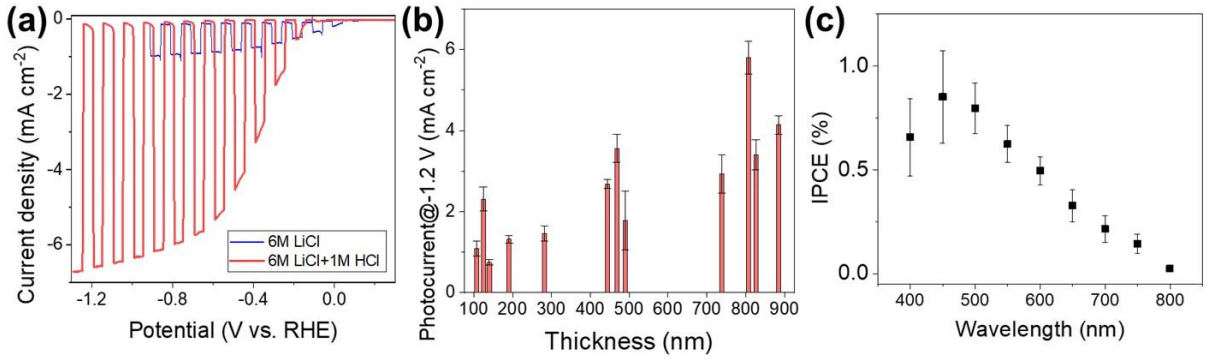

Fig. 36. The PEC activity, thickness-dependent PEC activity, and IPCE data of GaTe microelectrodes. (a) Linear sweep photovoltammograms of GaTe nanoflakes using 6 M LiCl and 1 M HCl/6 M LiCl droplets (sweep rate was 2.5 mV s^{-1}), under chopped illumination. The thickness of GaTe nanoflake herein was 808 ± 50 nm. (b) The photocurrent of GaTe nanoflakes with different thicknesses (100-900 nm) at −1.2 V vs. RHE. (c) IPCE of GaTe nanoflakes with 318 ± 6 nm thickness at −0.59 V vs. RHE. The average values and error bars were obtained from three individual droplets deposited on each nanoflake in three different spots. The electrolyte was 1 M HCl/6 M LiCl in (b-c) [200].

Linear sweep photovoltammetry curves of GaTe were recorded to evaluate its PEC activity (**Fig. 36a**), and it exhibited p-type photoactivity, in agreement with KP results (**Fig. 35**). GaTe nanoflakes showed higher PEC activity in 1 M HCl/6 M LiCl compared to 6 M LiCl droplets. To study the PEC activity as a function of flake thickness, twelve GaTe flakes with different thicknesses (within 100-900 nm) were selected and tested. The prepared flakes and their main properties are summarized in **Table 8.** Their photocurrent at −1.2 V vs. RHE was presented in **Fig. 36b**, achieving the highest photocurrent around 6 mA cm^{-2} with 808±50 nm flake thickness. Also, the photocurrent was enhanced with thicker flakes. The same phenomenon was reported for bulk p-type WSe_2 (20-120 nm thickness) [53,56]. The adsorbed water on the flake and the defects caused by mechanical exfoliation could affect the PEC activity, which can lead to the variation in photoelectrochemical properties between sample to sample [47]. In addition, the large variation in kinetics was found on the same flake surface [45]. Therefore, flakes with similar thickness may achieve quite different photocurrent.

Table 8. Summary of the properties of the mechanically exfoliated GaTe flakes used in PEC tests [200].

GaTe flakes	Thickness (nm)	Lateral size (μm)	Area (μm^2)	Photocurrent density at −1.2 V vs. RHE (mA cm^{-2})
1	108	157.6	9430	1.09±0.18
2	125	129.1	6789	2.31±0.30
3	140	123.3	6256	0.75±0.06
4	191	101.2	4075	1.32±0.09
5	282	224.4	14231	1.46±0.19
6	444	107.3	2073.5	2.68±0.11
7	468	691.8	204476	3.56±0.34
8	490	122.8	5023	1.78±0.72
9	739	322.6	20701.4	2.93±0.47
10	808	691.8	2045	5.8±0.41
11	826	371.4	62648	3.40±0.37
12	885	253.7	26481	4.14±0.23

IPCE was carried out to determine the wavelength-dependent power conversion efficiency of the GaTe microelectrodes. A representative example of IPCE spectra was shown in **Fig. 36c**. This flake with a thickness of 318 ± 6 nm, presented an absorption edge of 750 nm, corresponding to a 1.65 eV bandgap, which agrees with KP result and reported studies [136,227]. All these results illustrate that, the GaTe microelectrode can be applied for PEC HER application.

5.2.2. The PEC HER activity of GaTe macroelectrodes

The GaTe crystals were exfoliated in pure IPA, and the obtained flake suspension was separated by centrifugation. Subsequently, the desired flakes suspension was spray-coated on the GC substrate, and ultimately used as photocathodes for PEC HER application, the details can be found in the **Experimental**.

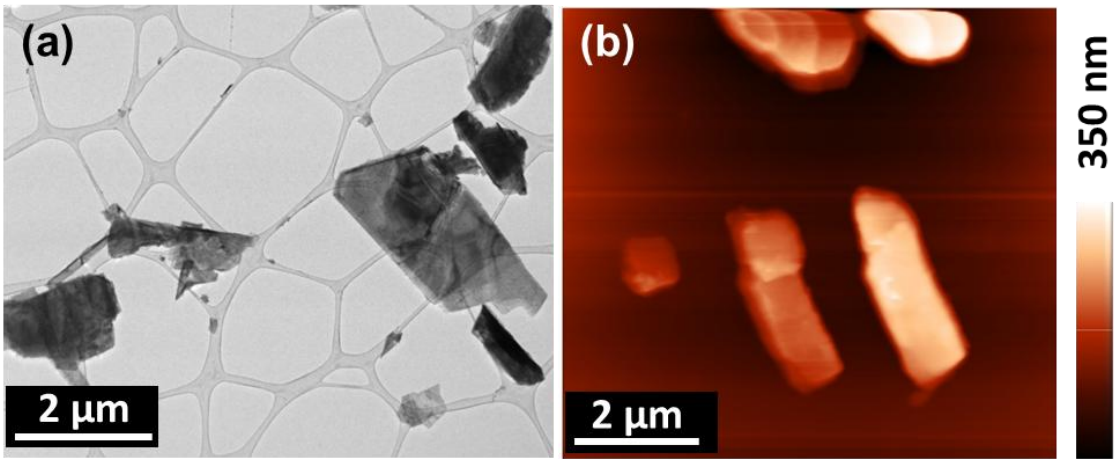

Fig. 37. (a) TEM and (b) AFM images of GaTe nanoflakes exfoliated in pure IPA by the LPE method. Adapted from ref.[200].

TEM and AFM were used to characterize the morphology of LPE prepared GaTe flakes, and all nanoflakes presented angular shape (**Fig. 37**). The size distributions of over 120 GaTe nanoflakes were analyzed, by using TEM images to determine the flake area and perimeter, and using AFM to measure the thickness. The histograms of flake size in **Fig. 38** showed a log-normal distribution, agreeing with prior findings. This distribution suggests a random multiplicative process, such as ball milling and cavitation, illustrating that the exfoliation follows a linear fragmentation model [60,205,206]. The most probability of the flake perimeter, area, and thickness were listed in **Table 9**, which were 1.37 µm, 0.02 μm^2, and 129 nm, respectively. Furthermore, the edge density was calculated by dividing the perimeter by the area [22,60], and GaTe nanoflakes had an edge density of 69 μm^{-1}. Studies have shown that the edge

density can affect the PEC activity of solution-processed MoS_2 flakes, and the higher edge density generally results in lower PEC activity [22], as the flake edges are considered as the recombination centers for photogenerated charge carriers [25].

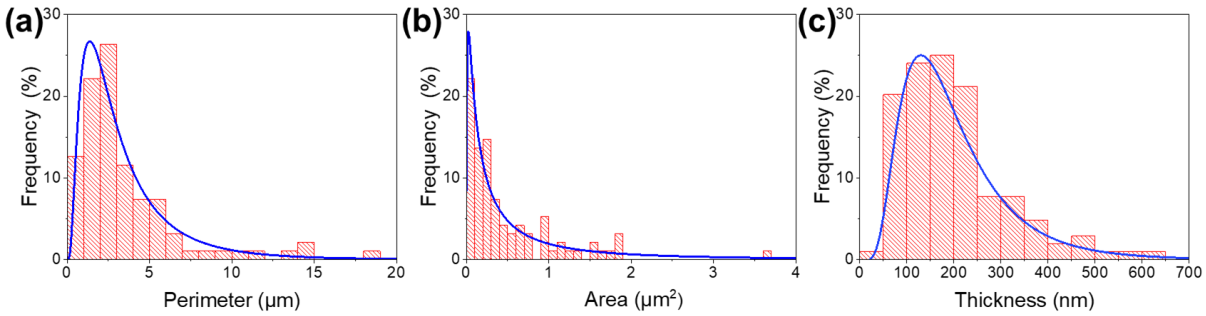

Fig. 38. Statistical analysis on (a) perimeter, (b) area, and (c) thickness of the LPE prepared GaTe nanoflakes [200].

Table 9. The most probability of perimeter, area, thickness, and the calculated edge density values (perimeter/area) of GaTe nanoflakes collected from dispersions [200].

Specimen	Perimeter (μm)	Area (μm^2)	Thickness (nm)	Edge density (μm^{-1})
GaTe	1.37	0.02	129	69

Raman spectrum was measured to detect the vibrational modes of the GaTe flakes**. Fig. 39a** presents the Raman spectrum of GaTe macroelectrode, obtained using a 532 nm laser excitation. The bands observed at 67, 114, 207 and 269 cm^{-1} are assigned to the A_g vibration mode, and 162 cm^{-1} corresponds to the B_g vibration mode. These results agree with reported Raman spectra of monoclinic phase of GaTe [143,228,229]. In addition, the band at 128 cm^{-1} is might be caused by the oxidation or degradation of GaTe upon exposure to an ambient air environment, as suggested by other reports [132]. XRD was used to characterize the crystallinity of the nanostructured GaTe film (**Fig. 39b**). The diffraction peaks at 2θ of 12 and 24 degree are corresponding to the (-210) and (-420) faces of monoclinic phase of GaTe, respectively, which are in agreement with Raman spectrum results.

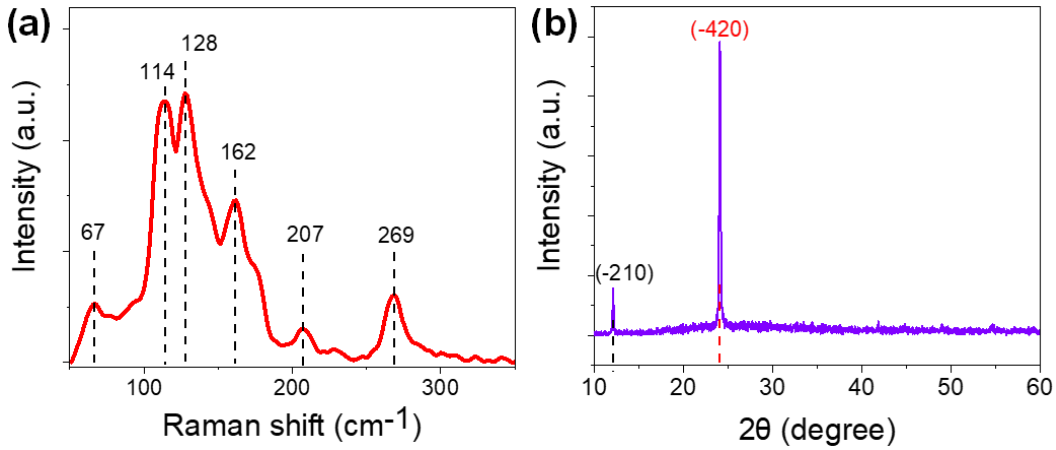

Fig. 39. (a) Raman spectrum and (b) XRD pattern of GaTe macroelectrode. Adapted from ref.[200].

The spray coating method is a versatile technique for depositing thin films with tunable loading on various substrates [230,231]. Hence, it was used to prepare GaTe macroelectrodes by spray-coating GaTe nanoflakes on GC substrate. To study the loading effect on PEC activity, GaTe/GC macroelectrodes with different mass loadings (0.1, 0.3, and 0.5 mg cm^{-2}) were fabricated, and tested in Ar saturated 0.5 M H_2SO_4 electrolyte. **Fig. 40** showed the SEM images of GaTe/GC photoelectrodes: 0.1 mg cm^{-2} is insufficient for complete coverage of the GC substrate, while loadings of 0.3 mg cm^{-2} and 0.5 mg cm^{-2} suffice, indicating that higher loading enhances electrode coverage.

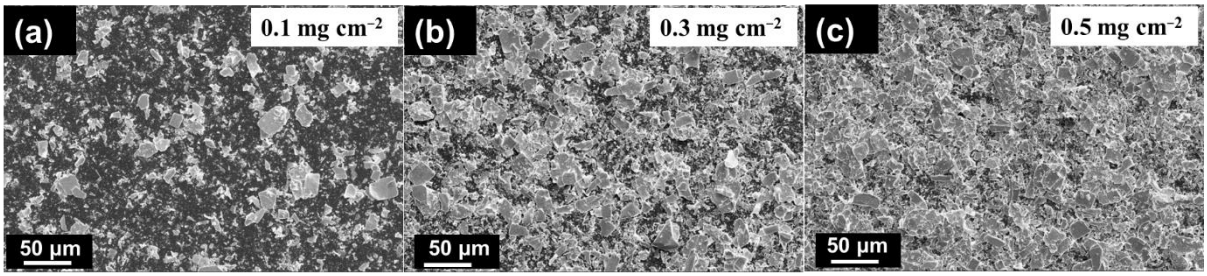

Fig. 40. Coverage of GaTe nanoflakes deposited by spray coating on GC substrates. SEM images of (a) 0.1 mg cm^{-2}, (b) 0.3 mg cm^{-2}, and (c) 0.5 mg cm^{-2} loading of GaTe nanoflakes [200].

Fig. 41a showed the PEC activity of the macroelectrodes with different loadings. The electrodes loaded with 0.1 mg cm^{-2} and 0.3 mg cm^{-2} display similar dark current with GC substrate, possibly attributed to the partial exposure of the conductive substrate to the electrolyte. In contrast, the 0.5 mg cm^{-2} loading showed the highest dark current due to the most edge defects compared to the lower mass loadings (0.1 and 0.3 mg cm^{-2}). **Fig. 41b** presented the photocurrents at several different potentials as the function of mass loading, indicating that 0.3

mg cm^{-2} is the optimal loading, achieving a maximum photocurrent of 0.57 ± 0.01 mA cm^{-2} at −0.74 V vs. RHE.

IPCE was measured to investigate the power conversion efficiency of the GaTe macroelectrodes at different wavelengths (**Fig. 41c**). The electrodes with 0.3 mg cm^{-2} were utilized for IPCE measurement. It showed a maximum IPCE value of ~8% at 400 nm, and an absorption edge of 795 nm, corresponding to a bandgap of 1.56 eV.

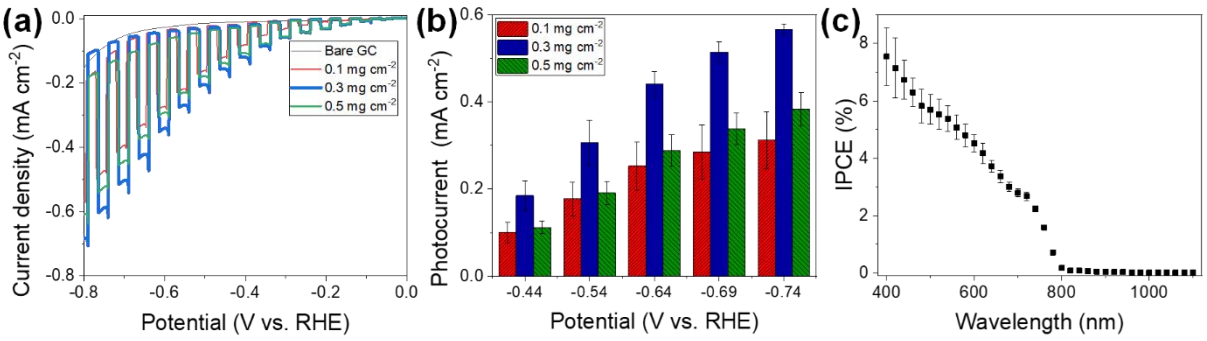

Fig. 41. (a) Linear sweep photovoltammograms of GaTe/GC electrodes as the function of loading. Photovoltammograms were measured in Ar saturated 0.5 M H_2SO_4 solution, scan rate was 2.5 mV s^{-1}. (b) Bar diagram of photocurrents plotted versus the potentials at three different loadings. (c) IPCE of GaTe/GC electrode at −0.59 V vs. RHE in 0.5 M H_2SO_4 solution. Adapted from ref.[200].

To investigate the illumination intensity dependency of PEC HER activity, five GaTe/GC photocathodes (prepared from the same batch) were tested under different illumination intensities (**Fig. 42a**). The PEC activity was enhanced as illumination power increased because more charge carriers were generated. Furthermore, the photocurrents at − 0.79 V vs. RHE were derived from linear sweep photovoltammetry curves (**Fig. 42a**), and presented in **Fig. 42b**. A linear relation between photocurrent density and illumination intensity was observed, and the GaTe electrode showed the highest photocurrent of 4 mA cm^{-2} at −0.79 V vs. RHE under 10 sun illumination.

To study the photostability of the GaTe/GC electrodes, the long-term (60 min) chronoamperometry profile was recorded under chopped illumination (on/off every 30 s) at −0.54 V vs. RHE (**Fig. 42c**). Continuous magnetic stirring was used in the cell through the whole measurement to remove the H_2 bubbles from the GaTe electrode surface. After 60 min reaction, the electrodes under 1 and 10 sun illumination remained 92% and 80% of their initial activity, respectively. The main product for GaTe photoelectrode in PEC HER test is H_2. A photoelectrolysis experiment (60 min) at −0.79 V vs. RHE using two GaTe photoelectrodes was

performed to collect the gas product. We found that the FE% is 93.2 ± 7 % for three different data points. SEM characterization showed that some GaTe flakes detached from the GC substrate after the 60 min photoelectrolysis (**Fig. 43**) measurement, which might be caused by the bubble formation during the HER process.

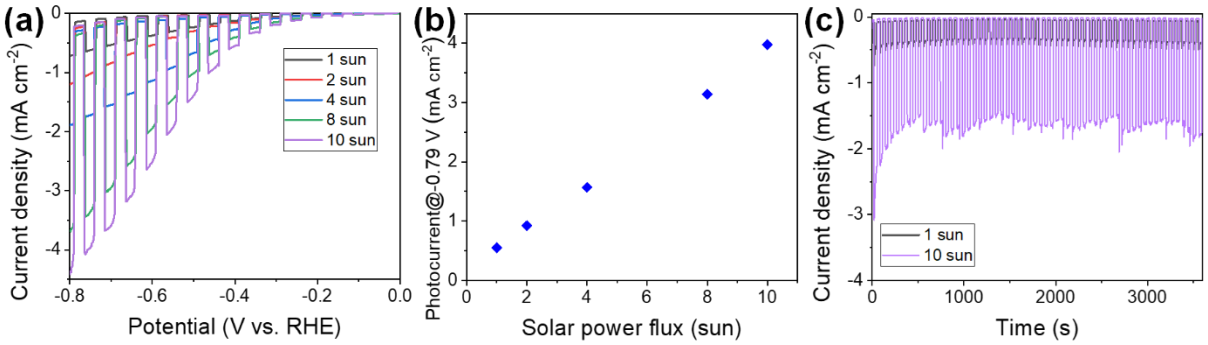

Fig. 42. (a) Linear sweep photovoltammograms of GaTe/GC macroelectrodes as the function of illumination intensity. Photovoltammograms were measured in Ar saturated 0.5 M H_2SO_4 solution, the scan rate was 2.5 mV s^{-1}. Five photocathodes from the same batch were studied here. (b) The photocurrent densities of GaTe/GC electrode at −0.79 V vs. RHE under different illumination intensities. (c) The long-term stability of GaTe/GC electrode at −0.54 V vs. RHE under 1 and 10 sun illumination. The mass loading was 0.3 mg cm^{-2} in (a-c) [200].

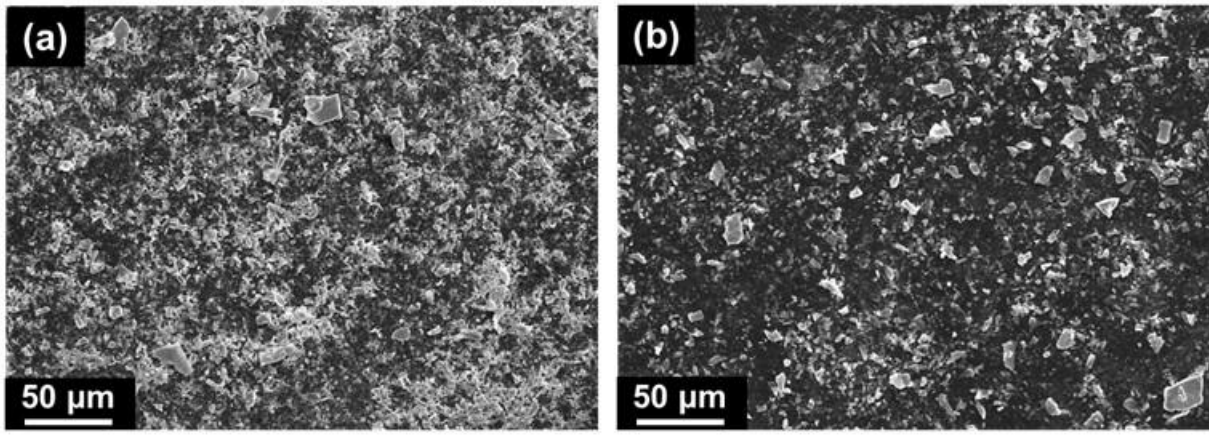

Fig. 43. SEM images of (a) before and (b) after the long-term chronoamperometry experiments of GaTe nanoflakes [200].

5.2.3. The comparison of PEC activity of GaTe micro- and macro-electrodes

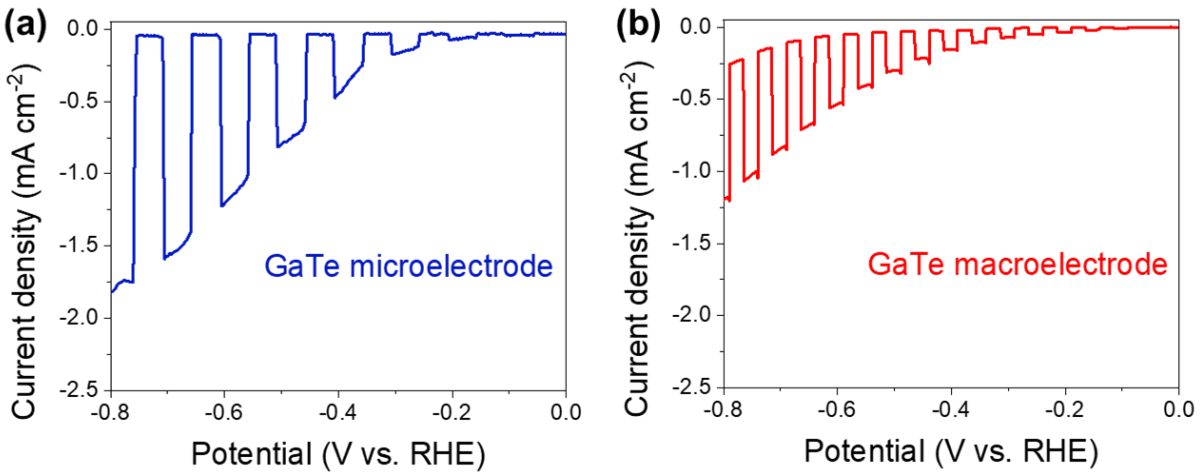

Fig. 44. Linear sweep photovoltammograms of GaTe (a) microelectrodes and (b) macroelectrodes under 200 mW cm^{-2} illumination intensity. The scan rate was 2.5 mV s^{-1} in (a) and (b).

The PEC HER performance of GaTe micro- and macro-electrodes under 200 mW cm^{-2} illumination intensity were shown in **Fig. 44**. The thickness of GaTe flake in **Fig. 44a** is 125 nm, and the one in **Fig. 44b** is 129 nm. The microelectrode achieved higher photocurrent and lower dark current than the macroelectrode, which can be explained by that, in the case of macroelectrode, more defects are produced after liquid phased exfoliation process. In contrast, in the case of microelectrode, we can measure the PEC activity at less defective positions (basal plane) [22,29,57]. As reported, the defects can be the recombination centers for photogenerated charge carriers, resulting in high dark current and low PEC activity. Besides, several studies illustrated that, the MoS_2 networks processed from solution (using LPE method) show relatively low carrier mobility (ca. 10 cm^2 V^{-1} s^{-1}), which is one order of magnitude lower than MoS_2 nanoflakes (over 100 cm^2 V^{-1} s^{-1}) prepared by the mechanical exfoliation method [232–234]. Similarly, the GaTe networks fabricated with solution-processed GaTe nanoflakes might have lower conductivity or carrier mobility compared to mechanically exfoliated GaTe microelectrodes in our case, which needs further investigation.

5.3. The PEC HER behavior of other semiconductors

Except SnSe and GaTe materials, many other layered SCs including GeS, ZnTe, As_2S_3 and Cu_2S (Cu_2Se, Cu_2Te), used for PEC HER application have been investigated in our study. In this section, different solvents for the LPE process, different substrates, and different flake synthesis methods have been explored, aiming to achieve good PEC performance. While all the photocathodes prepared from these materials showed negligible photocurrent (in the range of μA), and GeS was given as a representative example here.

The AR-GeS crystals were exfoliated in "green solvents", such as EtOH, IPA, and EtOH/H_2O. After the flake size-selection process with centrifugation, the obtained nanoflakes were deposited on GC substrates via m-LB method, and used as photocathodes in PEC HER application. **Fig. 45a** presented their PEC activity in 0.5 M H_2SO_4 solution. All electrodes showed negligible photocurrent (a few μA). This might be caused by the improper LPE solvents for exfoliation, therefore, the organic solvents such as DCB and DMF, were used instead of green solvents in LPE process [86,235]. After the exfoliation, the organic solvents were replaced with EtOH, to remove the solvent from the GeS film easily during the film preparation process. **Fig. 45b** showed the PEC performance of the electrodes made from nanoflakes exfoliated in organic solvents, while negligible photocurrent was still observed.

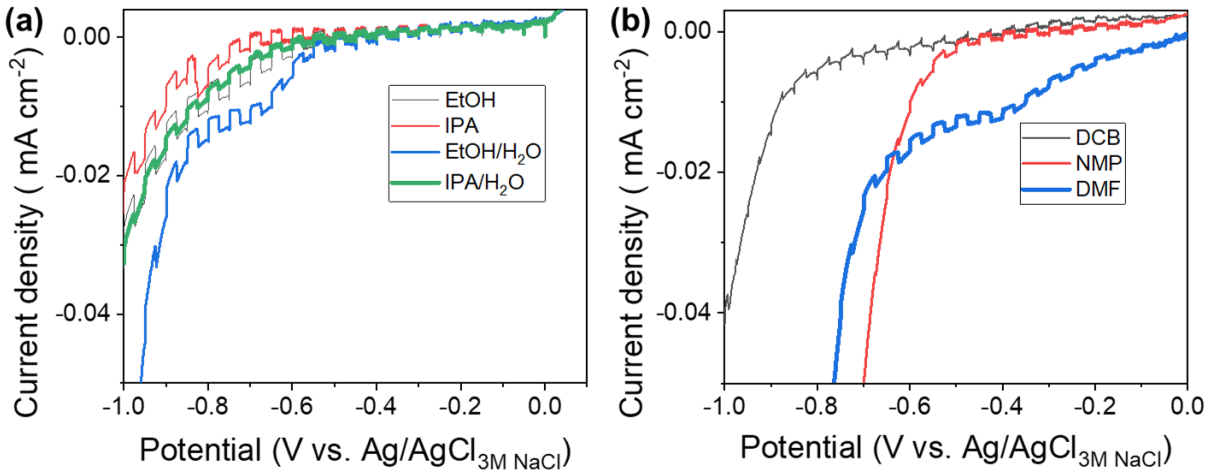

Fig. 45. Linear sweep photovoltammograms of GeS nanoflakes exfoliated in various solvents. (a) In EtOH, IPA, EtOH/H_2O and IPA/H_2O. (b) In DCB, NMP, and DMF, here, before the spray coating process, these organic solvents were replaced by EtOH. Linear sweep photovoltammograms were measured in Ar saturated 0.5 M H_2SO_4 solution, the scan rate was 2.5 mV s^{-1} in (a) and (b).

The fabricated macroelectrodes showed relatively low activity in PEC HER reaction, which can be possibly explained by several reasons: i) the exfoliation process destroys the structure of crystals, leading the resultant nanoflakes are not stable in the electrolyte media [236]. ii) abundant defects are produced after the liquid phase exfoliation process, acting as recombination centers for photogenerated charge carriers [22,29,57]. iii) the fabricated nanoflakes network possesses low conductivity [232–234]. Some common strategies, such as heterojunctions, tunnelling, and co-catalysts, used to enhance PEC performance were highlighted and discussed in our review paper [40].

6. Summary

Reviewing the literature, we found that some layered SCs have not been widely investigated in the field of PEC HER application yet. Therefore, exploring new layered metal chalcogenide SCs and studying their PEC performance in HER is the objective of my doctoral work. The first part of my doctoral work was to study the factors, including different solvents for LPE, the flakes edge density, Pt co-catalyst, and different synthesis methods, which can affect the PEC HER activity of SnSe flakes, aiming to achieve good PEC performance. The second part was to prepare GaTe nanoflakes using different exfoliation approaches (i.e., ME and LPE), and the PEC HER activity of GaTe micro- and macro-electrodes fabricated from such flakes was tested and compared, and the possible reasons for the limited photocurrent of macroelectrodes were discussed. The last part was to explore the PEC HER activity of macroelectrodes fabricated using other layered SCs. This work adds several candidates to the pool of photoelectrodes applicable in different PEC processes.

The most important results of my doctoral work can be summarized in the following points:

1. The solvents used in the liquid phase exfoliation affect the PEC HER performance of the obtained SnSe flakes. SnSe flakes were produced by exfoliating commercial SnSe crystals in different solvents, i.e., pure IPA and IPA/H_2O mixture with different IPA contents, using LPE method. The SnSe macroelectrodes were fabricated by depositing SnSe flakes on glassy carbon electrodes via m-LB method. The PEC HER performance was enhanced as the IPA content in the LPE solvents increased, and the pure IPA was found as the suitable solvent for SnSe, achieving the highest HER activity of 1.18 mA cm^{-2} photocurrent density at −0.69 V vs. RHE which was 10 times higher compared with IPA/H_2O case (1:3) (0.11 mA cm^{-2}).

2. Varying the particle size of SnSe crystals before liquid phase exfoliation, the edge density of the obtained SnSe flakes can be tuned. A sieving process was used to separate the as-received commercial SnSe crystals (diameter ≤ 12 mm) to three size fractions which were 12–1.6 mm, 1.6–0.69 mm and 0.4–0.16 mm size ranges named as L-, M- and S-SnSe, respectively, and then were exfoliated in pure IPA. The crystals after exfoliation are named as L-IPA-, M-IPA- and S-IPA-SnSe, respectively. These flakes had similar morphology characteristics, only the edge density values increased

with the decreasing initial crystal size. The photocathodes made from them by spray coating method showed the maximum photocurrent of ca. 2.3 mA cm^{-2}, which was higher than IPA-SnSe (1.18 mA cm^{-2}). These results demonstrate that edge density has no significant effect on the PEC HER activity of SnSe flakes.

3. Pt co-catalyst depositing on the SnSe surface can improve the PEC HER activity of SnSe flakes. Pt nanoparticles were anchored on the surface of SnSe by the photodeposition method, and the effect of different deposition factors, such as illumination time, the concentration of Pt precursor, and illumination intensity, on the PEC activity was investigated. Under optimal conditions, Pt decorated SnSe photocathode gave higher PEC HER activity than bare SnSe (4.39 vs. 2.14 mA cm^{-2}). IMPS results demonstrated that the Pt co-catalyst improved charge transfer kinetics and suppressed charge carrier recombination at the electrode/electrolyte interface.

4. The synthesis method of SnSe flakes has no significant effect on the PEC HER performance of SnSe. SnSe flakes were synthesized via the hydrothermal method, and spray-coated on GC substrate. The loading-dependent PEC HER activity indicated that 0.2 mg cm^{-2} was the optimal loading, achieving a maximum photocurrent of 3 mA cm^{-2}, which is in the same order of magnitude as LPE prepared SnSe flakes (2.3 mA cm^{-2}).

5. The mechanically exfoliated GaTe flakes can be applied for the PEC HER application. GaTe flakes were obtained by mechanically exfoliating as-received GaTe crystals, and immobilized on the SiO_2/Si substrate, and used as working electrode for PEC HER application. The PEC performance of GaTe microelectrode was conducted using our custom-developed PEC microscopy technique. It exhibited higher PEC activity with 6 M LiCl/1 M HCl than that of 6 M LiCl droplets. Meanwhile, GaTe has a thickness-dependent PEC HER performance, i.e., thicker flakes generally show higher PEC activity, achieving a maximum photocurrent of 6 mA cm^{-2} at −1.2 V vs. RHE with a thickness of 808±50 nm.

6. GaTe macroelectrode composed of liquid phase exfoliated flakes can be used for PEC HER application under concentrated illumination intensity. The loading dependent PEC activity indicated that the best performance was achieved with the mass loading

of 0.3 mg cm^{-2}, showing 0.57 ±0.01 mA cm^{-2} photocurrent at −0.74 V vs. RHE. Besides, an illumination intensity dependent PEC HER performance was found under optimal loading, achieving a maximum photocurrent of 4 mA cm^{-2} at − 0.74 V vs. RHE under 10 sun illumination. Stability tests were performed by 60 min long chronoamperometry, and 92% and 80% of initial activity remained under 1 and 10 sun illumination, respectively.

7. GaTe microelectrode fabricated by mechanical exfoliation showed higher photocurrent, compared to the GaTe macroelectrode composed of LPE-prepared GaTe flakes. This might be caused by that, the macroelectrode made from the LPE-prepared GaTe flakes has abundant edge defects, which can be avoided in the mechanically exfoliated flakes. Besides, the networks fabricated with solution-processed GaTe nanoflakes might have lower conductivity or carrier mobility compared to mechanically exfoliated GaTe microelectrodes, which can also result in lower PEC activity for GaTe macroelectrode.

8. The PEC HER performance of various layered and 2D materials was reviewed and summarized by a statistical analysis, revealing that most of such materials showed limited PEC HER activity (below 10 mA cm^{-2}). The possible reasons for limited PEC performance were analyzed and summarized from the reports, which are i) abundant defects are produced after exfoliation process, acting as recombination centers for photogenerated charge carriers. ii) the exfoliation process destroys the structure of crystals, leading to the resultant nanoflakes are not stable in the electrolyte media. iii) the fabricated nanoflakes network possesses low conductivity. The possible strategies to enhance PEC activity can be forming heterojunctions, tunnelling, and depositing co-catalysts.

References

[1] S. Chu, A. Majumdar, Opportunities and challenges for a sustainable energy future, Nature 488 (2012) 294–303. https://doi.org/10.1038/nature11475.

[2] N.S. Lewis, D.G. Nocera, Powering the Planet: Chemical Challenges in Solar Energy Utilization, Proc. Natl. Acad. Sci. 103 (2006) 15729–15735. https://doi.org/10.1073/pnas.0603395103.

[3] O. Ellabban, H. Abu-Rub, F. Blaabjerg, Renewable energy resources: Current status, future prospects and their enabling technology, Renew. Sustain. Energy Rev. 39 (2014) 748–764. https://doi.org/10.1016/j.rser.2014.07.113.

[4] B. Parida, S. Iniyan, R. Goic, A review of solar photovoltaic technologies, Renew. Sustain. Energy Rev. 15 (2011) 1625–1636. https://doi.org/10.1016/j.rser.2010.11.032.

[5] O. Khaselev, J.A. Turner, A monolithic photovoltaic-photoelectrochemical device for hydrogen production via water splitting, Science 280 (1998) 425–427. https://doi.org/10.1126/science.280.5362.425.

[6] M.A. Marwat, M. Humayun, M.W. Afridi, H. Zhang, M.R. Abdul Karim, M. Ashtar, M. Usman, S. Waqar, H. Ullah, C. Wang, W. Luo, Advanced Catalysts for Photoelectrochemical Water Splitting, ACS Appl. Energy Mater. 4 (2021) 12007–12031. https://doi.org/10.1021/acsaem.1c02548.

[7] M.G. Walter, E.L. Warren, J.R. McKone, S.W. Boettcher, Q. Mi, E.A. Santori, N.S. Lewis, Solar water splitting cells, Chem. Rev. 110 (2010) 6446–6473. https://doi.org/10.1021/cr1002326.

[8] M. Kan, Q. Wang, S. Hao, A. Guan, Y. Chen, Q. Zhang, Q. Han, G. Zheng, System Engineering Enhances Photoelectrochemical CO_2 Reduction, J. Phys. Chem. C 126 (2022) 1689−1700. https://doi.org/10.1021/acs.jpcc.1c10156.

[9] A Fujishima, K Honda, Electrochemical Photolysis of Water at a Semiconductor Electrode, Nature 238 (1972) 37–38. https://doi.org/10.1038/238037a0.

[10] T. Hisatomi, J. Kubota, K. Domen, Recent advances in semiconductors for photocatalytic and photoelectrochemical water splitting, Chem. Soc. Rev. 43 (2014) 7520–7535. https://doi.org/10.1039/c3cs60378d.

[11] K. Sun, S. Shen, Y. Liang, P.E. Burrows, S.S. Mao, D. Wang, Enabling silicon for Solar-Fuel production, Chem. Rev. 114 (2014) 8662–8719. https://doi.org/10.1021/cr300459q.

[12] E. Kecsenovity, B. Endrődi, P.S. Tóth, Y. Zou, R.A.W. Dryfe, K. Rajeshwar, C. Janáky, Enhanced Photoelectrochemical Performance of Cuprous Oxide/Graphene Nanohybrids, J. Am. Chem. Soc. 139 (2017) 6682–6692. https://doi.org/10.1021/jacs.7b01820.

[13] K. Rajeshwar, A. Thomas, C. Janaky, Photocatalytic activity of inorganic semiconductor surfaces: Myths, hype, and reality, J. Phys. Chem. Lett. 6 (2015) 139–147. https://doi.org/10.1021/jz502586p.

[14] W. Li, H. Wang, Z. Sun, Q. Wu, S. Xue, Si-doped Cu_2O/SiO_x composites for efficient photoelectrochemical water reduction, J. Power Sources 492 (2021) 229667. https://doi.org/10.1016/j.jpowsour.2021.229667.

[15] W. Zhang, Y. Huang, T. Gong, H. Feng, Activated carbon supported palladium-iron oxide catalysts fabricated by atomic layer deposition for hydrodechlorination of 1,4-dichlorobenzene, Catal. Commun. 93 (2017) 47–52. https://doi.org/10.1016/j.catcom.2017.01.026.

[16] K.K. Paul, N. Sreekanth, R.K. Biroju, A.J. Pattison, D. Escalera-López, A. Guha, T.N. Narayanan, N.V. Rees, W. Theis, P.K. Giri, Strongly enhanced visible light photoelectrocatalytic hydrogen evolution reaction in an n-doped MoS_2/TiO_2(B) heterojunction by selective decoration of platinum nanoparticles at the MoS_2 edge sites, J. Mater. Chem. A 6 (2018) 22681–22696. https://doi.org/10.1039/c8ta06783j.

[17] S. Seo, S. Kim, H. Choi, J. Lee, H. Yoon, G. Piao, J.C. Park, Y. Jung, J. Song, S.Y. Jeong, H. Park, S. Lee, Direct In Situ Growth of Centimeter-Scale Multi-Heterojunction $MoS_2/WS_2/WSe_2$ Thin-Film Catalyst for Photo-Electrochemical Hydrogen Evolution, Adv. Sci. 6 (2019) 1900301. https://doi.org/10.1002/advs.201900301.

[18] R.J. Britto, J.L. Young, Y. Yang, M.A. Steiner, D.T. Lafehr, D.J. Friedman, M. Beard, T.G. Deutsch, T.F. Jaramillo, Interfacial engineering of gallium indium phosphide photoelectrodes for hydrogen evolution with precious metal and non-precious metal based catalysts, J. Mater. Chem. A 7 (2019) 16821–16832. https://doi.org/10.1039/c9ta05247j.

[19] A.M. Beiler, D. Khusnutdinova, S.I. Jacob, G.F. Moore, Solar Hydrogen Production Using Molecular Catalysts Immobilized on Gallium Phosphide (111)A and (111)B Polymer-Modified Photocathodes, ACS Appl. Mater. Interfaces 8 (2016) 10038–10047. https://doi.org/10.1021/acsami.6b01557.

[20] H. Coskun, F.H. Isikgor, Z. Chen, M. Imran, B. Li, Q. Xu, J. Ouyang, Thermally evaporated two-dimensional SnS as an efficient and stable electron collection interlayer for inverted planar perovskite solar cells, J. Mater. Chem. A 7 (2019) 4759–4765. https://doi.org/10.1039/c8ta10876e.

[21] I.S. Kwon, I.H. Kwak, T.T. Debela, H.G. Abbas, Y.C. Park, J.P. Ahn, J. Park, H.S. Kang, Se-Rich $MoSe_2$ Nanosheets and Their Superior Electrocatalytic Performance for Hydrogen Evolution Reaction, ACS Nano 14 (2020) 6295–6304. https://doi.org/10.1021/acsnano.0c02593.

[22] X. Yu, K. Sivula, Photogenerated Charge Harvesting and Recombination in Photocathodes of Solvent-Exfoliated WSe_2, Chem. Mater. 29 (2017) 6863–6875. https://doi.org/10.1021/acs.chemmater.7b02018.

[23] P.S. Tóth, G. Szabó, C. Janáky, Structural Features Dictate the Photoelectrochemical Activities of Two-Dimensional $MoSe_2$ and WSe_2 Nanostructures, J. Phys. Chem. C 125 (2021) 7701–7710. https://doi.org/10.1021/acs.jpcc.1c01265.

[24] W. Kautek, J. Gobrecht, H. Gerischer, The Applicability of Semiconducting Layered Materials for Electrochemical Solar Energy Conversion, Berichte Der Bunsengesellschaft Für Phys. Chemie 84 (1980) 1034–1040. https://doi.org/10.1002/bbpc.19800841021.

[25] H.J. Lewerenz, A. Heller, F.J. Disalvo, Relationship between Surface Morphology and Solar Conversion Efficiency of WSe_2 Photoanodes, J. Am. Chem. Soc. 102 (1980) 1877–1880. https://doi.org/10.1021/ja00526a019.

[26] W. Kautek, H. Gerischer, Anisotropic photocorrosion of n-type MoS_2, $MoSe_2$, and WSe_2 single crystal surfaces: the role of cleavage steps, line and screw dislocations, Surf. Sci. 119 (1982) 46–60. https://doi.org/10.1016/0039-6028(82)90186-8.

[27] H.D. Abruna, A.J. Bard, Semiconductor Electrodes. 44. Photoelectrochemistry at Polycrystalline p-Type WSe_2 Films, J. Electrochem. Soc. 129 (1982) 673–675. https://doi.org/10.1149/1.2123949.

[28] W. Yang, J. Park, H.C. Kwon, O.S. Hutter, L.J. Phillips, J. Tan, H. Lee, J. Lee, S.D. Tilley, J.D. Major, J. Moon, Solar water splitting exceeding 10% efficiency: Via low-cost Sb_2Se_3 photocathodes coupled with semitransparent perovskite photovoltaics, Energy Environ. Sci. 13 (2020) 4362–4370. https://doi.org/10.1039/d0ee02959a.

[29] X. Yu, M.S. Prévot, N. Guijarro, K. Sivula, Self-assembled 2D WSe_2 thin films for photoelectrochemical hydrogen production, Nat. Commun. 6 (2015) 7596. https://doi.org/10.1038/ncomms8596.

[30] H. Li, C. Yang, X. Wang, J. Zhang, J. Xi, G. Du, Z. Ji, Mixed 3D/2D dimensional TiO_2 nanoflowers/$MoSe_2$ nanosheets for enhanced photoelectrochemical hydrogen generation, J. Am. Ceram. Soc. 103 (2020) 1187–1196. https://doi.org/10.1111/jace.16807.

[31] X. Xu, Y. Liu, Y. Zhu, X. Fan, Y. Li, F. Zhang, G. Zhang, W. Peng, Fabrication of a Cu_2O/g-C_3N_4/WS_2 Triple-Layer Photocathode for Photoelectrochemical Hydrogen Evolution, ChemElectroChem 4 (2017) 1498–1502. https://doi.org/10.1002/celc.201700014.

[32] J. Park, W. Yang, J. Tan, H. Lee, J.W. Yun, S.G. Shim, Y.S. Park, J. Moon, Hierarchal Nanorod-Derived Bilayer Strategy to Enhance the Photocurrent Density of Sb_2Se_3 Photocathodes for Photoelectrochemical Water Splitting, ACS Energy Lett. 5 (2020) 136–145. https://doi.org/10.1021/acsenergylett.9b02486.

[33] I.H. Kwak, I.S. Kwon, J.H. Lee, Y.R. Lim, J. Park, Chalcogen-vacancy group VI transition metal dichalcogenide nanosheets for electrochemical and photoelectrochemical hydrogen evolution, J. Mater. Chem. C 9 (2021) 101–109. https://doi.org/10.1039/d0tc04715e.

[34] J.R. McKone, A.P. Pieterick, H.B. Gray, N.S. Lewis, Hydrogen evolution from Pt/Ru-coated p-type WSe_2 photocathodes, J. Am. Chem. Soc. 135 (2013) 223–231. https://doi.org/10.1021/ja308581g.

[35] K. Roy, S. Maitra, D. Ghosh, P. Kumar, P. Devi, 2D-Heterostructure assisted activation of MoS_2 basal plane for enhanced photoelectrochemical hydrogen evolution reaction, Chem. Eng. J. 435 (2022) 134963. https://doi.org/10.1016/j.cej.2022.134963.

[36] D. Hu, J. Xiang, Q. Zhou, S. Su, Z. Zhang, X. Wang, M. Jin, L. Nian, R. Nözel, G. Zhou, Z. Zhang, J. Liu, One-step chemical vapor deposition of MoS_2 nanosheets on SiNWs as photocathodes for efficient and stable solar-driven hydrogen production, Nanoscale 10 (2018) 3518–3525. https://doi.org/10.1039/c7nr09235k.

[37] X. Huang, H. Woo, D. Lee, P. Wu, M. Song, J.W. Choi, High-efficiency photon-capturing capability of two-dimensional SnS nanosheets for photoelectrochemical cells, Catalysts 11 (2021) 236. https://doi.org/10.3390/catal11020236.

[38] Z. Ma, P. Konze, M. Küpers, K. Wiemer, D. Hoffzimmer, S. Neumann, S. Kunz, U. Simon, R. Dronskowski, A. Slabon, Elucidation of the Active Sites for Monodisperse FePt and Pt Nanocrystal Catalysts for p-WSe_2 Photocathodes, J. Phys. Chem. C 124 (2020) 11877–11885. https://doi.org/10.1021/acs.jpcc.0c01288.

[39] S.A. Monny, L. Zhang, Z. Wang, B. Luo, M. Konarova, A. Du, L. Wang, Fabricating highly efficient heterostructured $CuBi_2O_4$ photocathodes for unbiased water splitting, J. Mater. Chem. A 8 (2020) 2498–2504. https://doi.org/10.1039/c9ta10975g.

[40] P.S. Tóth, B. Qianqian, C. Janáky, Photoelectrochemistry of two-dimensional and layered materials: a brief review, J. Solid State Electrochem. 27 (2023) 1701–1715. https://doi.org/10.1007/s10008-023-05503-z.

[41] Z. Chen, A.J. Forman, T.F. Jaramillo, Bridging the gap between bulk and nanostructured photoelectrodes: The impact of surface states on the electrocatalytic and photoelectrochemical properties of MoS_2, J. Phys. Chem. C 117 (2013) 9713–9722. https://doi.org/10.1021/jp311375k.

[42] K. S. Novoselov, A. K. Geim, S. V. Morozov, D. Jiang, Y. Zhang, S. V. Dubonos, I. V. Grigorieva, A. A. Firsov, Electric Field Effect in Atomically Thin Carbon Films, Science 306 (2004) 666–669. https://doi.org/10.1126/science.1102896.

[43] M. Velický, P.S. Toth, From two-dimensional materials to their heterostructures: An electrochemist's perspective, Appl. Mater. Today 8 (2017) 68–103. https://doi.org/10.1016/j.apmt.2017.05.003.

[44] D.A.C. Brownson, L.J. Munro, D.K. Kampouris, C.E. Banks, Electrochemistry of graphene: Not such a beneficial electrode material?, RSC Adv. 1 (2011) 978–988. https://doi.org/10.1039/c1ra00393c.

[45] M. Velický, D.F. Bradley, A.J. Cooper, E.W. Hill, I.A. Kinloch, A. Mishchenko, K.S. Novoselov, H. V. Patten, P.S. Toth, A.T. Valota, S.D. Worrall, R.A.W. Dryfe, Electron transfer kinetics on mono- and multilayer graphene, ACS Nano 8 (2014) 10089–10100. https://doi.org/10.1021/nn504298r.

[46] H.J. Lewerenz, H. Gerischer, M. Lübke, Photoelectrochemistry of WSe_2 Electrodes: Comparison of Stepped and Smooth Surfaces, J. Electrochem. Soc. 131 (1984) 100–104. https://doi.org/10.1149/1.2115467.

[47] M. Velický, M.A. Bissett, C.R. Woods, P.S. Toth, T. Georgiou, I.A. Kinloch, K.S. Novoselov, R.A.W. Dryfe, Photoelectrochemistry of Pristine Mono- and Few-Layer MoS_2, Nano Lett. 16 (2016) 2023–2032. https://doi.org/10.1021/acs.nanolett.5b05317.

[48] M.A. Todt, A.E. Isenberg, S.U. Nanayakkara, E.M. Miller, J.B. Sambur, Single-Nanoflake Photo-Electrochemistry Reveals Champion and Spectator Flakes in Exfoliated $MoSe_2$ Films, J. Phys. Chem. C 122 (2018) 6539–6545. https://doi.org/10.1021/acs.jpcc.7b12715.

[49] J.M. Velazquez, J. John, D. V. Esposito, A. Pieterick, R. Pala, G. Sun, X. Zhou, Z. Huang, S. Ardo, M.P. Soriaga, B.S. Brunschwig, N.S. Lewis, A scanning probe investigation of the role of surface motifs in the behavior of p-WSe_2 photocathodes, Energy Environ. Sci. 9 (2016) 164–175. https://doi.org/10.1039/c5ee02530c.

[50] M. Velický, M.A. Bissett, P.S. Toth, H. V. Patten, S.D. Worrall, A.N.J. Rodgers, E.W. Hill, I.A. Kinloch, K.S. Novoselov, T. Georgiou, L. Britnell, R.A.W. Dryfe, Electron transfer kinetics on natural crystals of MoS_2 and graphite, Phys. Chem. Chem. Phys. 17 (2015) 17844–17853. https://doi.org/10.1039/c5cp02490k.

[51] P.S. Toth, M. Velický, M.A. Bissett, T.J.A. Slater, N. Savjani, A.K. Rabiu, A.M. Rakowski, J.R. Brent, S.J. Haigh, P. O'Brien, R.A.W. Dryfe, Asymmetric MoS_2/Graphene/Metal Sandwiches: Preparation, Characterization, and Application, Adv. Mater. 28 (2016) 8256–8264. https://doi.org/10.1002/adma.201600484.

[52] D. Eisenberg, Imaging the Anisotropic Reactivity of a Tungsten Diselenide Photocathode, ChemElectroChem 2 (2015) 1259–1263. https://doi.org/10.1002/celc.201500103.

[53] J.W. Hill, C.M. Hill, Directly Mapping Photoelectrochemical Behavior within Individual Transition Metal Dichalcogenide Nanosheets, Nano Lett. 19 (2019) 5710–5716. https://doi.org/10.1021/acs.nanolett.9b02336.

[54] B. Tao, P.R. Unwin, C.L. Bentley, Nanoscale Variations in the Electrocatalytic Activity of Layered Transition-Metal Dichalcogenides, J. Phys. Chem. C 124 (2020) 789–798. https://doi.org/10.1021/acs.jpcc.9b10279.

[55] M.A. Edwards, P. Bertoncello, P.R. Unwin, Slow diffusion reveals the intrinsic electrochemical activity of basal plane highly oriented pyrolytic graphite electrodes, J. Phys. Chem. C 113 (2009) 9218–9223. https://doi.org/10.1021/jp8092918.

[56] P.S. Tóth, G. Szabó, G. Bencsik, G.F. Samu, K. Rajeshwar, C. Janáky, Peeling off the surface: Pt-decoration of WSe_2 nanoflakes results in exceptional photoelectrochemical HER activity, SusMat (2022) 1–12. https://doi.org/10.1002/sus2.86.

[57] F. Bozheyev, K. Harbauer, C Zahn, D Friedrich, K. Ellmer, Highly (001)-textured p-type WSe_2 Thin Films as Efficient Large-Area Photocathodes for Solar Hydrogen Evolution, Sci. Rep. 7 (2017) 16003. https://doi.org/10.1038/s41598-017-16283-8.

[58] X. Yu, A. Rahmanudin, X.A. Jeanbourquin, D. Tsokkou, N. Guijarro, N. Banerji, K. Sivula, Hybrid heterojunctions of solution-processed semiconducting 2D transition metal dichalcogenides, ACS Energy Lett. 2 (2017) 524–531. https://doi.org/10.1021/acsenergylett.6b00707.

[59] Y. Pi, B. Liu, Z. Li, Y. Zhu, Y. Li, F. Zhang, G. Zhang, W. Peng, X. Fan, TiO_2 nanorod arrays decorated with exfoliated WS_2 nanosheets for enhanced photoelectrochemical water oxidation, J. Colloid Interface Sci. 545 (2019) 282–288. https://doi.org/10.1016/j.jcis.2019.03.041.

[60] Q. Ba, P.S. Tóth, Á. Vass, K. Rajeshwar, C. Janáky, Photoelectrochemical hydrogen evolution on macroscopic electrodes of exfoliated SnSe flakes, Appl. Catal. A Gen. 661 (2023) 119233. https://doi.org/10.1016/j.apcata.2023.119233.

[61] X. Jiang, B. Sun, Y. Song, M. Dou, J. Ji, F. Wang, One-pot synthesis of MoS_2/WS_2 ultrathin nanoflakes with vertically aligned structure on indium tin oxide as a photocathode for enhanced photo-assistant electrochemical hydrogen evolution reaction, RSC Adv. 7 (2017) 49309–49319. https://doi.org/10.1039/c7ra10762e.

[62] R. Wang, Y. Lyu, S. Du, S. Zhao, H. Li, L. Tao, S.P. Jiang, J. Zheng, S. Wang, Defect repair of tin selenide photocathode: Via in situ selenization: Enhanced photoelectrochemical performance and environmental stability, J. Mater. Chem. A 8 (2020) 5342–5349. https://doi.org/10.1039/c9ta13288k.

[63] A. Lukinskas, V. Jasulaitiene, P. Lukinskas, I. Savickaja, P. Kalinauskas, Electrochemical formation of nanometric layers of tin selenides on Ti surface, Electrochim. Acta 51 (2006) 6171–6178. https://doi.org/10.1016/j.electacta.2006.01.072.

[64] C. Lu, Y. Zhang, L. Zhang, Q. Yin, Preparation and photoelectrochemical properties of SnS/SnSe and SnSe/SnS bilayer structures fabricated via electrodeposition, Appl. Surf. Sci. 484 (2019) 560–567. https://doi.org/10.1016/j.apsusc.2019.04.104.

[65] F. Bonaccorso, A. Lombardo, T. Hasan, Z. Sun, L. Colombo, A.C. Ferrari, Production and processing of graphene and 2d crystals, Mater. Today 15 (2012) 564–589. https://doi.org/10.1016/S1369-7021(13)70014-2.

[66] V. Nicolosi, M. Chhowalla, M.G. Kanatzidis, M.S. Strano, J.N. Coleman, Liquid exfoliation of layered materials, Science 340 (2013) 1226419. https://doi.org/10.1126/science.1226419.

[67] S. Bellani, A. Bartolotta, A. Agresti, G. Calogero, G. Grancini, A. Di Carlo, E. Kymakis, F. Bonaccorso, Solution-processed two-dimensional materials for next-generation photovoltaics, Chem. Soc. Rev. 50 (2021) 11870–11965. https://doi.org/10.1039/d1cs00106j.

[68] T. Taniguchi, L. Nurdiwijayanto, R. Ma, T. Sasaki, Chemically exfoliated inorganic nanosheets for nanoelectronics Chemically exfoliated inorganic nanosheets for nanoelectronics, Appl. Phys. Rev. 9 (2022) 021313. https://doi.org/10.1063/5.0083109.

[69] H. Gómez, A. Maldonado, R. Asomoza, E.P. Zironi, J. Cañetas-Ortega, J. Palacios-Gómez, Characterization of indium-doped zinc oxide films deposited by pyrolytic spray with different indium compounds as dopants, Thin Solid Films 293 (1997) 117–123. https://doi.org/10.1016/S0040-6090(96)09001-3.

[70] Y. Ye, Y. Xian, J. Cai, K. Lu, Z. Liu, T. Shi, J. Du, Y. Leng, R. Wei, W. Wang, X. Liu, G. Bi, J. Qiu, Linear and Nonlinear Optical Properties of Few-Layer Exfoliated SnSe Nanosheets, Adv. Opt. Mater. 7 (2019) 1800579. https://doi.org/10.1002/adom.201800579.

[71] F. Bonaccorso, A. Bartolotta, J.N. Coleman, C. Backes, 2D-Crystal-Based Functional Inks, Adv. Mater. 28 (2016) 6136–6166. https://doi.org/10.1002/adma.201506410.

[72] S. Ramanathan, S.C.B. Gopinath, M.K.M. Arshad, P. Poopalan, V. Perumal, Nanoparticle synthetic methods: strength and limitations, INC, (2021) 31–43. https://doi.org/10.1016/b978-0-12-821163-2.00002-9.

[73] Q. Ding, F. Meng, C.R. English, M. Cabán-Acevedo, M.J. Shearer, D. Liang, A.S. Daniel, R.J. Hamers, S. Jin, Efficient photoelectrochemical hydrogen generation using heterostructures of Si and chemically exfoliated metallic MoS_2, J. Am. Chem. Soc. 136 (2014) 8504–8507. https://doi.org/10.1021/ja5025673.

[74] T.N. Trung, D.B. Seo, N.D. Quang, D. Kim, E.T. Kim, Enhanced photoelectrochemical activity in the heterostructure of vertically aligned few-layer MoS_2 flakes on ZnO, Electrochim. Acta 260 (2018) 150–156. https://doi.org/10.1016/j.electacta.2017.11.089.

[75] S. Hussain, S. Hussain, A. Waleed, M.M. Tavakoli, S. Yang, M.K. Rauf, Z. Fan, M.A. Nadeem, Spray Pyrolysis Deposition of $ZnFe_2O_4$/Fe_2O_3 Composite Thin Films on Hierarchical 3-D Nanospikes for Efficient Photoelectrochemical Oxidation of Water, J. Phys. Chem. C 121 (2017) 18360–18368. https://doi.org/10.1021/acs.jpcc.7b05266.

[76] P. Li, J. Zhang, H. Wang, H. Jing, J. Xu, X. Sui, H. Hu, H. Yin, The photoelectric catalytic reduction of CO_2 to methanol on CdSeTe NSs/TiO_2 NTs, Catal. Sci. Technol. 4 (2014) 1070–1077. https://doi.org/10.1039/c3cy00978e.

[77] F. Zhang, Y. Chen, W. Zhou, C. Ren, H. Gao, G. Tian, Hierarchical SnS_2/$CuInS_2$ Nanosheet Heterostructure Films Decorated with C_{60} for Remarkable Photoelectrochemical Water Splitting, ACS Appl. Mater. Interfaces 11 (2019) 9093–9101. https://doi.org/10.1021/acsami.8b21222.

[78] H. Sopha, A.T. Tesfaye, R. Zazpe, J. Michalicka, F. Dvorak, L. Hromadko, M. Krbal, J. Prikryl, T. Djenizian, J.M. Macak, ALD growth of MoS_2 nanosheets on TiO_2 nanotube supports, FlatChem 17 (2019) 100130. https://doi.org/10.1016/j.flatc.2019.100130.

[79] C. Martella, P. Melloni, E. Cinquanta, E. Cianci, M. Alia, M. Longo, A. Lamperti, S. Vangelista, M. Fanciulli, A. Molle, Engineering the Growth of MoS_2 via Atomic Layer Deposition of Molybdenum Oxide Film Precursor, Adv. Electron. Mater. 2 (2016) 1600330. https://doi.org/10.1002/aelm.201600330.

[80] N. Baig, I. Kammakakam, W. Falath, I, Nanomaterials: A review of synthesis methods, properties, recent progress, and challenges, Mater. Adv. 2 (2021) 1821–1871. https://doi.org/10.1039/d0ma00807a.

[81] M. Gutiérrez, A. Henglein, Preparation of colloidal semiconductor solutions of MoS_2 and WSe_2 via sonication, Ultrasonics 27 (1989) 259–261. https://doi.org/10.1016/0041-624X(89)90066-8.

[82] Y. Hernandez, V. Nicolosi, M. Lotya, F.M. Blighe, Z. Sun, S. De, I.T. McGovern, B. Holland, M. Byrne, Y.K. Gun'ko, J.J. Boland, P. Niraj, G. Duesberg, S. Krishnamurthy, R. Goodhue, J. Hutchison, V. Scardaci, A.C. Ferrari, J.N. Coleman, High-yield production of graphene by liquid-phase exfoliation of graphite, Nat. Nanotechnol. 3 (2008) 563–568. https://doi.org/10.1038/nnano.2008.215.

[83] J.N. Coleman, M. Lotya, A. O'neill, S.D. Bergin, P.J. King, U. Khan, K. Young, A. Gaucher, S. De, R.J. Smith, I. V Shvets, S.K. Arora, G. Stanton, H.-Y. Kim, K. Lee, G.T. Kim, G.S. Duesberg, T. Hallam, J.J. Boland, J.J. Wang, J.F. Donegan, J.C. Grunlan, G. Moriarty, A. Shmeliov, R.J. Nicholls, J.M. Perkins, E.M. Grieveson, K. Theuwissen, D.W. Mccomb, P.D. Nellist, V. Nicolosi, Two-Dimensional Nanosheets Produced by Liquid Exfoliation of Layered Materials, Science 331 (2011) 568–571. https://doi.org/10.1126/science.1194975.

[84] G. Cunningham, M. Lotya, C.S. Cucinotta, S. Sanvito, S.D. Bergin, R. Menzel, M.S.P. Shaffer, J.N. Coleman, Solvent exfoliation of transition metal dichalcogenides: Dispersibility of exfoliated nanosheets varies only weakly between compounds, ACS Nano 6 (2012) 3468–3480. https://doi.org/10.1021/nn300503e.

[85] D. Lam, K.S. Chen, J. Kang, X. Liu, M.C. Hersam, Anhydrous Liquid-Phase Exfoliation of Pristine Electrochemically Active GeS Nanosheets, Chem. Mater. 30 (2018) 2245–2250. https://doi.org/10.1021/acs.chemmater.7b04652.

[86] J. Fernandes, S.S. Nemala, G. De Bellis, A. Capasso, Green Solvents for the Liquid Phase Exfoliation Production of Graphene: The Promising Case of Cyrene, Front. Chem. 10 (2022) 878799. https://doi.org/10.3389/fchem.2022.878799.

[87] A. O'Neill, U. Khan, J.N. Coleman, Preparation of high concentration dispersions of exfoliated MoS_2 with increased flake size, Chem. Mater. 24 (2012) 2414–2421. https://doi.org/10.1021/cm301515z.

[88] C. Backes, B.M. Szydłowska, A. Harvey, S. Yuan, V. Vega-Mayoral, B.R. Davies, P.L. Zhao, D. Hanlon, E.J.G. Santos, M.I. Katsnelson, W.J. Blau, C. Gadermaier, J.N. Coleman, Production of highly monolayer enriched dispersions of liquid-exfoliated nanosheets by liquid cascade centrifugation, ACS Nano 10 (2016) 1589–1601. https://doi.org/10.1021/acsnano.5b07228.

[89] N.T. Hoang, J.H. Lee, T. H. Vu, S. Cho, M.J. Seong, Layer thickness-dependent optical properties of GaTe, Appl. Surf. Sci. 638 (2023) 158022. https://doi.org/10.1016/j.apsusc.2023.158022.

[90] F. Geng, R. Ma, Y. Ebina, Y. Yamauchi, N. Miyamoto, T. Sasaki, Gigantic swelling of inorganic layered materials: A bridge to molecularly thin two-dimensional nanosheets, J. Am. Chem. Soc. 136 (2014) 5491–5500. https://doi.org/10.1021/ja501587y.

[91] H. Ju, J. Kim, Chemically Exfoliated SnSe Nanosheets and Their SnSe/Poly(3,4-ethylenedioxythiophene):Poly(styrenesulfonate) Composite Films for Polymer Based Thermoelectric Applications, ACS Nano 10 (2016) 5730–5739. https://doi.org/10.1021/acsnano.5b07355.

[92] J. Gohil, V. Jethwa, V.M. Pathak, G.K. Solanki, P. Chauhan, A.B. Patel, C. Zankat, N. Patel, Enhanced visible-light photoresponse of DVT-grown Ni-doped SnSe crystal, J. Mater. Sci. Mater. Electron. 33 (2022) 10086–10095. https://doi.org/10.1007/s10854-022-07998-0.

[93] D.H. Kim, J.C. Park, J. Park, D.Y. Cho, W.H. Kim, B. Shong, J.H. Ahn, T.J. Park, Wafer-Scale Growth of a MoS_2 Monolayer via One Cycle of Atomic Layer Deposition: An Adsorbate Control Method, Chem. Mater. 33 (2021) 4099–4105. https://doi.org/10.1021/acs.chemmater.1c00729.

[94] G. Yang, S.J. Park, Conventional and microwave hydrothermal synthesis and application of functional materials: A review, Materials. 12 (2019) 1177. https://doi.org/10.3390/ma12071177.
[95] Y. Cheng, J. Zhang, C. Chen, X. Xiong, J. Zeng, J. Xi, Y.J. Yuan, Z. Ji, A novel 2D/2D $MoSe_2$/SnSe heterojunction photocatalyst with large carrier transmission channel shows excellent photoelectrochemical performance, Appl. Surf. Sci. 563 (2021) 150311. https://doi.org/10.1016/j.apsusc.2021.150311.
[96] O.N. Oliveira, L. Caseli, K. Ariga, The Past and the Future of Langmuir and Langmuir-Blodgett Films, Chem. Rev. 122 (2022) 6459–6513. https://doi.org/10.1021/acs.chemrev.1c00754.
[97] G. Cunningham, U. Khan, C. Backes, D. Hanlon, D. McCloskey, J.F. Donegan, J.N. Coleman, Photoconductivity of solution-processed MoS_2 films, J. Mater. Chem. C 1 (2013) 6899–6904. https://doi.org/10.1039/c3tc31402b.
[98] G. Bianca, M.I. Zappia, S. Bellani, Z. Sofer, M. Serri, L. Najafi, R. Oropesa-Nunez, B. Martín-García, T. Hartman, L. Leoncino, D. Sedmidubský, V. Pellegrini, G. Chiarello, F. Bonaccorso, Liquid-phase exfoliated GeSe nanoflakes for photoelectrochemical-type photodetectors and photoelectrochemical water splitting, ACS Appl. Mater. Interfaces 12 (2020) 48598–48613. https://doi.org/10.1021/acsami.0c14201.
[99] S. Biswas, L.T. Drzal, A novel approach to create a highly ordered monolayer film of graphene nanosheets at the liquid-liquid interface, Nano Lett. 9 (2009) 167–172. https://doi.org/10.1021/nl802724f.
[100] F. Kim, L.J. Cote, J. Huang, Graphene oxide: Surface activity and two-dimensional assembly, Adv. Mater. 22 (2010) 1954–1958. https://doi.org/10.1002/adma.200903932.
[101] R.A. Wells, H. Johnson, C.R. Lhermitte, S. Kinge, K. Sivula, Roll-to-Roll Deposition of Semiconducting 2D Nanoflake Films of Transition Metal Dichalcogenides for Optoelectronic Applications, ACS Appl. Nano Mater. 2 (2019) 7705–7712. https://doi.org/10.1021/acsanm.9b01774.
[102] T. Carey, C. Jones, F. Le Moal, D. Deganello, F. Torrisi, Spray-Coating Thin Films on Three-Dimensional Surfaces for a Semitransparent Capacitive-Touch Device, ACS Appl. Mater. Interfaces 10 (2018) 19948–19956. https://doi.org/10.1021/acsami.8b02784.
[103] M. Habibi, M.-R. Ahmadian-Yazdi, M. Eslamian, Optimization of spray coating for the fabrication of sequentially deposited planar perovskite solar cells, J. Photonics Energy 7 (2017) 022003. https://doi.org/10.1117/1.jpe.7.022003.
[104] L. Hao, Y. Du, Z. Wang, Y. Wu, H. Xu, S. Dong, H. Liu, Y. Liu, Q. Xue, Z. Han, K. Yan, M. Dong, Wafer-size growth of 2D layered SnSe films for UV-Visible-NIR photodetector arrays with high responsitivity, Nanoscale 12 (2020) 7358–7365. https://doi.org/10.1039/d0nr00319k.
[105] Y.K. Lee, Z. Luo, S.P. Cho, M.G. Kanatzidis, I. Chung, Surface Oxide Removal for Polycrystalline SnSe Reveals Near-Single-Crystal Thermoelectric Performance, Joule 3 (2019) 719–731. https://doi.org/10.1016/j.joule.2019.01.001.
[106] S. Gowthamaraju, U.P. Deshpande, P.A. Bhobe, Augmentation of the thermoelectric properties of polycrystalline Tin selenides via formation of SnSe/$SnSe_2$ composites, J. Mater. Sci. Mater. Electron. 32 (2021) 11781–11790. https://doi.org/10.1007/s10854-021-05807-8.
[107] Y. Huang, L. Li, Y.H. Lin, C.W. Nan, Liquid Exfoliation Few-Layer SnSe Nanosheets with Tunable Band Gap, J. Phys. Chem. C 121 (2017) 17530–17537. https://doi.org/10.1021/acs.jpcc.7b06096.
[108] K. Patel, P. Chauhan, A.B. Patel, G.K. Solanki, K.D. Patel, V.M. Pathak, Orthorhombic SnSe Nanocrystals for Visible-Light Photodetectors, ACS Appl. Nano Mater. 3 (2020) 11143–11151. https://doi.org/10.1021/acsanm.0c02301.
[109] X. Liu, Y. Li, B. Zhou, X. Wang, A.N. Cartwright, M.T. Swihart, Shape-controlled synthesis of SnE (E = S, Se) semiconductor nanocrystals for optoelectronics, Chem. Mater. 26 (2014) 3515–3521. https://doi.org/10.1021/cm501023w.
[110] S. Liu, X. Guo, M. Li, W.H. Zhang, X. Liu, C. Li, Solution-phase synthesis and characterization of single-crystalline SnSe nanowires, Angew. Chemie - Int. Ed. 50 (2011) 12050–12053. https://doi.org/10.1002/anie.201105614.
[111] L. Liao, M. Xiao, P. Jia, Y. Jin, J. Liu, Q. Zhang, Effect of calcination temperature on one-step in situ preparation of SnSe/SnO_2 heterojunction and its photocatalytic performance, J. Solid State Chem. 324 (2023) 124113. https://doi.org/10.1016/j.jssc.2023.124113.
[112] X. Ren, X. Qi, Y. Shen, G. Xu, J. Li, Z. Li, Z. Huang, J. Zhong, Synthesis of SnSe nanosheets by hydrothermal intercalation and exfoliation route and their photoresponse properties, Mater. Sci. Eng. B 214 (2016) 46–50. https://doi.org/10.1016/j.mseb.2016.09.001.
[113] B. Singh, S. Gautam, G.C. Behera, V. Aggarwal, R. Kumar, M. Kumar, R. Ganesan, V.N. Singh, S.C. Roy, S.S. Kushvaha, Bi_2Se_3/SnSe heterojunction on flexible Ti foil for enhanced photoelectrochemical water splitting, Mater. Lett. 355 (2024) 135503. https://doi.org/10.1016/j.matlet.2023.135503.

[114] A.A.A. Abdelazeez, A.B.G. Trabelsi, F.H. Alkallas, M. Rabia, Successful 2D MoS_2 nanosheets synthesis with SnSe grid-like nanoparticles: Photoelectrochemical hydrogen generation and solar cell applications, Sol. Energy 248 (2022) 251–259. https://doi.org/10.1016/j.solener.2022.10.058.

[115] P. Mandal, U.K. Ghorui, A. Mondal, D. Banerjee, Photoelectrochemical Performance of Tin Selenide (SnSe) Thin Films Prepared by Two Different Techniques, Electron. Mater. Lett. 18 (2022) 381–390. https://doi.org/10.1007/s13391-022-00349-5.

[116] S. V. Barma, S.B. Jathar, Y.T. Huang, Y.A. Jadhav, G.K. Rahane, A. V. Rokade, M.P. Nasane, S.N. Rahane, R.W. Cross, M.P. Suryawanshi, S.B. Jo, R.L.Z. Hoye, S.R. Jadkar, N.Y. Dzade, S.R. Rondiya, Synthesis and Interface Engineering in Heterojunctions of Tin-Selenide-Based Nanostructures for Photoelectrochemical Water Splitting, ACS Appl. Nano Mater. 7 (2024) 1986−1999. https://doi.org/10.1021/acsanm.3c05202.

[117] D. Zheng, H. Fang, M. Long, F. Wu, P. Wang, F. Gong, X. Wu, J.C. Ho, L. Liao, W. Hu, High-Performance Near-Infrared Photodetectors Based on p-Type SnX (X = S, Se) Nanowires Grown via Chemical Vapor Deposition, ACS Nano 12 (2018) 7239–7245. https://doi.org/10.1021/acsnano.8b03291.

[118] B. Subramanian, T. Mahalingam, C. Sanjeeviraja, M. Jayachandran, M.J. Chockalingam, Electrodeposition of Sn, Se, SnSe and the material properties of SnSe films, Thin Solid Films 357 (1999) 119–124. https://doi.org/10.1016/S0040-6090(99)00644-6.

[119] Z. Jia, J. Xiang, F. Wen, R. Yang, C. Hao, Z. Liu, Enhanced Photoresponse of SnSe-Nanocrystals-Decorated WS_2 Monolayer Phototransistor, ACS Appl. Mater. Interfaces 8 (2016) 4781–4788. https://doi.org/10.1021/acsami.5b12137.

[120] F. Li, H. Chen, L. Xu, F. Zhang, P. Yin, T. Yang, T. Shen, J. Qi, Y. Zhang, D. Li, Y. Ge, H. Zhang, Defect Engineering in Ultrathin SnSe Nanosheets for High- Performance Optoelectronic Applications, ACS Appl. Mater. Interfaces 13 (2021) 33226–33236. https://doi.org/10.1021/acsami.1c05254.

[121] J. Fan, X. Huang, F. Liu, L. Deng, G. Chen, Feasibility of using chemically exfoliated SnSe nanobelts in constructing flexible SWCNTs-based composite films for high-performance thermoelectric applications, Compos. Commun. 24 (2021) 100612. https://doi.org/10.1016/j.coco.2020.100612.

[122] H.W. Jeong, H. Wu, G.F. Samu, P. Rouster, I. Szilágyi, H. Park, C. Janáky, The effect of nanostructure dimensionality on the photoelectrochemical properties of derived TiO_2 films, Electrochim. Acta 373 (2021) 137900. https://doi.org/10.1016/j.electacta.2021.137900.

[123] Z. Li, H. Qiao, Z. Guo, X. Ren, Z. Huang, X. Qi, S.C. Dhanabalan, J.S. Ponraj, D. Zhang, J. Li, J. Zhao, J. Zhong, H. Zhang, High-Performance Photo-Electrochemical Photodetector Based on Liquid-Exfoliated Few-Layered InSe Nanosheets with Enhanced Stability, Adv. Funct. Mater. 28 (2018) 1705237. https://doi.org/10.1002/adfm.201705237.

[124] D.G. Hopkinson, V. Zólyomi, A.P. Rooney, N. Clark, D.J. Terry, M. Hamer, D.J. Lewis, C.S. Allen, A.I. Kirkland, Y. Andreev, Z. Kudrynskyi, Z. Kovalyuk, A. Patanè, V.I. Fal'Ko, R. Gorbachev, S.J. Haigh, Formation and Healing of Defects in Atomically Thin GaSe and InSe, ACS Nano 13 (2019) 5112–5123. https://doi.org/10.1021/acsnano.8b08253.

[125] S.L. Li, K. Tsukagoshi, E. Orgiu, P. Samorì, Charge transport and mobility engineering in two-dimensional transition metal chalcogenide semiconductors, Chem. Soc. Rev. 45 (2016) 118–151. https://doi.org/10.1039/c5cs00517e.

[126] H. Wang, M.L. Chen, M. Zhu, Y. Wang, B. Dong, X. Sun, X. Zhang, S. Cao, X. Li, J. Huang, L. Zhang, W. Liu, D. Sun, Y. Ye, K. Song, J. Wang, Y. Han, T. Yang, H. Guo, C. Qin, L. Xiao, J. Zhang, J. Chen, Z. Han, Z. Zhang, Gate tunable giant anisotropic resistance in ultra-thin GaTe, Nat. Commun. 10 (2019) 2302. https://doi.org/10.1038/s41467-019-10256-3.

[127] J. Kang, V.K. Sangwan, H.S. Lee, X. Liu, M.C. Hersam, Solution-Processed Layered Gallium Telluride Thin-Film Photodetectors, ACS Photonics 5 (2018) 3996–4002. https://doi.org/10.1021/acsphotonics.8b01066.

[128] D.N. Bose, S. Pal, Photoconductivity, low-temperature conductivity, and magnetoresistance studies on the layered semiconductor GaTe, Phys. Rev. B - Condens. Matter Mater. Phys. 63 (2001) 235321. https://doi.org/10.1103/PhysRevB.63.235321.

[129] J. Camassel, P. Merle, H. Mathieu, A. Gouskov, Near-band-edge optical properties of $GaSe_xTe_{1-x}$ mixed crystals, Phys. Rev. B 19 (1979) 1060. https://doi.org/10.1103/PhysRevB.19.1060.

[130] L.C. Tien, Y.C. Shih, C.Y. Chen, Y.T. Huang, R.S. Chen, Broadband photodetectors based on layered 1D GaTe nanowires and 2D GaTe nanosheets, J. Alloys Compd. 876 (2021) 160195. https://doi.org/10.1016/j.jallcom.2021.160195.

[131] Y. Liu, X. Wu, W. Guo, M. Li, C. Xiao, T. Ou, J. Yao, Y. Yu, Y. Zheng, Y. Wang, Enhanced performance of a n-Si/p-GaTe heterojunction through interfacial passivation and thermal oxidation, J. Mater. Chem. C 10 (2022) 11747–11754. https://doi.org/10.1039/d2tc02740b.

[132] C.C. Carlo, P.H. Wu, D.P. Hasibuan, C.S. Saragih, H. Giap, D.H. Nguyen, Y.R. Chen, R.A. Patil, D. Van Pham, J.L. Shen, C.C. Lai, M.K. Wu, Y.R. Ma, Efficient van der Waals layered gallium telluride-based passive photodetectors for low-power-density sensing of visible light, J. Mater. Chem. C 11 (2023) 14316–14325. https://doi.org/10.1039/d3tc01958f.

[133] Z. Wang, K. Xu, Y. Li, X. Zhan, M. Safdar, Q. Wang, F. Wang, J. He, Role of Ga vacancy on a multilayer GaTe phototransistor, ACS Nano 8 (2014) 4859–4865. https://doi.org/10.1021/nn500782n.

[134] S. Siddique, C.C. Gowda, R. Tromer, S. Demiss, A.R.S. Gautam, O.E. Femi, P. Kumbhakar, D.S. Galvao, A. Chandra, C.S. Tiwary, Scalable Synthesis of Atomically Thin Gallium Telluride Nanosheets for Supercapacitor Applications, ACS Appl. Nano Mater. 4 (2021) 4829–4838. https://doi.org/10.1021/acsanm.1c00428.

[135] Z. Chen, S. Chu, J. Chen, H. Chen, J. Zhang, X. Ma, Q. Li, X. Chen, Epitaxially grown semi-vertical and aligned GaTe two dimensional sheets on ZnO substrate for energy harvesting applications, Nano Energy 56 (2019) 294–299. https://doi.org/10.1016/j.nanoen.2018.11.015.

[136] L.C. Tien, Y.C. Shih, Morphology-controlled vapor phase growth and characterization of one-dimensional GaTe nanowires and two-dimensional nanosheets for potential visible-light active photocatalysts, Nanomaterials 11 (2021) 778. https://doi.org/10.3390/nano11030778.

[137] H.L. Zhuang, R.G. Hennig, Single-layer group-III monochalcogenide photocatalysts for water splitting, Chem. Mater. 25 (2013) 3232–3238. https://doi.org/10.1021/cm401661x.

[138] U.S. Shenoy, U. Gupta, D.S. Narang, D.J. Late, U. V Waghmare, C.N.R. Rao, Electronic structure and properties of layered gallium telluride, Chem. Phys. Lett. 651 (2016) 148–154. https://doi.org/10.1016/j.cplett.2016.03.045.

[139] Y. Fan, X. Ma, X. Liu, J. Wang, H. Ai, M. Zhao, Theoretical Design of an InSe/GaTe vdW Heterobilayer: A Potential Visible-Light Photocatalyst for Water Splitting, J. Phys. Chem. C 122 (2018) 27803–27810. https://doi.org/10.1021/acs.jpcc.8b07692.

[140] Q. Li, X. Ma, H. Liu, Z. Chen, H. Chen, S. Chu, Self-Organized Growth of Two-Dimensional GaTe Nanosheet on ZnO Nanowires for Heterojunctional Water Splitting Applications, ACS Appl. Mater. Interfaces 9 (2017) 18836–18844. https://doi.org/10.1021/acsami.7b04199.

[141] Z. Wang, M. Safdar, M. Mirza, K. Xu, Q. Wang, Y. Huang, F. Wang, X. Zhan, J. He, High-performance flexible photodetectors based on GaTe nanosheets, Nanoscale 7 (2015) 7252–7258. https://doi.org/10.1039/c4nr07313d.

[142] K. Lai, S. Ju, H. Zhu, H. Wang, H. Wu, B. Yang, E. Zhang, M. Yang, F. Li, S. Cui, X. Deng, Z. Han, M. Zhu, J. Dai, Strong bulk-surface interaction dominated in-plane anisotropy of electronic structure in GaTe, Commun. Phys. 5 (2022) 143. https://doi.org/10.1038/s42005-022-00923-1.

[143] N.T. Hoang, J.H. Lee, T.H. Vu, S. Cho, M.J. Seong, Thickness-dependent in-plane anisotropy of GaTe phonons, Sci. Rep. 11 (2021) 21202. https://doi.org/10.1038/s41598-021-00673-0.

[144] F. Bondino, S. Duman, S. Nappini, G. D'Olimpio, C. Ghica, T.O. Menteş, F. Mazzola, M.C. Istrate, M. Jugovac, M. Vorokhta, S. Santoro, B. Gürbulak, A. Locatelli, D.W. Boukhvalov, A. Politano, Improving the Efficiency of Gallium Telluride for Photocatalysis, Electrocatalysis, and Chemical Sensing through Defects Engineering and Interfacing with its Native Oxide, Adv. Funct. Mater. 32 (2022) 2205923. https://doi.org/10.1002/adfm.202205923.

[145] Q. Zhao, T. Wang, Y. Miao, F. Ma, Y. Xie, X. Ma, Y. Gu, J. Li, J. He, B. Chen, S. Xi, L. Xu, H. Zhen, Z. Yin, J. Li, J. Ren, W. Jie, Thickness-induced structural phase transformation of layered gallium telluride, Phys. Chem. Chem. Phys. 18 (2016) 18719–18726. https://doi.org/10.1039/c6cp01963c.

[146] B. Mortazavi, F. Shojaei, M. Azizi, T. Rabczuk, X. Zhuang, As_2S_3, As_2Se_3 and As_2Te_3 nanosheets: Superstretchable semiconductors with anisotropic carrier mobilities and optical properties, J. Mater. Chem. C 8 (2020) 2400–2410. https://doi.org/10.1039/c9tc05904k.

[147] J. Lin, H. Yang, J. Zhang, S. Yang, G. Lu, Y. Zhang, H. Qin, J. Xi, L. Song, Surface restructuring $Ni_{0.85}Se$/ZnSe catalyst shows large boosting electrocatalytic and photoelectrochemical performance, Ceram. Int. 50 (2024) 6713–6724. https://doi.org/10.1016/j.ceramint.2023.12.010.

[148] A.F. Shaikh, S.S. Arbuj, M.S. Tamboli, S.D. Naik, S.B. Rane, B.B. Kale, ZnSe/ZnO Nano-Heterostructures for Enhanced Solar Light Hydrogen Generation, ChemistrySelect 2 (2017) 9174–9180. https://doi.org/10.1002/slct.201701618.

[149] H. Kaneko, T. Minegishi, M. Nakabayashi, N. Shibata, Y. Kuang, T. Yamada, K. Domen, A Novel Photocathode Material for Sunlight-Driven Overall Water Splitting: Solid Solution of ZnSe and Cu(In,Ga)Se_2, Adv. Funct. Mater. 26 (2016) 4570–4577. https://doi.org/10.1002/adfm.201600615.

[150] X. Xiong, M. Forster, J.D. Major, Y. Xu, A.J. Cowan, Time-Resolved Spectroscopy of ZnTe Photocathodes for Solar Fuel Production, J. Phys. Chem. C 121 (2017) 22073–22080. https://doi.org/10.1021/acs.jpcc.7b06304.

[151] J.W. Jang, S. Cho, G. Magesh, Y.J. Jang, J.Y. Kim, W.Y. Kim, J.K. Seo, S. Kim, K.H. Lee, J.S. Lee, Aqueous-solution route to zinc telluride films for application to CO_2 reduction, Angew. Chemie - Int. Ed. 53 (2014) 5852–5857. https://doi.org/10.1002/anie.201310461.

[152] Y. Zhang, Y. Huang, S.S. Zhu, Y.Y. Liu, X. Zhang, J.J. Wang, A. Braun, Covalent S-O Bonding Enables Enhanced Photoelectrochemical Performance of Cu_2S/Fe_2O_3 Heterojunction for Water Splitting, Small 17 (2021) 2100320. https://doi.org/10.1002/smll.202100320.

[153] G. Wang, Y. Quan, K. Yang, Z. Jin, EDA-assisted synthesis of multifunctional snowflake-Cu_2S/CdZnS S-scheme heterojunction for improved the photocatalytic hydrogen evolution, J. Mater. Sci. Technol. 121 (2022) 28–39. https://doi.org/10.1016/j.jmst.2021.11.073.

[154] T.H. Lai, C.W. Tsao, M.J. Fang, J.Y. Wu, Y.P. Chang, Y.H. Chiu, P.Y. Hsieh, M.Y. Kuo, K. Der Chang, Y.J. Hsu, Au@Cu_2O Core−Shell and Au@Cu_2Se Yolk−Shell Nanocrystals as Promising Photocatalysts in Photoelectrochemical Water Splitting and Photocatalytic Hydrogen Production, ACS Appl. Mater. Interfaces 14 (2022) 40771–40783. https://doi.org/10.1021/acsami.2c07145.

[155] A. V. Shaikh, S.G. Sayyed, S. Naeem, S.F. Shaikh, R.S. Mane, Electrodeposition of n-CdSe/p-Cu_2Se heterojunction solar cells, Eng. Sci. 13 (2021) 79–86. https://doi.org/10.30919/es8d1124.

[156] S. Li, Z. Zhao, J. Li, H. Liu, M. Liu, Y. Zhang, L. Su, A.I. Pérez-Jiménez, Y. Guo, F. Yang, Y. Liu, J. Zhao, J. Zhang, L. Zhao, Y. Lin, Mechanically Induced Highly Efficient Hydrogen Evolution from Water over Piezoelectric SnSe nanosheets, Small 18 (2022) 2202507. https://doi.org/10.1002/SMLL.202202507.

[157] T.K. Chang, Y.S. Huang, H.Y. Chen, C.N. Liao, Photoelectrochemical Enhancement of Cu_2O by a Cu_2Te Hole Transmission Interlayer, ACS Appl. Mater. Interfaces 14 (2022) 48540–48546. https://doi.org/10.1021/acsami.2c10448.

[158] P. Mandal, B. Show, S.T. Ahmed, D. Banerjee, A. Mondal, Visible-light active electrochemically deposited tin selenide thin films: synthesis, characterization and photocatalytic activity, J. Mater. Sci. Mater. Electron. 31 (2020) 4708–4718. https://doi.org/10.1007/s10854-020-03027-0.

[159] H. Zhao, C. Wang, G. Liu, D. Barba, F. Vidal, G. Han, F. Rosei, Efficient and stable hydrogen evolution based on earth-abundant SnSe nanocrystals, Appl. Catal. B Environ. 264 (2020) 118526. https://doi.org/10.1016/j.apcatb.2019.118526.

[160] H.S. Im, Y. Myung, Y.J. Cho, C.H. Kim, H.S. Kim, S.H. Back, C.S. Jung, D.M. Jang, Y.R. Lim, J. Park, J.P. Ahn, Facile phase and composition tuned synthesis of tin chalcogenide nanocrystals, RSC Adv. 3 (2013) 10349–10354. https://doi.org/10.1039/c3ra40869h.

[161] H. Cai, J. Kang, H. Sahin, B. Chen, A. Suslu, K. Wu, F. Peeters, X. Meng, S. Tongay, Exciton pumping across type-I gallium chalcogenide heterojunctions, Nanotechnology 27 (2016) 065203. https://doi.org/10.1088/0957-4484/27/6/065203.

[162] X. Fan, L. Su, F. Zhang, D. Huang, D.K. Sang, Y. Chen, Y. Li, F. Liu, J. Li, H. Zhang, H. Xie, Layer-Dependent Properties of Ultrathin GeS Nanosheets and Application in UV-Vis Photodetectors, ACS Appl. Mater. Interfaces 11 (2019) 47197–47206. https://doi.org/10.1021/acsami.9b14663.

[163] X. Lv, W. Wei, Q. Sun, F. Li, B. Huang, Y. Dai, Two-dimensional germanium monochalcogenides for photocatalytic water splitting with high carrier mobility, Appl. Catal. B Environ. 217 (2017) 275–284. https://doi.org/10.1016/j.apcatb.2017.05.087.

[164] R.K. Ulaganathan, Y.Y. Lu, C.J. Kuo, S.R. Tamalampudi, R. Sankar, K.M. Boopathi, A. Anand, K. Yadav, R.J. Mathew, C.R. Liu, F.C. Chou, Y.T. Chen, High photosensitivity and broad spectral response of multi-layered germanium sulfide transistors, Nanoscale 8 (2016) 2284–2292. https://doi.org/10.1039/c5nr05988g.

[165] Z. Huang, K. Ren, R. Zheng, L. Wang, L. Wang, Ultrahigh Carrier Mobility in Two-Dimensional IV–VI Semiconductors for Photocatalytic Water Splitting, Molecules 28 (2023) 4126. https://doi.org/10.3390/molecules28104126.

[166] D. Tan, W. Zhang, X. Wang, S. Koirala, Y. Miyauchi, K. Matsuda, Polarization-sensitive and broadband germanium sulfide photodetectors with excellent high-temperature performance, Nanoscale 9 (2017) 12425–12431. https://doi.org/10.1039/c7nr03040a.

[167] D. Gu, X. Tao, H. Chen, Y. Ouyang, W. Zhu, Y. Du, Two-dimensional polarized $MoTe_2$/GeS heterojunction with an intrinsic electric field for photocatalytic water-splitting, RSC Adv. 11 (2021) 34048–34058. https://doi.org/10.1039/d1ra05840a.

[168] S.M. Tan, C.K. Chua, D. Sedmidubský, Z. Sofer, M. Pumera, Electrochemistry of layered GaSe and GeS: Applications to ORR, OER and HER, Phys. Chem. Chem. Phys. 18 (2016) 1699–1711. https://doi.org/10.1039/c5cp06682d.

[169] A.S. Sarkar, E. Stratakis, Dispersion behaviour of two dimensional monochalcogenides, J. Colloid Interface Sci. 594 (2021) 334–341. https://doi.org/10.1016/j.jcis.2021.02.081.

[170] D. Tan, H.E. Lim, F. Wang, N.B. Mohamed, S. Mouri, W. Zhang, Y. Miyauchi, M. Ohfuchi, K. Matsuda, Anisotropic optical and electronic properties of two-dimensional layered germanium sulfide, Nano Res. 10 (2017) 546–555. https://doi.org/10.1007/s12274-016-1312-6.

[171] X. Liu, B. Lv, Z. Ding, Z. Luo, External uniaxial compressive strain induced built-in electric field in bilayer two-dimensional As_2S_3 for photocatalytic water splitting: A first-principles study, Appl. Surf. Sci. 535 (2021) 147701. https://doi.org/10.1016/j.apsusc.2020.147701.

[172] D.F. Blossey, Iodine Quenching of the Surface Photoresponse of Crystalline As_2S_3, Chem. Phys. Lett. 25 (1974) 593–595. https://doi.org/10.1016/0009-2614(74)85376-5.

[173] D. F. Blossey, R. Zallen, Surface and bulk photoresponse of crystalline As_2S_3, Phys. Rev. B 9 (1974) 4306–4313. https://doi.org/10.1103/PhysRevB.9.4306.

[174] E. Ozakın, Rumeysa Can, F. Kaya, N. Acar, A. Cevik, Arsenic Poisoning Due to the Intake of Orpiment, J. Clin. Toxicol. 3 (2014) 1000176. https://doi.org/10.4172/2161-0495.1000176.

[175] P. Li, T. He, Recent advances in zinc chalcogenide-based nanocatalysts for photocatalytic reduction of CO_2, J. Mater. Chem. A 9 (2021) 23364. https://doi.org/10.1039/d1ta05365e.

[176] J. Liu, S. Yue, H. Zhang, C. Wang, D. Barba, F. Vidal, S. Sun, Z.M. Wang, J. Bao, H. Zhao, G.S. Selopal, F. Rosei, Efficient Photoelectrochemical Hydrogen Generation Using Eco-Friendly "giant" InP/ZnSe Core/Shell Quantum Dots, ACS Appl. Mater. Interfaces 15 (2023) 34797–34808. https://doi.org/10.1021/acsami.3c04900.

[177] Y. Chen, L. Wang, W. Wang, M. Cao, Enhanced photoelectrochemical properties of ZnO/ZnSe/CdSe/Cu_{2-x}Se core–shell nanowire arrays fabricated by ion-replacement method, Appl. Catal. B Environ. 209 (2017) 110–117. https://doi.org/10.1016/j.apcatb.2017.02.049.

[178] M.F. Kuehnel, C.E. Creissen, C.D. Sahm, D. Wielend, A. Schlosser, K.L. Orchard, E. Reisner, ZnSe Nanorods as Visible-Light Absorbers for Photocatalytic and Photoelectrochemical H_2 Evolution in Water, Angew. Chemie - Int. Ed. 58 (2019) 5059–5063. https://doi.org/10.1002/anie.201814265.

[179] Y. Zhong, M. Li, X. Luan, F. Gao, H. Wu, J. Zi, Z. Lian, Ultrathin $ZnIn_2S_4$/ZnSe heteronanosheets with modulated S-scheme enable high efficiency of visible-light-responsive photocatalytic hydrogen evolution, Appl. Catal. B Environ. 335 (2023) 122859. https://doi.org/10.1016/j.apcatb.2023.122859.

[180] J. Wang, X. Yang, J. Cao, Y. Wang, Q. Li, Computational study of the electronic, optical and photocatalytic properties of single-layer hexagonal zinc chalcogenides, Comput. Mater. Sci. 150 (2018) 432–438. https://doi.org/10.1016/j.commatsci.2018.04.049.

[181] J.O. Bockris, K. Uosaki, The Rate of the Photoelectrochemical Generation of Hydrogen at p-Type Semiconductors, J. Electrochem. Soc. 124 (1977) 1348–1355. https://doi.org/10.1149/1.2133652.

[182] Z.G. Yu, C.E. Pryor, W.H. Lau, M.A. Berding, D.B. MacQueen, Core-shell nanorods for efficient photoelectrochemical hydrogen production, MRS Online Proceedings Library 885 (2005) 1103. https://doi.org/10.1557/proc-0885-a11-03.

[183] D.H. Won, J. Chung, S.H. Park, E.H. Kim, S.I. Woo, Photoelectrochemical production of useful fuels from carbon dioxide on a polypyrrole-coated p-ZnTe photocathode under visible light irradiation, J. Mater. Chem. A 3 (2015) 1089–1095. https://doi.org/10.1039/c4ta05901h.

[184] W. Zhang, Y. Hu, C. Yan, D. Hong, R. Chen, X. Xue, S. Yang, Y. Tian, Z. Tie, Z. Jin, Surface plasmon resonance enhanced direct Z-scheme TiO_2/ZnTe/Au nanocorncob heterojunctions for efficient photocatalytic overall water splitting, Nanoscale 11 (2019) 9053–9060. https://doi.org/10.1039/c9nr01732a.

[185] Z. Wang, Y. Wang, S. Ning, Q. Kang, Zinc-Based Materials for Photoelectrochemical Reduction of Carbon Dioxide, Energy and Fuels 36 (2022) 11380–11393. https://doi.org/10.1021/acs.energyfuels.2c01350.

[186] T. Minegishi, A. Ohnishi, Y. Pihosh, K. Hatagami, T. Higashi, M. Katayama, K. Domen, M. Sugiyama, ZnTe-based photocathode for hydrogen evolution from water under sunlight, APL Mater. 8 (2020) 041101. https://doi.org/10.1063/5.0002621.

[187] Y. Wei, Y. Zhu, P. Li, X. Gao, Z. Yu, S. Liu, N. Li, Y. Shen, M. Wang, Surface states modulation of ZnTe via ultrathin ZnO layer as efficient photocathodes for CO_2 reduction reaction, Appl. Catal. B Environ. 347 (2024) 123760. https://doi.org/10.1016/j.apcatb.2024.123760.

[188] P. Wen, H. Li, X. Ma, R. Lei, X. Wang, S.M. Geyer, Y. Qiu, A colloidal ZnTe quantum dot-based photocathode with a metal-insulator-semiconductor structure towards solar-driven CO_2 reduction to tunable syngas, J. Mater. Chem. A 9 (2021) 3589–3596. https://doi.org/10.1039/d0ta10394b.

[189] V. Navakoteswara Rao, N. Lakshmana Reddy, M. Mamatha Kumari, P. Ravi, M. Sathish, K.M. Kuruvilla, V. Preethi, K.R. Reddy, N.P. Shetti, T.M. Aminabhavi, M. V. Shankar, Photocatalytic recovery of H_2 from H_2S containing wastewater: Surface and interface control of photo-excitons in $Cu_2S@TiO_2$ core-shell nanostructures, Appl. Catal. B Environ. 254 (2019) 174–185. https://doi.org/10.1016/j.apcatb.2019.04.090.

[190] Q. Cao, R. Che, N. Chen, Scalable synthesis of Cu_2S double-superlattice nanoparticle systems with enhanced UV/visible-light-driven photocatalytic activity, Appl. Catal. B Environ. 162 (2015) 187–195. https://doi.org/10.1016/j.apcatb.2014.06.052.

[191] Z. Du, J. Tong, W. Guo, H. Zhang, X. Zhong, Cuprous sulfide on Ni foam as a counter electrode for flexible quantum dot sensitized solar cells, J. Mater. Chem. A 4 (2016) 11754–11761. https://doi.org/10.1039/c6ta04934f.

[192] I. Minguez-Bacho, M. Courté, H.J. Fan, D. Fichou, Conformal Cu_2S-coated Cu_2O nanostructures grown by ion exchange reaction and their photoelectrochemical properties, Nanotechnology 26 (2015) 185401. https://doi.org/10.1088/0957-4484/26/18/185401.

[193] J. Henry, T. Daniel, V. Balasubramanian, K. Mohanraj, G. Sivakumar, Temperature dependent electrical and optical properties with higher photosensitivity of Cu_2Se absorber thin films for photo voltaic application, Inorg. Nano-Metal Chem. 51 (2021) 38–46. https://doi.org/10.1080/24701556.2020.1751199.

[194] J. Henry, T. Daniel, V. Balasubramanian, K. Mohanraj, G. Sivakumar, Enhanced Photosensitivity of Bi-Doped Cu_2Se Thin Films Prepared by Chemical Synthesis for Solar Cell Application, Iran. J. Sci. Technol. Trans. A Sci. 44 (2020) 1369–1377. https://doi.org/10.1007/s40995-020-00949-6.

[195] H. Komal, M. Sohail, A. Nafady, K. Ken, G. Will, A. Wahab, A.P.O. Mullane, S-doped copper selenide thin films synthesized by chemical bath deposition for photoelectrochemical water splitting, Appl. Surf. Sci. 641 (2023) 158505. https://doi.org/10.1016/j.apsusc.2023.158505.

[196] Y. Zhang, L. Hu, Y. Zhang, X. Wang, H. Wang, Snowflake-Like Cu_2S/MoS_2/Pt heterostructure with near infrared photothermal-enhanced electrocatalytic and photoelectrocatalytic hydrogen production, Appl. Catal. B Environ. 315 (2022) 121540. https://doi.org/10.1016/j.apcatb.2022.121540.

[197] P. Kumar, K. Singh, O.N. Srivastava, Template free-solvothermaly synthesized copper selenide (CuSe, $Cu_{2-x}Se$, β-Cu_2Se and Cu_2Se) hexagonal nanoplates from different precursors at low temperature, J. Cryst. Growth 312 (2010) 2804–2813. https://doi.org/10.1016/j.jcrysgro.2010.06.014.

[198] K. Liu, H. Liu, J. Wang, L. Shi, Synthesis and characterization of Cu_2Se prepared by hydrothermal co-reduction, J. Alloys Compd. 484 (2009) 674–676. https://doi.org/10.1016/j.jallcom.2009.05.014.

[199] C. Han, Y. Bai, Q. Sun, S. Zhang, Z. Li, L. Wang, S. Dou, Ambient aqueous growth of Cu_2Te nanostructures with excellent electrocatalytic activity toward sulfide redox shuttles, Adv. Sci. 3 (2015) 1500350. https://doi.org/10.1002/advs.201500350.

[200] Q. Ba, P.S. Tóth, C. Hajdu, C. Janáky, Photoelectrochemical behavior of GaTe nanoflakes prepared by exfoliation, Electrochim. Acta 507 (2024) 145105. https://doi.org/10.1016/j.electacta.2024.145105.

[201] I.D. Baikie, A.C. Grain, J. Sutherland, J. Law, Ambient pressure photoemission spectroscopy of metal surfaces, Appl. Surf. Sci. 323 (2014) 45–53. https://doi.org/10.1016/j.apsusc.2014.08.159.

[202] L.M. Peter, E.A. Ponomarev, D.J. Fermín, Intensity-modulated photocurrent spectroscopy: Reconciliation of phenomenological analysis with multistep electron transfer mechanisms, J. Electroanal. Chem. 427 (1997) 79–96. https://doi.org/10.1016/S0022-0728(96)05033-4.

[203] M. Rodríguez-Pérez, I. Rodríguez-Gutiérrez, A. Vega-Poot, R. García-Rodríguez, G. Rodríguez-Gattorno, G. Oskam, Charge transfer and recombination kinetics at WO_3 for photoelectrochemical water oxidation, Electrochim. Acta 258 (2017) 900–908. https://doi.org/10.1016/j.electacta.2017.11.140.

[204] G.R. Neupane, M. Bamidele, V. Yeddu, D.Y. Kim, P. Hari, Negative capacitance and hysteresis in encapsulated $MAPbI_3$ and lead–tin (Pb–Sn) perovskite solar cells, J. Mater. Res. 37 (2022) 1357–1372. https://doi.org/10.1557/s43578-022-00540-2.

[205] Z. Cheng, S. Redner, Scaling theory of fragmentation, Phys. Rev. Lett. 60 (1988) 2450. https://doi.org/10.1103/PhysRevLett.60.2450.

[206] K. Kouroupis-Agalou, A. Liscio, E. Treossi, L. Ortolani, V. Morandi, N.M. Pugno, V. Palermo, Fragmentation and exfoliation of 2-dimensional materials: A statistical approach, Nanoscale 6 (2014) 5926–5933. https://doi.org/10.1039/c3nr06919b.

[207] S. Zhao, H. Wang, Y. Zhou, L. Liao, Y. Jiang, X. Yang, G. Chen, M. Lin, Y. Wang, H. Peng, Z. Liu, Controlled synthesis of single-crystal SnSe nanoplates, Nano Res. 8 (2015) 288–295. https://doi.org/10.1007/s12274-014-0676-8.

[208] C. Gurnani, S.L. Hawken, A.L. Hector, R. Huang, M. Jura, W. Levason, J. Perkins, G. Reid, G.B.G. Stenning, Tin(iv) chalcogenoether complexes as single source precursors for the chemical vapour deposition of SnE_2 and SnE (E = S, Se) thin films, Dalt. Trans. 47 (2018) 2628–2637. https://doi.org/10.1039/c7dt03848h.

[209] Z. Tian, M. Zhao, X. Xue, W. Xia, C. Guo, Y. Guo, Y. Feng, J. Xue, Lateral Heterostructures Formed by Thermally Converting n-Type $SnSe_2$ to p-Type SnSe, ACS Appl. Mater. Interfaces 10 (2018) 12831–12838. https://doi.org/10.1021/acsami.8b01235.

[210] M. Kumar, S. Rani, Y. Singh, K.S. Gour, V.N. Singh, Tin-selenide as a futuristic material: properties and applications, RSC Adv. 11 (2021) 6477–6503. https://doi.org/10.1039/d0ra09807h.

[211] D. Martínez-Escobar, M. Ramachandran, A. Sánchez-Juárez, J.S. Narro Rios, Optical and electrical properties of $SnSe_2$ and SnSe thin films prepared by spray pyrolysis, Thin Solid Films 535 (2013) 390–393. https://doi.org/10.1016/j.tsf.2012.12.081.

[212] S. Saha, A. Banik, K. Biswas, Few-Layer Nanosheets of n-Type $SnSe_2$, Chem. – A Eur. J. 22 (2016) 15634–15638. https://doi.org/10.1002/chem.201604161.

[213] Z. Wang, C. Fan, Z. Shen, C. Hua, Q. Hu, F. Sheng, Y. Lu, H. Fang, Z. Qiu, J. Lu, Z. Liu, W. Liu, Y. Huang, Z.A. Xu, D.W. Shen, Y. Zheng, Defects controlled hole doping and multivalley transport in SnSe single crystals, Nat. Commun. 9 (2018) 47. https://doi.org/10.1038/s41467-017-02566-1.

[214] W. Albers, J. Verberkt, The SnSe-$SnSe_2$ Eutectic; a P-N multilayer structure, J. Mater. Sci. 5 (1970) 24–28. https://doi.org/10.1007/bf02427180.

[215] J. Kibsgaard, Z. Chen, B.N. Reinecke, T.F. Jaramillo, Engineering the surface structure of MoS_2 to Â preferentially expose active edge sites for Â electrocatalysis, Nat. Mater. 11 (2012) 963–969. https://doi.org/10.1038/nmat3439.

[216] B. Qin, Y. Zhang, D. Wang, Q. Zhao, B. Gu, H. Wu, H. Zhang, B. Ye, S.J. Pennycook, L.D. Zhao, Ultrahigh Average ZT Realized in p-Type SnSe Crystalline Thermoelectrics through Producing Extrinsic Vacancies, J. Am. Chem. Soc. 142 (2020) 5901–5909. https://doi.org/10.1021/jacs.0c01726.

[217] M. Kumar, P. Sharma, S. Rani, M. Kumar, V.N. Singh, Ultrafast excited-state dynamics of $SnSe_2$-SnSe composite thin film, AIP Adv. 11 (2021) 025040. https://doi.org/10.1063/5.0038269.

[218] U. Halim, C.R. Zheng, Y. Chen, Z. Lin, S. Jiang, R. Cheng, Y. Huang, X. Duan, A rational design of cosolvent exfoliation of layered materials by directly probing liquid-solid interaction, Nat. Commun. 4 (2013) 2213. https://doi.org/10.1038/ncomms3213.

[219] A.K. Deb, V. Kumar, Bandgap engineering in semiconducting one to few layers of SnS and SnSe, Phys. Status Solidi B (2016) 1–8. https://doi.org/10.1002/pssb.201600379.

[220] X. Yu, N. Guijarro, M. Johnson, K. Sivula, Defect Mitigation of Solution-Processed 2D WSe_2 Nanoflakes for Solar-to-Hydrogen Conversion, Nano Lett. 18 (2018) 215–222. https://doi.org/10.1021/acs.nanolett.7b03948.

[221] L. Peter, Photoelectrochemical Kinetics: Hydrogen Evolution on p-Type Semiconductors, J. Electrochem. Soc. 166 (2019) H3125–H3132. https://doi.org/10.1149/2.0231905jes.

[222] J.E. Thorne, Y. Zhao, D. He, S. Fan, S. Vanka, Z. Mi, D. Wang, Understanding the role of co-catalysts on silicon photocathodes using intensity modulated photocurrent spectroscopy, Phys. Chem. Chem. Phys. 19 (2017) 29653–29659. https://doi.org/10.1039/c7cp06533g.

[223] E.A. Ponomarev, L.M. Peter, A comparison of intensity modulated photocurrent spectroscopy and photoelectrochemical impedance spectroscopy in a study of photoelectrochemical hydrogen evolution at p-InP, J. Electroanal. Chem. 397 (1995) 45–52. https://doi.org/10.1016/0022-0728(95)04148-9.

[224] C. Zachäus, F.F. Abdi, L.M. Peter, R. Van De Krol, Photocurrent of $BiVO_4$ is limited by surface recombination, not surface catalysis, Chem. Sci. 8 (2017) 3712–3719. https://doi.org/10.1039/c7sc00363c.

[225] D.K. Zhong, S. Choi, D.R. Gamelin, Near-complete suppression of surface recombination in solar photoelectrolysis by "co-Pi" catalyst-modified W:$BiVO_4$, J. Am. Chem. Soc. 133 (2011) 18370–18377. https://doi.org/10.1021/ja207348x.

[226] P. Hu, J. Zhang, M. Yoon, X.F. Qiao, X. Zhang, W. Feng, P. Tan, W. Zheng, J. Liu, X. Wang, J.C. Idrobo, D.B. Geohegan, K. Xiao, Highly sensitive phototransistors based on two-dimensional GaTe nanosheets with direct bandgap, Nano Res. 7 (2014) 694–703. https://doi.org/10.1007/s12274-014-0430-2.

[227] M. Abdel Rahman, A.E. Belal, Single crystal growth and optical energy gap of gallium telluride, J. Phys. Chem. Solids 61 (2000) 925–929. https://doi.org/10.1016/S0022-3697(99)00391-1.

[228] S. Huang, Y. Tatsumi, X. Ling, H. Guo, Z. Wang, G. Watson, A.A. Puretzky, D.B. Geohegan, J. Kong, J. Li, T. Yang, R. Saito, M.S. Dresselhaus, In-Plane Optical Anisotropy of Layered Gallium Telluride, ACS Nano 10 (2016) 8964–8972. https://doi.org/10.1021/acsnano.6b05002.

[229] L.C. Muhimmah, C.H. Ho, Dual phase two-color emission observed in van der Waals GaTe planes, Appl. Surf. Sci. 542 (2021) 148593. https://doi.org/10.1016/j.apsusc.2020.148593.

[230] P. Cataldi, I.S. Bayer, F. Bonaccorso, V. Pellegrini, A. Athanassiou, R. Cingolani, Foldable Conductive Cellulose Fiber Networks Modified by Graphene Nanoplatelet-Bio-Based Composites, Adv. Electron. Mater. 1 (2015) 1500224. https://doi.org/10.1002/aelm.201500224.

[231] M.I. Zappia, G. Bianca, S. Bellani, M. Serri, L. Najafi, R. Oropesa-Nuñez, B. Martín-García, D. Bouša, D. Sedmidubský, V. Pellegrini, Z. Sofer, A. Cupolillo, F. Bonaccorso, Solution-Processed GaSe Nanoflake-Based Films for Photoelectrochemical Water Splitting and Photoelectrochemical-Type Photodetectors, Adv. Funct. Mater. 30 (2020) 1909572. https://doi.org/10.1002/adfm.201909572.

[232] Z. Lin, Y. Liu, U. Halim, M. Ding, Y. Liu, Y. Wang, C. Jia, P. Chen, X. Duan, C. Wang, F. Song, M. Li, C. Wan, Y. Huang, X. Duan, Solution-processable 2D semiconductors for high-performance large-area electronics, Nature 562 (2018) 254–258. https://doi.org/10.1038/s41586-018-0574-4.

[233] T. Carey, O. Cassidy, K. Synnatschke, E. Caffrey, J. Garcia, S. Liu, H. Kaur, A.G. Kelly, J. Munuera, C. Gabbett, D. O'Suilleabhain, J.N. Coleman, High-Mobility Flexible Transistors with Low-Temperature Solution-Processed Tungsten Dichalcogenides, ACS Nano 17 (2023) 2912–2922. https://doi.org/10.1021/acsnano.2c11319.

[234] M.M. Perera, M. Lin, H. Chuang, B.P. Chamlagain, C. Wang, X. Tan, M.M. Cheng, D. Toma, Z. Zhou, Improved Carrier Mobility in Few-Layer MoS_2 Field-Effect Transistors with Ionic-Liquid Gating, ACS Nano 7 (2013) 4449–4458. https://doi.org/10.1021/nn401053g.

[235] R. Biswas, Modeling the liquid phase exfoliation of graphene in polar and nonpolar solvents, Biointerface Res. Appl. Chem. 12 (2022) 7404–7415. https://doi.org/10.33263/BRIAC126.74047415.

[236] L. Zhang, X. Li, K. Chen, Z. Zhang, Y. Li, Y. Lu, X. Chen, D. Yang, C. Shan, Revealing the Anisotropic Structural and Electrical Stabilities of 2D SnSe under Harsh Environments: Alkaline Environment and Mechanical Strain, ACS Appl. Mater. Interfaces 14 (2022) 9824–9832. https://doi.org/10.1021/acsami.1c22963.

Acknowledgments

I am grateful to the Doctoral School of Chemistry at University of Szeged and the Head of Department of Physical Chemistry and Materials Science, **Dr**.**Ágota Tóth**, for her support to international students during my doctoral studies.

I would like to thank my supervisors, **Dr. Csaba Janáky** and **Dr. Péter S. Tóth**, for their guidance and support during my doctoral studies in the research group. I would also like to thank them for the supporting my attendance in several international and local conferences to broaden my knowledge and get new views for my doctoral work.

I am thankful to **Prof. Krishnan Rajeshwar** for his conceptualization and advices of the manuscripts during my doctoral studies.

Many thanks to the former, and current members of the research group for their help in my research work, and for creating a friendly and innovative working environment. I would like to highlight the help of Dr. Ahmed Mohsen Mohamed Ismail Mohamed, Dr. Gábor Bencsik, Dr. Jie He, Dr. Gergely Ferenc Samu, Dr. Egon Kecsenovity, Dr. Ádám Balog, Dr. Ádám Vass, Ms. Cintia Hajdú and Ms. Katalin Sziveri, who helped me in various aspects of my study and life, for some measurements, procuring chemicals, management, and engaging in my daily English practice session.

I am also grateful to many friends at Szeged who have provided a wonderful atmosphere for social activities, to distract my attention and cheer me up after some unsuccessful experiments. I have had excellent companions from different countries who have helped me broaden my knowledge about many other cultures.

I greatly acknowledge the PhD scholarship from **China Scholarship Council** (CSC), and the Stipendium Hungaricum Scholarship from **Tempus Public Foundation** (TPS), for giving me this opportunity to study at the University of Szeged.

Last but not least I owe big thanks to **my family** for their unwavering support, understanding, and encouragement, which give me the strength to persevere through challenges and pursue my doctoral degree in abroad.

Publication list

Hungarian Scientific Bibliography (MTMT) identifier: 10069636

Publications related to the scientific topic of the dissertation:

1) **Qianqian Ba**, Péter S. Tóth, Cintia Hajdú, Csaba Janáky. Photoelectrochemical behavior of GaTe nanoflakes prepared by exfoliation. Electrochimica Acta 507 (2024): 145105.

   IF_{2025} = 5.5

2) **Qianqian Ba**, Péter S. Tóth, Ádám Vass, Krishnan Rajeshwar, Csaba Janáky. Photoelectrochemical hydrogen evolution on macroscopic electrodes of exfoliated SnSe flakes. Applied Catalysis A, General 661 (2023): 119233.

   IF_{2025} = 4.7

3) Péter S. Tóth, **Qianqian Ba**, Csaba Janáky. Photoelectrochemistry of two-dimensional and layered materials: a brief review. Journal of Solid State Electrochemistry 27 (2023): 1701–1715.

   IF_{2025} =2.6

$\sum$IF = 12.8

Conferences

Oral presentation:

Qianqian Ba, Péter S. Tóth, Csaba Janáky: Application of SnSe-based macroscopic electrodes for photoelectrochemical hydrogen evolution reaction.

XLV. CHEMISTRY LECTURES, 25-27, October, 2022, Szeged, Hungary.

Poster presentations:

1) **Qianqian Ba**, Péter S. Tóth, Csaba Janáky: Study of the hydrogen evolution reaction on macroscopic SnSe-based photoelectrodes.

   244th ECS Meeting, 8-12, October, 2023, Gothenburg, Sweden.

2) **Qianqian Ba**, Péter S. Tóth, Csaba Janáky: Photoelectrochemical hydrogen evolution on macroscopic SnSe-based electrodes.

   Graphene2023 Conference, 27-30, June, 2023, Manchester, UK.

3) **Qianqian Ba**, Péter S. Tóth, Csaba Janáky: Study of the photoelectrochemical hydrogen evolution reaction on exfoliated SnSe electrodes.

   YOURHETCAT 2022 CONFERENCE, 11-13, July, 2022, Szeged, Hungary.

4) **Qianqian Ba**, Péter S. Tóth, Csaba Janáky: Investigation of photoelectrochemical hydrogen evolution reaction on exfoliated SnSe electrodes.

   E-MRS SPRING MEETING 2022, 30 May-3 June, 2022, Online.

5) **Qianqian Ba**, Péter S. Tóth, Csaba Janáky: Application of exfoliated SnSe photoelectrodes for hydrogen evolution reaction.

   XXV. SPRING WIND CONFERENCE, 6-8, May, 2022, Pécs, Hungary.